Author/s:
Li, Rui

Title:
Localisation of the Epileptogenic Zone from Interictal State MEG Data of Focal Epilepsy Patients

Date:
2020

Persistent Link:
https://hdl.handle.net/11343/238457

Localisation of the Epileptogenic Zone from Interictal State MEG Data of Focal Epilepsy Patients

Rui Li

Doctor of Philosophy

January 2020

Department of Biomedical Engineering

Melbourne School of Engineering

The University of Melbourne

This thesis is being submitted in total fulfillment of the degree.

Abstract

Over twenty million people in the world have drug refractory epilepsy. Their seizures cannot be adequately controlled by medication. Epilepsy surgery can remove or alter abnormal brain areas where seizures start, which is the only way to cure epilepsy and can be an effective treatment for drug refractory epilepsy patients. Accurate localisation of the epileptogenic zone (EZ) is crucially important to achieve seizure freedom after surgery. Magnetoencephalography (MEG) is a non-invasive brain functional imaging technique with superb temporal resolution. Clinically, neurophysiologists visually annotate interictal spikes in MEG recordings and apply localisation methods using averaged spikes. The manual annotation of spikes can be very time consuming for neurophysiologists.

The aim of this thesis is to develop automatic methods to localise the epileptogenic zone using interictal state MEG recording for focal epilepsy patients. This thesis comprises three research objectives to achieve this goal. First, investigate localisation performance of kurtosis beamforming with various source selection approaches; the use of a 1 second sliding window for calculating kurtosis is shown to deliver the best performance relative to the other measures considered. Second, develop a method to detect interictal spikes automatically on virtual sensors (VSs) that are reconstructed using beamforming; the method based on feature extraction and machine learning delivers similar performance to labels by expert raters. Third, explore spatial distribution of interictal spikes across VSs and associate spike frequencies with EZs and surgical outcomes; the method is promising for localising the EZ at the lobe level. Potential future research is discussed based on these outcomes.

Declaration

This thesis encompasses my original work towards the Doctor of Philosophy.

Due acknowledgement has been made in the text to all other material used.

This thesis is fewer than the maximum word limit in length, exclusive of tables, maps, bibliographies and appendices.

Melbourne, Australia, January 2020.

Rui Li

Acknowledgement

I thank all my supervisors for their continuous support, guidance and encouragement over the past a few years. I am very grateful for being trained by them as a PhD student.

I thank my primary supervisor and mentor, Prof. David B. Grayden, for his continuous support and professional research training.

I thank Prof. Mark J. Cook for his guidance and extensive support in the clinical aspects of the project.

I thank Prof. David T. J. Liley for helping me with MEG technique and experiments.

I thank A/Prof. Chris Plummer that the knowledge he shared from his unique experience in presurgical evaluation using MEG in epilepsy.

This is an interdisciplinary project that I have received invaluable support and help from engineering and clinical researchers and clinicians.

I thank Dr. Levin Kuhlmann for discussions, feedback and helping throughout my candidature.

I thank Dr. William P. Woods for sharing his knowledge of MEG signal processing and managing computational resources for me.

I thank Simon J. Vogrin for kindly sharing high quality data with me and our many clinical discussions.

I thank Dr. Udaya Seneviratne for kindly labelling spikes and patient meetings.

I thank Dr. Wendyl J. D'Souza for kindly labelling spikes and teaching me clinical spike knowledge.

I thank Andria Pelentritou for kindly sharing programs and for warm-hearted help.

I particularly want to thank Dr. Chris Plummer, Mr. Simon Vogrin, Dr. William P. Woods, Dr. Michael A. Murphy, Dr. Mark J. Cook and Dr. David T.J. Liley for the collection of the MEG data and other clinical data from the epilepsy patients. Thank you all for kindly sharing this precious dataset with me, and for the clinical and technical support I received from this wonderful team that made this PhD project possible.

Studying abroad as a PhD student was a brand-new life experience for me and for my family.

I thank my friends who accompanied me throughout my study and my life.

I thank my grandma for her kindness and love.

I thank my parents, Xiuli Tang and Chang’an Li, for their love and education.

Contents

List of figures

List of tables

Chapter 1 Introduction

1.1 Epilepsy and seizure control

Our brain is composed of billions of neurons. In the normal state, neurons can generate thoughts, feelings, movements and control our body functions. In seizure state, the normal electrical patterns of the brain can be disrupted, causing neurons to fire in ways that prevents normal brain function. Epilepsy is a neurological disease that causes the brain to have recurrent seizures (Fisher et al., 2005). Estimates are that 1% of population in the world is affected by epilepsy (Sander & Shorvon, 1996; Stapleton-Kotloski et al., 2014). In two thirds of patients, seizures can be controlled by medications. However, one third of patients do not respond to anti-epileptic drug (Schuele & Lüders, 2008).

Generally, epilepsy patients have two types of seizures: generalised and focal (Stafstrom & Carmant, 2015). Generalised seizures can involve both hemispheres of the brain instantly with abnormal activity. Focal seizures start in a region of the brain and may spread to other areas. Over half of epilepsy patients have focal seizures (Nguyen et al., 2013). They have various symptoms often termed "auras", including motor, sensory or psychic abnormalities, inexplicable feelings of joy or sadness, automatisms, or a sense of warning.

There are three commonly used treatments to control seizures for drug refractory epilepsy patients. Vagus nerve stimulation sends electrical signals to the brain by stimulating the left vagus nerve of the neck continuously (Schachter & Saper, 1998). However, the effectiveness of this treatment is limited. Only 5% of patients with this device achieved seizure freedom, while 25% of patients have not experienced any positive seizure reduction (Englot et al., 2011).

The Responsive Neural Stimulation (RNS) device constantly monitors the brain near the seizure focus and detects abnormal electrical activities that can develop into seizures; then the system responds to give a small bursts of stimulation in an attempt to stop the seizures (Sun et al., 2008). The effectiveness of this treatment improves with time. In the first year of use in patients, 44% seizure reduction has been achieved with the RNS device; after 3 – 6 years, 66% of seizure reduction has been obtained (Bergey et al., 2015).

Epilepsy surgery is a treatment to remove or alter a portion of the brain where seizures originate. The portion of the brain that is targeted is called the "epileptogenic zone". The epileptogenic zone is defined as the minimum amount of cortex must be resected to produce seizure freedom

(Lüders et al., 2006). This treatment is the only way to "cure" epilepsy. The average seizure-free surgical outcome rate is around 70% (Engel Jr, 1992; Spencer & Huh, 2008) but many people are not surgical candidates.

Responsive Neural Stimulation monitors the brain at the seizure focus in order to detect abnormal discharges as soon as possible so as to have the best likelihood to stop the seizures. Surgical resection removes or alters the epileptogenic zone to achieve seizure freedom. Therefore, accurate and reliable localisation of epileptic sources is important for both therapies.

1.2 Modalities of epileptic source localisation

There are some complementary imaging techniques that can be utilized to localise the epileptogenic zone. Magnetic Resonance Imaging invented in 1984, is based on the absorption and radiation of radio frequency energy from hydrogen atoms within a strong external magnetic field. MRI can reliably indicate brain structural lesions and it has become the anatomical imaging strategy of choice for epilepsy patients (Duncan, 1997). However, MRI of epilepsy patients may show no lesions or may indicate comprehensive lesions with multiple foci (Cendes et al., 2016). Therefore, functional brain imaging is also often necessary to localise the epileptogenic zone.

Non-invasive functional imaging techniques have been widely used for epileptic source localisation. The major differences among them are temporal and spatial resolutions, illustrated in Figure 1-1 (Meyer-Lindenberg, 2010). Single-photon emission computed tomography (SPECT) and Positron Emission Tomography (PET) are computerized tomographic approaches that permit 3-D localisation of radionuclide tracers within the whole brain, and use various labelled compounds to determine the specific cerebral function (Phelps et al., 1975). SPECT and PET have high spatial resolution of around 4-5 mm (Engel, 2000). However, the temporal resolution of the two approaches are constrained to be hours or even days (Baillet et al., 2001).

Functional MRI detects brain activity by detecting changes of the Blood-Oxygen-Level Dependent (BOLD) magnetic signal using MRI (Huettel et al., 2004). Brain mapping generated by fMRI has high spatial resolution, with 1-3 mm voxels, but the temporal resolution of around 100 ms is poor resulting because of the slow BOLD response. Furthermore, fMRI studies are hampered by the rather complicated relationship between BOLD changes and underlying neural activities. Areas of BOLD changes in fMRI maps also do not exactly represent areas of corresponding electrical neural activities.

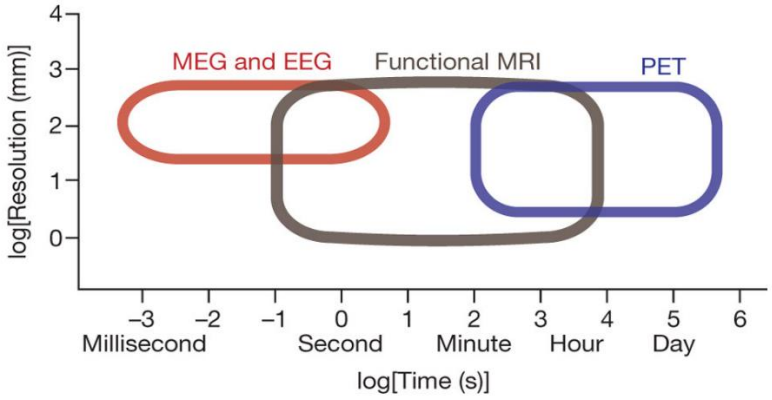

Figure 1-1 Spatial and temporal resolutions of non-invasive modalities including PET, fMRI, EEG and MEG. (Meyer-Lindenberg, 2010)

Electroencephalography (EEG) and magnetoencephalography (MEG) are techniques that measure the electric field and magnetic field induced by neural activity, respectively. They can offer superior temporal resolution compared to techniques that detect brain dynamics, such as SPECT, PET and fMRI. EEG and MEG permit research on the dynamics of neural activities at time scales typically of the order of milliseconds (Nunez & Srinivasan, 2006). However, while EEG is the most accessible and least expensive technique, it suffers from severe limitation owing to filtering and distortion caused by the skull and scalp.

Electrocorticography is the surgical implantation of subdural grids or strip electrodes that measure EEG directly from the cortex, thus avoiding the effects of signal-distorting skull and scalp. ECoG can reach 5 mm^2 spatial resolutions by using flexible, closely spaced subdural electrodes (Bazhenov et al., 2011). Because of these advantages, ECoG has been commonly utilised in pre-surgical evaluation of focal epilepsy as the gold standard (Engel Jr, 1993). The main problem with ECoG recordings arises from the risks and the excessive costs of surgical implantation and extended hospitalization with long-term monitoring (Baumgartner et al., 1995). An alternative type of intracranial EEG is stereo-EEG (SEEG) which is less invasive than ECoG since the implantation of the depth electrodes requires only small drill holes in the skull with much less post-operative pain and infection (Youngerman et al., 2019). ECoG and stereo-EEG are complementary invasive EEG recordings. ECoG is applicable when seizures are believed to originate from superficial cerebral cortex while Stereo-EEG is also useful when the seizure focus is believed to be in deep brain structures.

1.2.1 MEG in epileptic source localisation

MEG and EEG are non-invasive functional imaging modalities that have less than 1 ms temporal resolution. They are considered to be complementary modalities (Ebersole & Ebersole, 2010; Nunez & Srinivasan, 2006). They have different sensitivities to activities of populations of neurons within cortex relative to the EEG or MEG sensor outside the head. Specifically, EEG is most sensitive to sources perpendicular to the sensors, including a, b, d, e, g and h in Figure 1-2, while MEG is most sensitive to tangential sources such as k and m.

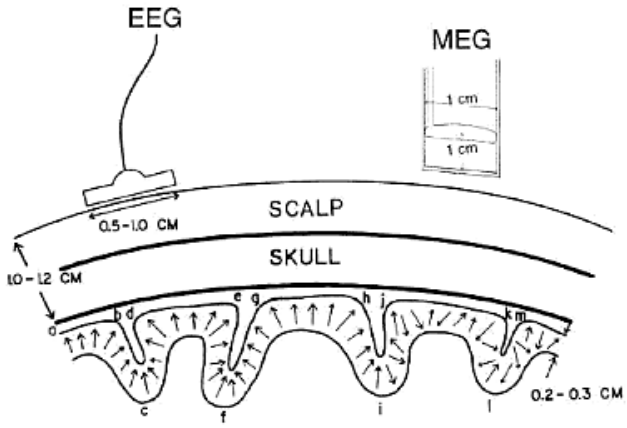

Figure 1-2 Different sensitivities of EEG and MEG to brain sources with various directions (Nunez & Srinivasan, 2006).

While the EEG signal is attenuated and distorted by the skull and scalp, MEG signals are less affected by the various tissue layers of the human head (Barth et al., 1986). Furthermore, a 3-4 cm^2 area of synchronized epileptic activities in a region of cortex can produce a detectable MEG signal, whereas around a 6-10 cm^2 area is required to generate a detectable EEG signal (Mikuni et al., 1997; Oishi et al., 2002; Tao et al., 2005).

MEG performed more accurately in localizing the implanted dipole both in a phantom head and in a human subject's head (Cohen et al., 1990; Leahy et al., 1998). The localisation error in the phantom study was 7 – 8 mm for EEG and 3 mm for MEG, while the errors were 10 mm for EEG and 8 mm for MEG in human brain.

1.3 MEG generation

MEG is the detection of magnetic fields outside the head produced by underlying neural activity. In particular, the electric neural activity is caused by two distinct neural activities: action potential currents and postsynaptic currents. An action potential is electrical activity that propagates along the membrane of a neuron, which introduces voltages changes in the neuron

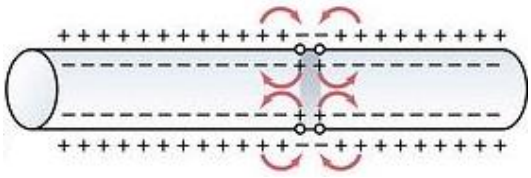

Figure 1-3 Current sources caused by an action potential (Hall, 2015).

(a) (b)

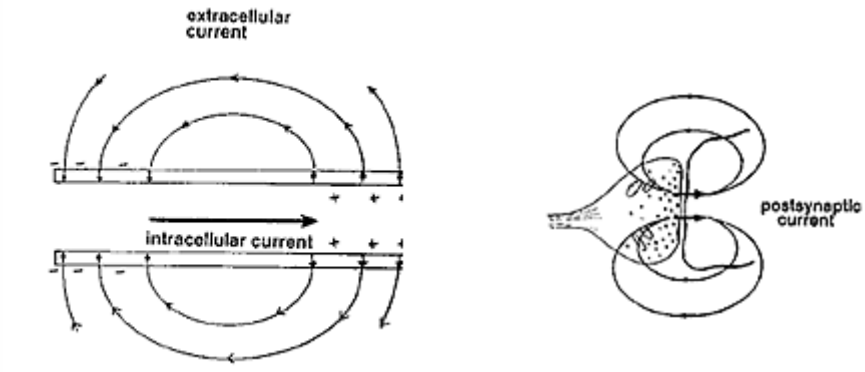

Figure 1-4 Electrical currents in the brain. (a) Intracellular currents and extracellular currents caused by an action potential. (b) Currents caused by postsynaptic activity. (Pizzella & Romani, 1990)

as depicted in Figure 1-3. During the depolarization process, the local excess of positive charges inside the membrane induce an axial current flow within the axon, represented by the red arrows inside the membrane in Figure 1-3, which lead to positive charges flowing along this direction. There is also charge flow in the extracellular space. These activities generate currents as shown in Figure 1-4(a). This process lasts for about 1 ms, and thus the related electromagnetic activity is classified as being in the "high-frequency" region.

Postsynaptic activity lasts much longer than an action potential. When an action potential reaches a synapse between two neurons, neurotransmitter is released within the synaptic cleft that binds to the receptor sites of the postsynaptic neuron, which enables chemical messenger-gated ion channels on the postsynaptic neuron to open. This process causes changes in the membrane potential and creates intracellular and extracellular currents, illustrated in Figure 1-4(b). This potential distribution is referred to as the "postsynaptic potential", which can last for several tens (or even hundreds) of milliseconds. Both intracellular currents and extracellular currents induced by postsynaptic potentials are viewed as major source of the signals measured by MEG since they usually last longer than the fast firing action potentials travelling along the axons of excited neurons (Nunez & Srinivasan, 2006).

Figure 1-5 Parallel distribution of pyramidal cells in cortex (Gray & Lewis, 1918).

The spatial structure of cells is of crucial significance to generating measurable EEG and MEG signals. It is believed that the main generators of MEG or EEG are the large pyramidal neurons, which is distributed parallel to each other as shown in Figure 1-5. This distribution allows their currents add up to each other to create a measurable signal (Nunez & Srinivasan, 2006).

1.4 MEG measurement

In order to detect rather weak MEG signals, typically less than 1 picoTesla (pT), magnetic sensors with high sensitivity are required. Until recently, the only device having the required sensitivity is the superconducting quantum interference device (SQUID) made from low-temperature superconductors. A SQUID magnetometer, shown in Figure 1-6, used to measure brain magnetic fields is usually composed of a pickup coil, an input coil, the SQUID sensor and associated electronics. A changing magnetic field induces currents in the supercooled pickup coil. The input coil transfers the induced currents to magnetic flux, and then the SQUID sensors and electronics transfer this magnetic flux into the room temperature voltage output.

There are a variety of pickup coil types, including magnetometers and first-order gradiometers that are now most commonly utilised in MEG systems. Figure 1-7 illustrates examples of pickup coils. The magnetometer in Figure 1-7(a) detects the projection of a magnetic field onto the z-axis.

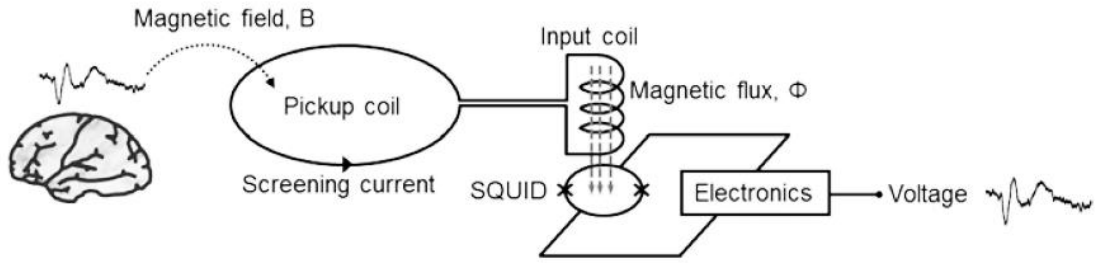

Figure 1-6 MEG measurement system (Lee & Kim, 2019).

(a) B_z (b) $\frac{dB_z}{dz}$ (c) $\frac{dB_z}{\partial y}$

Figure 1-7 Three pickup coils in present MEG systems . (a) Magnetometer, (b) axial first-order gradiometer, (c) planar first-order gradiometer (Lee & Kim, 2019).

Gradiometers are composed of two parallel or planar loops with opposite winds. As shown in Figure 1-7 (b) and (c), the axial-gradiometer and planar-gradiometer measure the gradients of B_z on the direction of the z-axis and the y-axis, respectively. B_z represents variations of a magnetic field. Since gradiometers detect the gradient of variations of magnetic field captured by two pickup coils, they have zero sensitivity to a uniformly distributed field, which is valid for sources far away from the sensors. Moreover, gradiometers are sensitive to nearby sources, such as brain sources, which are highly non-uniform. Thus, the signal-to-interference-ratio of a gradiometer can be higher than a magnetometer with a simple pickup coil by two orders of magnitude (Taulu et al., 2019).

1.5 MEG source localisation: forward problem

MEG source localisation involves two problems: the forward problem and the inverse problem. The forward problem estimates the outside head electromagnetic measurements originating from a certain brain source and distorted by the volume conduction of the head. The head volume conduction can be modelled theoretically using a spherical head model. It has been shown that the analytical solution to the MEG forward problem with the spherical head model

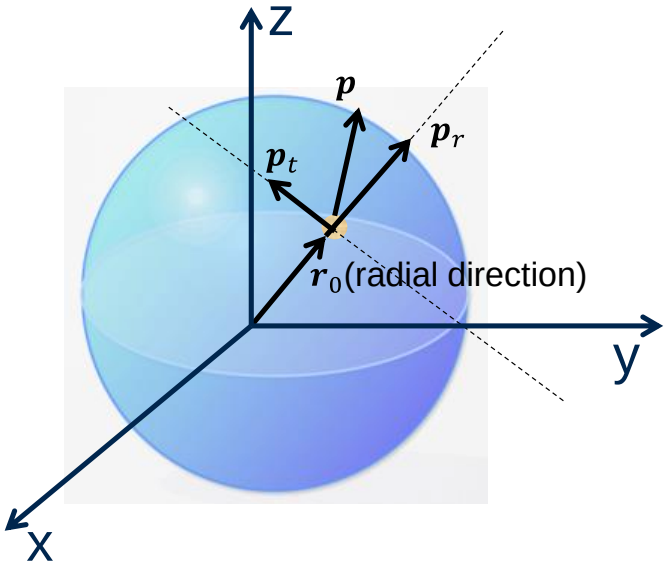

Figure 1-8 Radial sources are silent to MEG .

is (Sarvas, 1987)

$$B(r) = \frac{\mu_0}{4\pi F^2}[F\boldsymbol{p} \times \boldsymbol{r}_0 - (\boldsymbol{p} \times \boldsymbol{r}_0 \cdot \boldsymbol{r})\nabla F], \tag{1.1}$$

where $\mathbf{r}_0$ and $\mathbf{p}$ are the position and moment of the source dipole, respectively, $F = a(\boldsymbol{r} \cdot \boldsymbol{a} + ra)$ and $\boldsymbol{a} = \boldsymbol{r} - \boldsymbol{r}_0$. This equation is called the "Sarvas formula". It is important to see from Eq. (1.1) that if the direction of the current dipole $\mathbf{p}$ orients to the same direction as its position vector $\mathbf{r}_0$, then the cross product $\mathbf{p} \times \mathbf{r}_0$ becomes zero, so there is no magnetic field outside the head induced by a radial dipole. This radial dipole does not produce magnetic fields outside the head, and is thus known as the "magnetically silent source", but it does induce magnetic fields inside the head. Eq. (1.1), it is shown that the dipole with moment $\boldsymbol{p}$ is located at position $\boldsymbol{r}_0$. The moment of this dipole source can be decomposed into the radial compartment $\boldsymbol{p}_r$ and the tangential compartment $\boldsymbol{p}_t$. The radial direction of this dipole does not induce magnetic field outside the head.

Besides the spherical head model, there are two commonly used numerical head models: the boundary element model (BEM) and the finite element model (FEM). It is well accepted that the head is mainly composed of five distinct compartments: scalp, skull, cerebrospinal fluid, grey matter and white matter. The conductivities of these compartments are inhomogeneous, and both the skull and white matter have anisotropic conductivities. Typically, a simple head

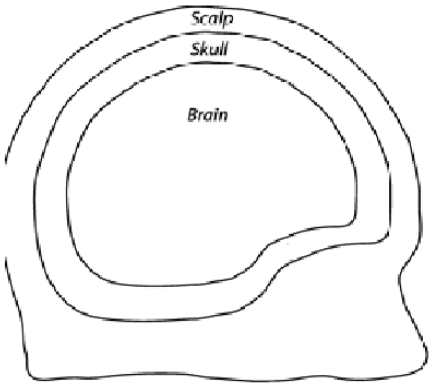

Figure 1-9 Three major compartments of the head (Heller & Volegov, 2014).

(a) (b)

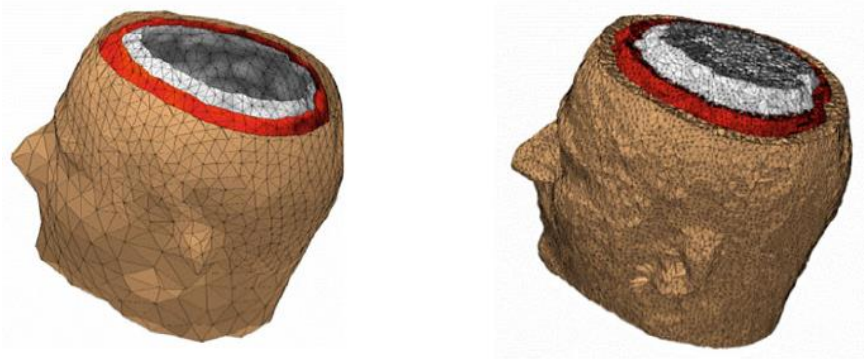

Figure 1-10 Examples of head models. (a) Head model created using BEM with the three most distinct conductivity boundaries (inner and outer skull surface, outer surface of the head) described by meshes. (b) Head model created by the FEM built with tetrahedral elements. (Haueisen & Knösche, 2019)

model (still commonly used) assumes that there are three distinct compartments, as shown in Figure 1-9: scalp, skull and brain, and the conductivity of each compartment is homogeneous and isotropic. The BEM is based on the simplified three-compartments assumption, which segments the boundaries of these different head compartments into small pieces, as shown in Figure 1-10(a), and models the conductivity jumps at these interfaces in a piecewise manner. To increase the accuracy of the head model, the compartment assumption can be replaced by a three-dimensional volume discretization instead of two-dimensional interfaces discretised using BEM. FEM segments the head volume into small voxels, as shown in Figure 1-10(b), and describes each voxel with a separate conductivity tensor (Wolters, 2003).

The leadfield matrix is used usually to represent the solution to the forward problem as

$$\boldsymbol{B} = \boldsymbol{L} \cdot \hat{\boldsymbol{J}}_s, \tag{1.2}$$

where $\boldsymbol{B}$ is the MEG measurement, $\boldsymbol{L}$ is the leadfield matrix and $\hat{\boldsymbol{J}}_s$ is the estimated dipole source.

1.5.1 Effects of different volume conductors

Most studies have concentrated on the effects of different volume conductors on EEG, since it is assumed that MEG is less distorted by the conductivity of the head tissues. Scheler et al. 2007) compared the effects of three single shell (3SS) head models and BEM head models on MEG localisations in patients with focal epilepsy. Their study suggested no significant difference between 3SS and BEM localisation results. Birot et al. (2014) performed the comparison for the locally spherical model with anatomical constraints (LSMAC), BEM and FEM head model, and indicated that these three different head models in epileptic patients have similar localisation performance. Considering the limited effect of volume conductions on MEG source localisation, we applied single shell head to discretise brain mesh to model volume conductions in this study (Nolte, 2003).

1.6 MEG source localisation: inverse problem

The forward problem describes the response of the MEG sensors to a certain brain source. The goal of our research project is to localise epileptic sources from MEG sensor measurements, which is defined as the inverse problem. However, this inverse problem is ill-posed, since the measured MEG can be interpreted by non-unique source distributions and the existence of silent radial sources.

In order to obtain a unique solution to the inverse problem, additional constraints are required. Equivalent current dipole is the most commonly used inverse method, which assumes MEG measurements are generated by one or several sources (Ramírez, 2008). This method,

$$\min \left\| \boldsymbol{B} - \mathbf{L}_s \cdot \hat{\boldsymbol{J}}_s \right\|^2, \tag{1.3}$$

minimises the residual between the real measurements $\boldsymbol{B}$ and the measurement induced by an estimated source $\hat{\boldsymbol{J}}_s$. The leadfield matrix corresponding to the estimated dipole is expressed as $\mathbf{L}_s$ in Eq. (1.2).

Minimum Norm Estimation (MNE) assumes MEG recordings are generated by a source space with electrical current intensities distributed. MNE can be expressed as

$$\min\left\|\boldsymbol{b}(t) - \boldsymbol{L}_v \cdot \hat{\boldsymbol{J}}_v(\boldsymbol{t})\right\|^2, \tag{1.4}$$

where $\boldsymbol{b}(t)$ is the measurement at time t and $\hat{\boldsymbol{J}}_v(\boldsymbol{t})$ is the estimated source space with current intensities $\hat{\boldsymbol{J}}_i(\boldsymbol{t}), i = 1, \cdots, N$ and is expressed as

$$\hat{\boldsymbol{J}}_v(\boldsymbol{t}) = \begin{bmatrix} \hat{\boldsymbol{J}}_1(\boldsymbol{t}) \\ \vdots \\ \hat{\boldsymbol{J}}_N(\boldsymbol{t}) \end{bmatrix} \tag{1.5}$$

and the corresponding leadfield matrix for current intensities is

$$\boldsymbol{L}_v = \begin{bmatrix} \boldsymbol{L}_1 \\ \vdots \\ \boldsymbol{L}_N \end{bmatrix}. \tag{1.6}$$

The solution to Eq. (1.4) is

$$\hat{\boldsymbol{J}}_v(\boldsymbol{t}) = \boldsymbol{T}\boldsymbol{b}(t) = \boldsymbol{L}_v^T[\boldsymbol{L}_v \cdot \boldsymbol{L}_v^T]^{-1}\boldsymbol{b}(t). \tag{1.7}$$

$\boldsymbol{L}_v \cdot \boldsymbol{L}_v^T$ tends to be singular for biomagnetic recordings (Sekihara & Nagarajan, 2008), so regularisation is usually applied to eliminate the singularity. Then Eq. (1.7) can be written as

$$\hat{\boldsymbol{J}}_v(\boldsymbol{t}) = \boldsymbol{L}_v^T[\boldsymbol{L}_v \cdot \boldsymbol{L}_v^T + \lambda \boldsymbol{I}]^{-1}\boldsymbol{b}(t). \tag{1.8}$$

This solution minimises the cost function:

$$\min\left\|\boldsymbol{b}(t) - \boldsymbol{L}_v \cdot \hat{\boldsymbol{J}}_v(\boldsymbol{t})\right\|^2 + \lambda\left\|\hat{\boldsymbol{J}}_v(\boldsymbol{t})\right\|^2. \tag{1.9}$$

This minimisation problem minimises the residual term as well as the norm of the estimated source itself. This is the reason why this method is called Minimum Norm Estimation (MNE). However, MNE is a biased estimator and is known to be incapable of estimating deep sources (Pascual-Marqui & Domingo, 1999). Standardized low resolution brain electromagnetic tomography (sLORETA) was proposed to modify the results of MNE to obtain the unbiased estimation of sources (Pascual-Marqui et al., 1994). This method standardises the output of MNE using its variance

$$\hat{\boldsymbol{J}}_i^T(\boldsymbol{t})\left\{\left[\boldsymbol{S}_{\hat{\boldsymbol{J}}}\right]_{ii}\right\}^{-1}\hat{\boldsymbol{J}}_i(\boldsymbol{t}), \tag{1.10}$$

where $\hat{\boldsymbol{J}}_i(\boldsymbol{t})$ is the MNE results at the ith voxel of the source space and $[\mathbf{S}_J]_{ii}$ is the variance of this estimated source. This estimated source variance is

$$\boldsymbol{S}_{\hat{\boldsymbol{J}}} = [\boldsymbol{T}\boldsymbol{b}(t)] \cdot [\boldsymbol{T}\boldsymbol{b}(t)]^T = \boldsymbol{T}\boldsymbol{b}(t)\boldsymbol{b}^{\boldsymbol{T}}(t)\boldsymbol{T}, \tag{1.11}$$

where $\boldsymbol{b}(t)\boldsymbol{b}^{\boldsymbol{T}}(t)$ is the measurement variance and can be expressed as

$$\boldsymbol{b}(t)\boldsymbol{b}(t)^T = \boldsymbol{L}_v\boldsymbol{S}_J\boldsymbol{L}_v^T + \boldsymbol{S}_{noise}, \tag{1.12}$$

where $\boldsymbol{S}_J$ is the actual source covariance and $\boldsymbol{S}_{noise}$ is the measurement noise covariance. From a Bayesian point of view, $\boldsymbol{S}_J = \boldsymbol{I}$ and $\boldsymbol{S}_{noise} = \lambda\mathbf{I}$. Thus, Eq. (1.11) becomes

$$\boldsymbol{S}_{\hat{\boldsymbol{J}}} = \boldsymbol{L}_v^T[\boldsymbol{L}_v\boldsymbol{L}_v^T + \lambda\boldsymbol{I}]^{-1}\boldsymbol{L}_v. \tag{1.13}$$

An alternative approach to reconstruct brain activity from electromagnetic data is beamforming, which does not impose additional constraints. Beamforming methods can achieve a desirable spatial resolution down to the size of the mesh grid. A beamformer is a spatial filter that scans the brain volumes by maximizing electromagnetic activity from a specified location and suppressing activity originating from other volumes (Van Veen et al., 1997). The most commonly used spatial filter is the minimum variance beamformer, which calculates the weight that minimises the beamformer output power subject to unity output of the source originating from the scanning position,

$$\min \boldsymbol{w}^T(r)\boldsymbol{R}\boldsymbol{w}(r)\,,\ s.t.\ \boldsymbol{w}^T(r)\boldsymbol{l}(r) = 1, \tag{1.14}$$

where $\boldsymbol{l}(r)$ is the leadfield for a source at position r and $\boldsymbol{R}$ is the measurement covariance. The solution to Eq. (1.14) is

$$\boldsymbol{w}(\boldsymbol{r}) = \frac{\boldsymbol{R}^{-1}\boldsymbol{l}(\boldsymbol{r})}{[\boldsymbol{l}^T(\boldsymbol{r})\boldsymbol{R}^{-1}\boldsymbol{l}(\boldsymbol{r})]}. \tag{1.15}$$

1.7 MEG source localisation in clinics

Epilepsy patients have two major abnormal electrical activities: ictal waveforms and interictal spikes, with examples shown in Figure 1-11. Ictal data is abnormal waveforms during epileptic seizures, while interictal spikes are abnormal discharges between seizures. In our study, we localised epileptic sources using interictal state MEG recordings because the limited recording

duration of MEG cannot always capture ictal events and interictal spikes are more commonly present. In addition, studies have shown that MEG localisation accuracy using ictal and

Dipole fitting, MNE and sLORETA are the most commonly used MEG source localisation methods in clinics. Neurophysiologists visually annotate interictal spikes in continuous MEG recordings, and inverse methods are modelled on the averaged spikes to localise spike sources. There were two major studies that have validated MEG source localisations against surgical resections. Englot et al. (2015) applied the dipole fitting method and the results localised to surgically resected lobes in 82% of patients in a total of 71 patients with seizure-free surgical outcomes. Plummer et al. (2019) modelled the upward slope of averaged spikes using sLORETA and localised to surgically resected cavities in 8 out of 9 seizure-free patients.

An alternative localisation method is the spatial filter: beamforming. Kurtosis beamforming, also called SAM(g2), was proposed to be applied to continuous MEG recording and does not require annotated interictal spikes (Kirsch et al., 2006; Robinson et al., 2004). Source activities can be reconstructed using beamforming by scanning the whole brain. On each scanned grid,

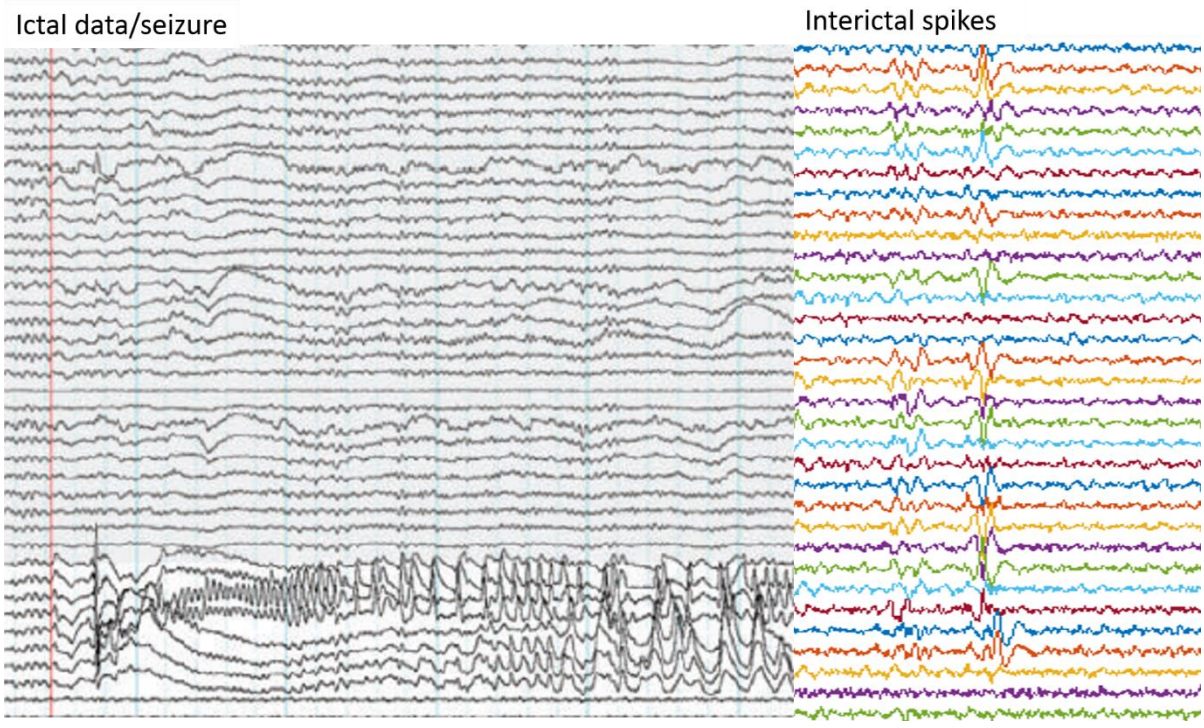

Figure 1-11 MEG recordings of ictal waveforms (Plummer et al., 2019) and interictal spikes.

interictal data are similar (Mégevand & Seeck, 2018; Plummer et al., 2019; Ramanujam et al., 2017).

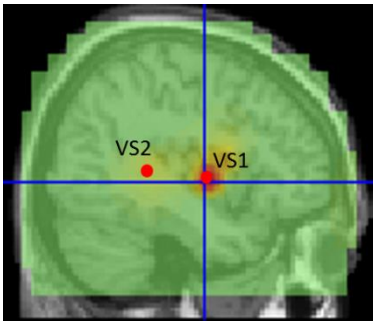

Figure 1-12 Kurtosis brain image and corresponding virtual sensors.

kurtosis was calculated, as illustrated on a brain image shown in Figure 1-12. Kurtosis detects the presence of outliers in data, which is an important characteristic of interictal spikes. Local maxima of kurtosis distributions are considered as virtual sensors (VSs). Two VSs are show in Figure 1-12 indicated by VS1 and VS2.

Kirsch et al. (2006) implemented SAM(g2) on 36 epilepsy patients and showed consistency of SAM(g2) interictal spikes localisation results with dipole fitting results when the SNR was sufficiently large and only one epileptic focus was present. Oishi et al. (2006) illustrated that locations of SAM virtual sensors were confirmed by subdural EEG measurements. Hall et al. (2018) validated localised results of kurtosis beamforming against surgical resections: in 13 seizure-free patients, 9 patients were concordant and 4 were discordant with the lobe of surgical resection.

Two studies compared the performances of several commonly used MEG inverse methods (de Gooijer‐van de Groep et al., 2013; Tenney et al., 2014). However, their results are not comparable, since de Gooijer-van de Groep et al. (2013) compared the interictal MEG spike localisation results with interictal discharges of ECoG while Tenney et al. (2014) performed the comparison between the interictal MEG spike results with ictal-onset spikes of ECoG. Specifically, de Gooijer-van de Groep et al. suggested that these three MEG inverse methods – MUSIC, SAM(g2) and sLORETA – have similar sensitivities around 25% and recommended the combination of MUSIC and SAM(g2) to obtain higher sensitivity with a slight increase in false positives. In the study by Tenney et al. (2014), the comparison was conducted on ECD, MUSIC, MNE, sLORETA, SWARM, SAM(g2)-VS, SAM(g2) and SAM-VSsys. They reported that SAM(g2) had higher accuracy, but there was no significant advantage of one method over the others. It is important to note that, when compared with other inverse methods, SAM(g2) involved much less manual work, only including artefact rejection at sensor level and at virtual sensor level in Gooijer-van de Groep's study and selection of virtual sensors with

corresponding MEG/EEG spikes morphology in Tenney et al.'s work, but still obtained similar performance in localising interictal spikes.

1.8 Limitations of using kurtosis

Bias to infrequent interictal spikes is one disadvantage of using kurtosis as a measure to detect spikes as outliers in time series data. One example is shown in Figure 1-13. A single triangular signal is present in time series $s_1(t)$ and its kurtosis in the whole window length is 5, as summarised in Table 1-1. The whole window kurtosis of $s_2(t)$ with two triangular signals is 2.5, indicating that kurtosis on the whole data is not reliable when there is more outlying data. One solution to reduce this bias is to use a sliding window. In Figure 1-13, we used a 1 s sliding window for $s_1(t)$ and $s_2(t)$. The summed kurtosis across all the sliding windows for the two signals are 11 and 10, respectively. We calculated normalised kurtosis difference between two signals using

$$\text{diff}_{g2} = \frac{|g_2[s_1(t)] - g_2[s_2(t)]|}{\text{mean}\{[g_2[s_1(t)], g_2[s_2(t)]]\}}. \tag{1.16}$$

The normalised kurtosis differences between two signals decreased from 0.7 to 0.15, demonstrated in Table 1-1.

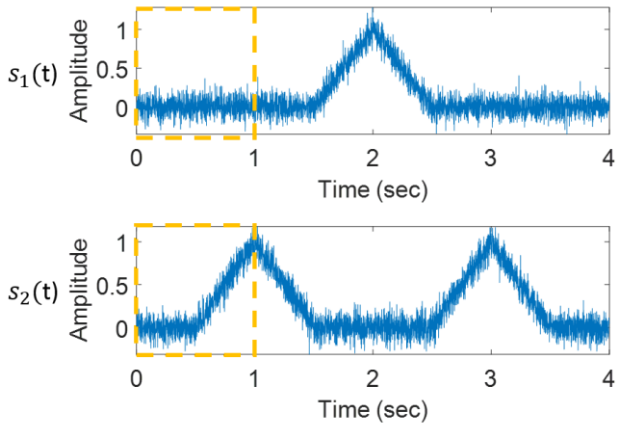

Figure 1-13 Example of kurtosis bias. Two 4 s time series $s_1(t)$ and $s_2(t)$ with one and two triangular signals, respectively, are shown as blue lines. The yellow dashed line shows the 1 s sliding window.

Harpaz et al. (2015) proposed the use of a sliding window to reduce localisation bias introduced by different spike rates. They showed improved localisation results introduced by using sliding window in two cases shown in Figure 1-14. The sliding window method successfully corrected the mislocalisations in the left column of Figure 1-14 and the modified SAM(g2) results are

Table 1-1 Kurtosis values of two time series in Figure 1-13 with whole window and 1 s sliding window and the normalised differences between the two cases.

	Kurtosis whole window	Kurtosis sliding window
$s_1(t)$	5	11
$s_2(t)$	2.5	10
diff_{g2}	0.7	0.15

shown in the right column of Figure 1-14, which covered lesions indicated by white arrows in the left column. Scott et al. (2016) investigated various lengths of sliding window used to reduce bias for seven epilepsy patients and suggested the optimal sliding window length is 1 s. In our study, we evaluated localisation performance using kurtosis beamforming with sliding widow lengths of 3 min and 1 s.

Kurtosis detects outliers in time series, which is an important characteristic of interictal spikes (Westfall, 2014). Kurtosis can also detect artefacts and other brain activities that stand out from background. One example is shown in Figure 1-15. Three source activities reconstructed using beamforming have similar kurtosis values around 6. The upper two time series have interictal spikes present indicated by blue frames, while the bottom time series has a typical alpha wave present shown in the red frame. Because kurtosis does not only detect interictal spikes, visual inspections are required on VSs reconstructed by beamforming to ensure presence of authentic spikes (Agirre-Arrizubieta et al., 2014; de Gooijer-van de Groep et al., 2013; Hall et al., 2018; Kirsch et al., 2006; Oishi et al., 2006; Tenney et al., 2014). In our study, we investigated spatial

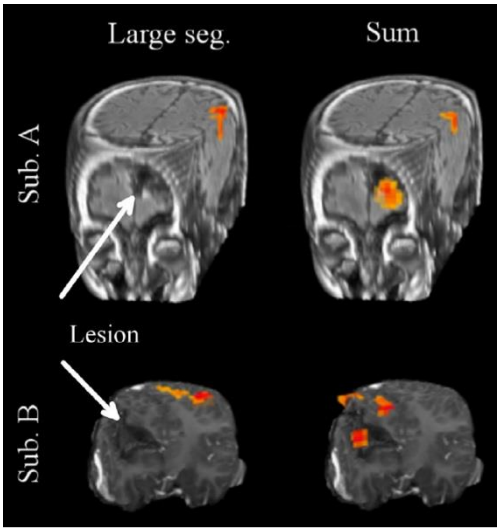

Figure 1-14 SAM(g2) localisation results with various time windows for calculation of excess kurtosis in two subjects (A and B). The white arrow indicates the position of lesion and the orange area represents the region with highest kurtosis levels (Harpaz et al., 2015).

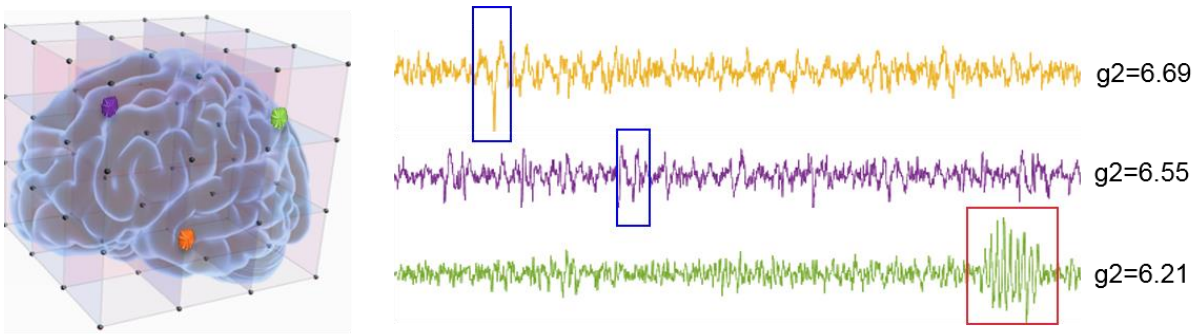

Figure 1-15 Source activities at three scanned grid and their kurtosis . Three times reconstructed using beamforming from MEG sensor data are shown by solid lines with colour yellow, purple and green. Interictal spikes are indicated by blue frames and a typical brain alpha wave is in the red frame.

distributions of interictal spikes directly rather than distribution of kurtosis to provide a method that does not require such onerous visual inspection.

1.9 Thesis overview

In this thesis, Chapter 2 describes materials used in this study, including patients, MEG recordings and pre-processing steps. Also, localisation validations used in this study are introduced in Chapter 2. Three research objectives are covered in this thesis in Chapters 3, 4 and 5.

The first objective of this study is to evaluate performance of localisation of the epileptogenic zone (EZ) using MEG kurtosis beamforming with four source selection approaches, including maximal kurtosis with 3 min sliding window, maximal kurtosis with 1 s sliding window, VS with maximal kurtosis and regions with persistent interictal spikes. The second objective is to develop a method to detect interictal spikes on VSs automatically and validate it against labels from neurophysiologists. Third, we investigate spatial distributions of interictal spikes on VSs and the association between spike frequencies and EZs.

Chapter 2 Materials

2.1 Patients

We retrospectively studied MEG recordings of 13 patients with refractory focal epilepsy. The MEG data were collected from August 2013 to October 2015 by Dr. Chris Plummer and Mr. Simon J. Vogrin (Plummer et al., 2019). I would like to acknowledge this precious clinical data that took many years of hard working to be collected, which becomes the foundation of this research project. The selection criteria for MEG recordings in pre-surgical evaluation were:

- no lesions or comprehensive lesions presented on MRI;
- deficient localized results from non-invasive modalities including video EEG monitoring (VEM), positron emission tomography and single photon emission computed tomography (SPECT);
- interictal spike discharges shown in video EEG recordings.

The study was approved by the Human Research Ethics Committees of St Vincent's Hospital, Melbourne and Swinburne University of Technology. Patients were sleep deprived and medications were withheld in the twelve hours before MEG recordings.

The demographics of the patients and their MRI, VEM, PET and SPECT performed in the presurgical evaluations are listed in Table 2-1. Of the 13 patients, six were female and seven were male. Their median duration with epilepsy until surgery was 20 years with range 4-33 years. Ten patients showed normal MRI images; the other three had complex lesions visible on MRI.

2.2 Data acquisition

MEG data were acquired using an Elekta Neuromag Oy (Helsinki, Finland) with 306 MEG channels (102 magnetometers and 204 gradiometers) with sampling rate of 1000 Hz (9 patients, before May 2015) or 5000 Hz (4 patients, after May 2015) with lowpass, anti-aliasing filters set at 330 Hz and 1650 Hz, respectively, in a magnetically shielded room. Simultaneous MEG and EEG were recorded but EEG data were not used in this study. The resting-state MEG data were recorded in blocks of up to one hour with patients' eyes closed or open, as described in Table 2-2. In each block, the MEG data was recorded continuously.

Positions of three fiducials (nasion and left and right pre-auricular) and EEG sensors were acquired using a 3D digitizer (Fastrak, Polhemus, Colchester, VT, USA) for co-registration between MEG recordings and MRI images.

2.3 Data processing

The temporal extension to signal source separation (tSSS) of Maxfilter® (Elekta Oy, v2.2.10-15, Helsinki, Finland) was applied to suppress noise and interference of the MEG recordings. MEG data with recording sampling rate 5000 Hz were down-sampled to 1000 Hz using Maxfilter, after applying a lowpass filter with frequency 333.33 Hz. The MEG data analysis developed in this study used MATLAB (The MathWorks, Release 2017a, Massachusetts, USA), the FieldTrip Toolbox (Oostenveld et al., 2011) and EEGLAB toolbox (Delorme & Makeig, 2004).

MEG recordings and patients' preoperative MRI images were co-registered by visually inspecting three fiducials and the head surface. One example of co-registration between MEG recordings and MRI images is show in Figure 2-1. The blue dots represent MEG sensors and green asterisks encompassed by white circles show the three fiducials. The single shell head model was fitted into the brain surface as the solution to the forward problem in this study (Nolte, 2003). One example of a single shell head model is shown in Figure 2-2.

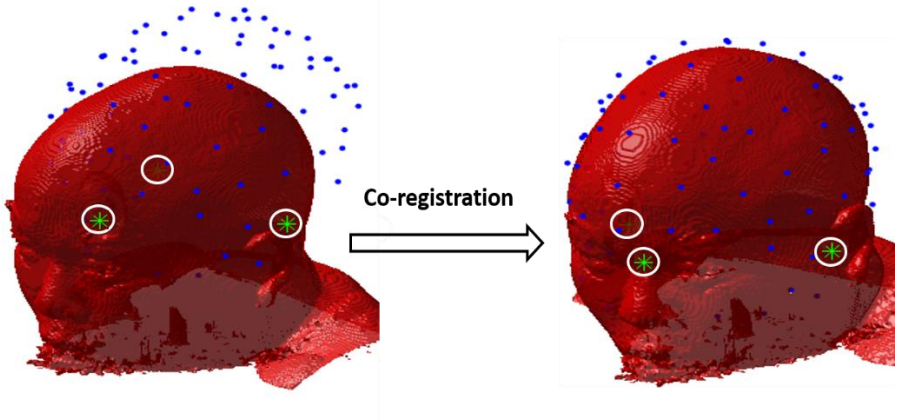

Figure 2-1 Co-registration between MEG sensors and MRI images. red surface represents the head surface. The blue dots represent the head position (positions of EEG sensors) acquired during the MEG recording. The green asterisks surrounded by white circles are the sampled fiducials. The left figure shows the locations of MEG data and MRI data before co-registration and the right figure shows their locations after co-registration.

Table 2-1 Patient demographics and presurgical work-ups. The first column shows the patient number. The demographics shown in the following two columns are genders and duration of epilepsy to surgery of each patient. The clinical results obtained from MRI, VEM, PET and SPECT are shown in the last four columns. F: female; M: male; L: left; R: right.

Patients	Sex	Duration epilepsy until surgery (years)	MRI	VEM	PET	SPECT
P007	F	33	Normal	L Anterior quadrant	R Temporal (anteromesial) L Temporal (mesial)	L Temporal (anterior)
P012	F	25	Normal	L Fronto-central	L Frontal (lateral) L Parietal (lateral)	L Frontal (lateral) L Parietal (lateral)
P016	M	12	Normal	L Fronto-temporal	L Frontal (orbital) L Temporal (mesial)	L Frontal (posterior)
P035	M	31	Normal	R Anterio quadrant	R Temporal (mesial, anterolateral)	R Temporal (lateral)
P037	F	33	Multilobar dysplasia	R Fronto-central	Not done	Not captured
P040	F	8	Normal	R Lateral temporal	Normal	Not captured
P042	F	4	Normal	L Anterior temporal	L Temporal (anterior pole)	L Temporal (lateral)
P046	F	4	Normal	L Fronto-central	R Frontal (superior frontal gyrus) R Parietal (paracentral lobule)	Not captured
P049	M	32	Multilobar dysplasia	L Posterior quadrant	L Occipito-parietal junction	Not captured
P061	M	20	R Frontal gliosis	R Frontal	Not done	Not captured
P070	M	6	Normal	L Anterior quadrant	L Temporal (anterior pole)	Not captured
P072	M	32	Normal	R Frontal	L Temporal (mesial)	R Frontal (lateral) R Temporal (lateral)
P074	M	5	Normal	L Parieto-occipital	Vertex (bilateral, sensorimotor strip)	L Temporal (lateral)

Table 2-2 MEG recordings for all patients in this study. The first column shows the patient number. The second column gives the total recording duration for each patient, which is composed of continuously recorded blocks from one block up to five blocks. The next five columns give the recording durations and patient's states (eyes closed/open) for each block. The last column gives the total amount of clean data after pre-processing.

Pat	Total length	Block1	Block2	Block3	Block4	Block5	Clean data
P007	45.7 min	45.7 min Eyes closed	-	-	-	-	31.9 min
P012	40.4 min	34.7 min Eyes closed	5.7 min Eyes open	-	-	-	38.9 min
P016	62.3 min	54.7 min Eyes closed	7.6 min Eyes open	-	-	-	56.5 min
P035	55.8 min	35.8 min Eyes closed	14.6 min Eyes closed	5.4 min Eyes open	-	-	46.7 min
P037	51.4 min	32.0 min Eyes closed	14.2 min Eyes closed	5.3 min Eyes open	-	-	46.8 min
P040	49.0 min	42.9 min Eyes closed	4.1 min Eyes open	-	-	-	41.2 min
P042	53.2 min	16.1 min Eyes closed	30.6 min Eyes closed	6.4 min Eyes open	-	-	41.5 min
P046	78.1 min	20.8 min Eyes closed	20.8 min Eyes closed	5.0 min Eyes closed	15.8 min Eyes open	15.8 min Eyes open	73.5 min
P049	64.6 min	41.1 min Eyes closed	17.9 min Eyes closed	5.6 min Eyes open	-	-	59.8 min
P061	54.2 min	6.5 min Eyes closed	39.2 min Eyes closed	8.5 min Eyes open	-	-	52.5 min
P070	66.8 min	16.5 min Eyes closed	42.7 min Eyes closed	7.7 min Eyes open	-	-	62.3 min
P072	47.1 min	6.6 min Eyes closed	34.2 min Eyes closed	6.3 min Eyes open	-	-	45.0 min
P074	38.1 min	38.1 min Eyes closed	-	-	-	-	35.0 min

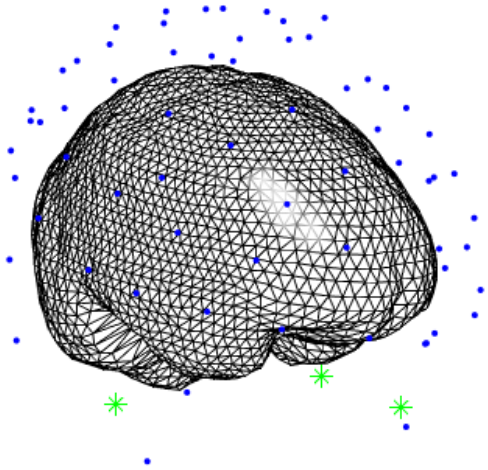

Figure 2-2 single shell head model. The triangulated mesh shows the single shell method. The blue dots and green asterisks are the same as Figure 2-1.

The MEG data was first filtered using a 3-70 Hz, 4th-order, two-directional Butterworth band-pass filter and a 48-52 Hz, 3rd-order, two-directional Butterworth band-stop filter. The continuous filtered data were then manually inspected to identify MEG channels and segments polluted by noise, coil jumps and muscle artefacts. The remaining clean data were concatenated to each other in each recording block to form long-term data. The duration of clean data for each patient is shown in the last column of Table 2-2.

Independent Component Analysis (ICA) was performed on the data to reject the independent components related to electrocardiogram and electrooculography artefacts. The *runica*() function of EEGLAB was used to implement ICA to MEG sensor measurement. The measurement $\boldsymbol{x}$ is a linear superposition of a set of sources $s_1, s_2, \cdots, s_N$ mixed by a matrix $\mathbf{A}$, which can be expressed as

$$\boldsymbol{x} = \boldsymbol{A}\boldsymbol{s}. \tag{2.1}$$

The ICA method can recover sources from the measurement vector by finding an unmixing matrix $\boldsymbol{W}$. To obtain independent components, the function *runica*() first inputs the measurement to a single-layer neural network and updates the weights of the network by maximising the entropy between the outputs (Bell & Sejnowski, 1995).

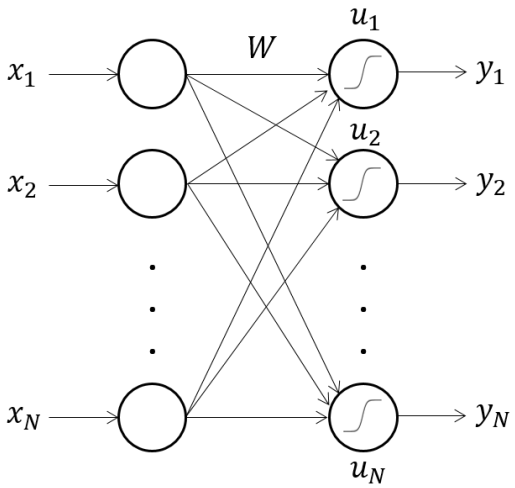

Figure 2-3 ICA implementation : single-layer neural network. The input to the neural network is $x_1, x_2, \cdots, x_N$. The transform weight from the input layer to the hidden layer is the matrix $\boldsymbol{W}$. Each unit of the output layer is transformed by a sigmoid function $g(u)$, which is the output of the network.

The one-layer network used by *runica*() is shown in Figure 2-3. The input to the neural network is the measurement $\boldsymbol{x}$, which is linearly passed to the output layer by the matrix $\boldsymbol{W}$ with a bias $\boldsymbol{w}_0$ expressed as

$$\boldsymbol{u} = \boldsymbol{W}\boldsymbol{x} + \boldsymbol{w}_0. \tag{2.2}$$

The output of the network is transformed by the sigmoid function $\boldsymbol{y} = g(\boldsymbol{u})$, where the sigmoid function is

$$g(u) = \frac{1}{1 + e^{-u}}. \tag{2.3}$$

To reduce the statistical dependence between outputs, the weight matrix $\boldsymbol{W}$ is updated to maximise the entropy between the outputs $y_1, y_2, \cdots, y_N$. The updated rule is

$$\Delta\boldsymbol{W} \propto [\boldsymbol{W}^T]^{-1} + (\boldsymbol{I} - 2\boldsymbol{y})\boldsymbol{x}^T \tag{2.4}$$

$$\Delta\boldsymbol{w}_0 \propto \boldsymbol{I} - 2\boldsymbol{y} \tag{2.5}$$

The training of the network stops, when the change of weights between two iterations is smaller than 10^{-7}. The change of weights is measured by the 2-norm of the matrix.

We applied ICA decomposition to the MEG sensor data and obtained the topology and time series of each independent component. The electrocardiogram (ECG) and electrooculography (EOG) components could be distinguished by their topologies and time series. An example is

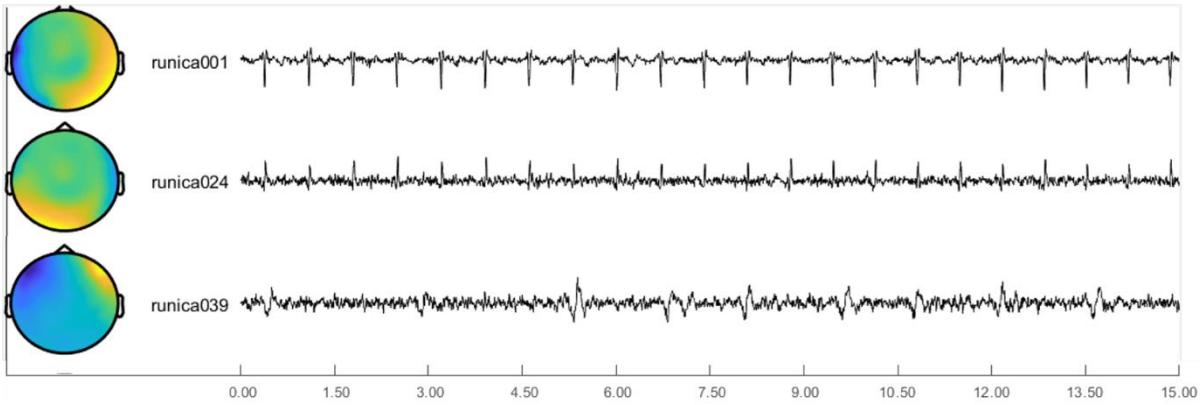

Figure 2-4 ECG and EOG independent components . The head shape heat maps illustrated at left panel of the figure are topologies of the independent components. The right side shows the time series of the components. The upper two components are related to ECG and the lower component is an EOG component.

shown in Figure 2-4. Usually, there are two ECG components, whose topologies are similar but rotated. Also, the time series of the ECG component is typical, with regular ECG discharges. The EOG components also have particular topologies and time series. The top two rows in Figure 2-4 are ECG components and the bottom row is an EOG artefacts component. The ECG and EOG related components were removed from MEG recordings and the following analysis in this study were performed on MEG data with ECG and EOG artifacts rejected.

2.4 Validation

This work studied the localisation of the epileptogenic zone (EZ) from MEG recordings of focal epilepsy patients. To validate the MEG localised regions, we utilised the resected areas in surgeries, and the clinical EEG-MEG source localisation results in preoperative evaluations (Plummer et al., 2019).

The resected areas in surgeries delineated in our study were based on the resections described and depicted by (Plummer et al., 2019). Also, each depicted surgical resection was confirmed by clinicians. The post-surgical outcome was evaluated with a minimum follow-up period of 14 months (median 21 months, range 14-39 months). The postoperative outcomes in this study were classified using Engel scores with four classes shown in Table 2-3 (Engel Jr, 1993). Class I: free of disabling seizures (seizure reduction between 98% and 100%, P012, P016, P035, P037, P042, P061, P070, P072, P074); Class II: rare disabling seizures (seizure reduction 80% and 99%, P007, P046); Class III: worthwhile improvement (seizure reduction 59% and 60%, P040, P049); Class IV: no worthwhile improvement (no patients). P046 with seizure reduction

99% was classified as Engel II, because her disabling seizure after surgery showed a different semiology.

Furthermore, the brain source localisation in this study was validated with clinical EEG-MEG localisation results of the same recordings for the same patient cohort (Plummer et al., 2019), in which independent EEG source localisation (Bonilha et al.), MEG source localisation (MSL) and combined EEG and MEG source localisation (EMSL) were investigated. In our study, we only validated our solutions with ESL and MSL clinical results, since EMSL results did not differ from ESL and MSL.

In the clinical localisation, a neurophysiologist (CP) manually annotated interictal spikes in the MEG and EEG data, which were averaged with their negative peaks aligned independently for each modality. The 'take-off' of the averaged spike is defined as the first sample that reached >50% magnitude of the baseline. The baseline is defined as the interval prior to the

Table 2-3 Patient surgery characteristics . Each of the 13 patients included in this study are listed along with their ages at surgery, resected areas, months of follow-up, post-surgery seizure reduction rates and Engel surgical outcome scores. ATLE: anterior temporal lobectomy; HC: hippocampus; PCL: paracentral lobule; TPO: temporo-parietal-occipital junction.

Patients	Age at surgery (year)	Resected area	Follow-up months	Post-surgery seizure reduction (%)	Engel outcome
P007	54	L ATLE	30	80	II
P012	27	L Paracentral lobule	23	99	I
P016	25	L Inferior frontal gyrus	39	98	I
P035	51	R ATLE	26	100	I
P037	36	R premotor cortex	17	99	I
P040	29	R ATLE	21	59	III
P042	36	L ATLE	20	100	I
P046	10	R PCL, precuneus	26	99	II
P049	49	L TPO junction	15	60	III
P061	33	R Inferior frontal gyrus	14	100	I
P070	25	L ATLE (HC spared)	22	98	I
P072	39	R Premotor cortex	21	99	I
P074	20	L Superior parietal lobule	20	100	I

take-off and its length is twice the number of spike samples. The source localisation method sLORETA was applied on the early, middle and late phases of the averaged MEG spikes and EEG spikes separately. The early phase was the first sample of averaged discharges that the sLORETA solution with 90% variance explained. The middle phase was defined as the sample with its amplitude reaching the one that occurred earlier between 50% of the negative peaks and 50% of the mean global field power. The late phase was fitted on the negative peak. In our validation, the onset of the source used the earliest source solution among early-ESL, middle-ESL, late-ESL and early-MSL, middle-MSL, late-MSL of the clinical solutions. One example of clinical ESL and MSL is shown in Figure 2-5, in which the first row and the second row show the MSL and ESL, respectively. The annotated interictal spikes from the MEG and EEG recordings are shown on the left side of the figure, in which three vertical dashed lines indicate the early, middle and late phases of source solutions. The localized areas for early, middle and late phases are shown sequentially in the figure.

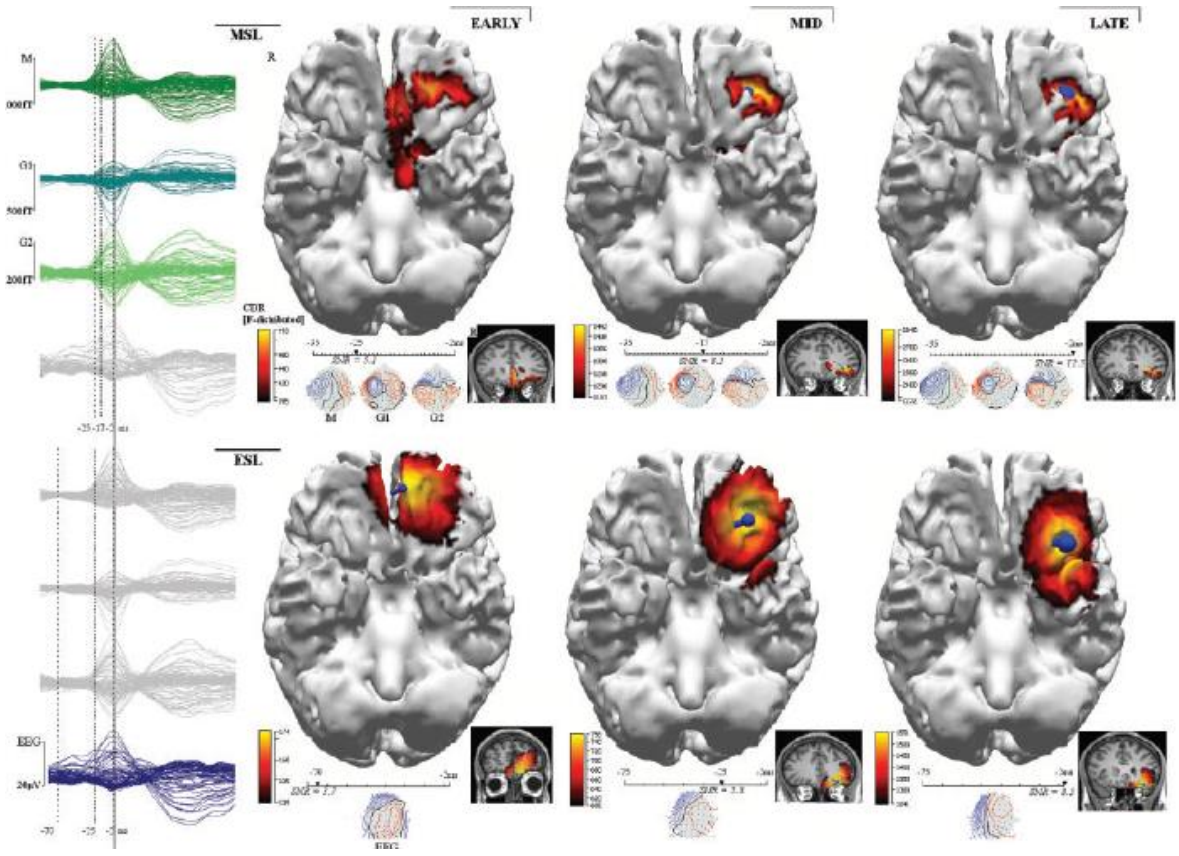

Figure 2-5 Clinical EEG and MEG source localisation . The first row is MSL, in which the MEG interictal discharges are shown on the left side with three vertical lines to indicate the early-MSL, middle-MSL and late MSL, for which localisation results are shown in the following three columns on the right. The second row is the ESL and figures are arranged similar to the first row. (Figure 3 in Plummer et al., 2019).

The propagations of sources were source location solutions that occurred later than the earliest source location. The source onset and propagation from the clinical study is shown in Table 2-4. There were two patients (P007 and P046) without propagation and the remaining 11 patients showed both onset and propagation. For the 11 patients with propagation present, the modalities localized to the earliest source solution are shown in brackets in the onset column.

This chapter introduces epilepsy patients, MEG recordings and validations used in this study. The following three chapters cover three objectives of this thesis, in which artefacts of MEG data were rejected visually and using ICA introduced in Section 2.2 Solutions to forward problem or leadfield matrices of each patient were generated using single shell head model and co-registered with MEG sensors. Two validations, clinical solutions and surgical resections, introduced in Section 2.4 were used in Chapter 3 and Chapter 5 as localisation references.

Table 2-4 Clinical EEG and MEG source localisation. The second column shows the onset position of sources and the second row gives the propagation locations of the epileptic spikes.

Patients	Onset	Propagation
P007	Bitemporal (Left Baso-mesial temporal; Right mesial temporal)	-
P012	Paracentral lobule (early-MSL)	Left Parietal convexity
P016	Rectal gyrus (early-ESL)	Medial orbitofrontal gyrus; Lateral orbitofrontal gyrus
P035	Antero-basal temporal cortex (early-MSL)	Infero-lateral temporal cortex; later to posterior temporal cortex and parietal convexity
P037	Base pre-central gyrus approximating face (early-MSL)	Pre-central gyrus approximating hand, later propagate upward along the line of the pre-central gyrus
P040	Posterior Superior temporal gyrus (early-MSL)	Lateral MTG, and later to right uncus
P042	Baso-mesial temporal (early-MSL)	Basolateral temporal cortex
P046	Right posterior paracentral lobule, precuneus.	-
P049	TPO junction (early-MSL)	Pre-occipital notch, PON
P061	Right inferior frontal gyrus (early-ESL, early-MSL)	Infero-medial
P070	Anterior inferior temporal gyrus (early-ESL)	Posterior superior temporal gyrus
P072	Right Premotor cortex (early-MSL)	Frontal pole
P074	Junction of the post-central sulcus and superior parietal lobule (early-MSL)	Ipsilateral pre-central gyrus

Chapter 3 Kurtosis beamforming of MEG data

3.1 Introduction

Magnetoencephalography (MEG) is a non-invasive modality can be used in presurgical evaluation to aid the localisation of the epileptogenic zone and guide the implantation of intracranial electrodes for patients with drug refractory focal epilepsy (Agirre-Arrizubieta et al., 2014; Englot et al., 2015; Plummer et al., 2019). The localisation of interictal spikes observed between seizures in focal epilepsy is crucial for the determination of the surgical resection (Rosenow & Lüders, 2001).

MEG interictal spike localisation is an ill-posed inverse problem. One category of inverse methods solves the ill-posed problem by imposing constraints on the source. Equivalent current dipole (ECD) assumes that the sensor data is generated by a single source dipole. Minimum norm estimation (MNE) and standardized low resolution tomographic analysis (sLORETA) are current density models that assume the sources are composed of a large number of small current dipoles within cortex (Pascual-Marqui & Domingo, 1999; Pascual-Marqui et al., 1994; Ramírez, 2008). These methods require neurophysiologists to identify interictal spikes from continuous MEG data, on which the ill-posed inverse problem is solved by imposing constraints.

An alternative solution to solve MEG localisation is beamforming, which is spatial filtering that outputs the source activity at the scanning position without distortions and suppresses noise and interference from other locations (Van Veen et al., 1997; Vrba & Robinson, 2001). Beamforming does not impose additional constraints, and it can be applied on continuous MEG recordings without requiring interictal spikes annotated by neurophysiologists. SAM(g2) was proposed to localise interictal spikes automatically by utilising synthetic aperture magnetometry (SAM) beamforming to reconstruct brain source time series and using kurtosis to detect the outliers of the reconstructed sources, which is one of the characteristics of interictal spikes (Kirsch et al., 2006; Robinson et al., 2004).

In the past decade, SAM(g2) has shown promising performance for source localisation in presurgical evaluation. Oishi et al. (2006) showed that, in a cohort of nine patients, regions with the maximum percentage of spikes revealed by SAM(g2) were colocalized to the seizure onset zone defined by subdural EEG in seven patients and partial co-localisation was shown in two patients. Ishii et al. (2008) showed that overlaps between regions localized from the

interictal spikes using SAM(g2) and the SOZ defined in electrocorticography in all three children with epileptic focal cortical dysplasia that were studied. Sugiyama et al. (2009) reported that SAM(g2) colocalized to the resected cavity in seven out of eight patients with surgeries. In 2018, Hall et al. (2018) validated SAM(g2) in a relatively large patient cohort. They retrospectively studied 22 patients and compared SAM(g2) results with surgical resection. In 14 seizure-free patients, SAM(g2) localised to the surgical cavity in six patients, localised to the same lobe with surgical resection in three patients, mis-localised the surgical resection in four patients, and had uninterpretable results for one patient. Additionally, while it has been believed that EEG and MEG are unable to detect deep brain activities (Agirre-Arrizubieta et al., 2009; Wennberg et al., 2011), it was reported that SAM(g2) can localise interictal spikes generated from mesial temporal lobe (Hillebrand et al., 2016). SAM(g2) can provide useful information for diagnosis even for patients with vagus nerve stimulation, which can severely contaminate MEG recordings (Stapleton-Kotloski et al., 2014).

The kurtosis distribution of the brain can be obtained with SAM(g2), on which the local maxima are considered as virtual sensors (VSs). Kurtosis is a statistical parameter that shows the existence of the outliers (Westfall, 2014). Interictal spikes are characterised by standing out from the background data, which can contribute to the high kurtosis values. There have been two major approaches to obtain the kurtosis distribution from beamforming results in previous studies. One approach is to calculate the kurtosis from the whole MEG data performed by beamforming (Agirre-Arrizubieta et al., 2014; de Gooijer‐van de Groep et al., 2013; Hall et al., 2018; Kirsch et al., 2006; Oishi et al., 2006; Rose et al., 2013; Tenney et al., 2014). Another approach applies a sliding window to deal with the kurtosis bias introduced by different spike rates. The g2 maps are generated by averaging the kurtosis values within each sliding window.

One limitation of using kurtosis is that it is biased to the infrequent interictal spikes. A high kurtosis value introduced by the infrequent interictal spikes present in a time series can drop dramatically with frequent spikes in the same time series. Harpaz et al. (2015). proposed the use of the sum kurtosis along the sliding window to remove the bias, and recommended that the sliding window length should not include more than one interictal spike. In their work, it was shown that mis-localisation caused by the spike frequency bias can be fixed by applying the sliding window method. Scott et al. (2016) also investigated kurtosis beamforming with a sliding window. They suggested the optimal sliding window length was 1 second by analysing the MEG recordings from seven patients.

In the selection of localised sources for the present study, we adopted these two categories: the VS with genuine spikes and the voxel with the maximal kurtosis. Another solution we considered was the voxel with the maximal kurtosis in the summed g2 map with a 1 second sliding window. Additionally, we proposed a method to achieve regions with persistent spikes and adopted this region as another solution in our work. All the localisation results in our study were validated against clinical source localisation results and surgical resection areas.

3.2 Methods: Localized solutions from multiple kurtosis beamforming results

3.2.1 Kurtosis beamforming

Beamforming is spatial filtering that outputs a signal from a scanned position without distortion and suppresses noise and inferences from other locations (Hillebrand & Barnes, 2005; Huang et al., 2004; Sekihara et al., 2002; Sekihara et al., 2001). Vectorized linear constraint minimum variance (LCMV) beamforming was used in this study to reconstruct source level brain activity,

$$\min_{\boldsymbol{W}(\boldsymbol{r})} tr\{\boldsymbol{W}^T(\boldsymbol{r})\boldsymbol{R}\boldsymbol{W}(\boldsymbol{r})\} \;\; s.t. \boldsymbol{W}^T(\boldsymbol{r})\boldsymbol{L}(\boldsymbol{r}) = \|\boldsymbol{L}(\boldsymbol{r})\|\boldsymbol{I}, \tag{3.1}$$

where $\boldsymbol{W}(\boldsymbol{r})$ are the vectorized beamforming weights on scanning position $\boldsymbol{r}$, $\boldsymbol{R} = \boldsymbol{X} \cdot \boldsymbol{X}^T$ is the covariance matrix, $\boldsymbol{X}$ is the MEG data, $\boldsymbol{L}(\boldsymbol{r})$ is the lead field matrix located at position $\boldsymbol{r}$ on three orthogonal directions, $tr\{\cdot\}$ represents matrix trace, $\|\cdot\|$ is matrix norm and $\boldsymbol{I}$ is a 3×3 unit-diagonal matrix. The solution to (3.1) is

$$\boldsymbol{W}(\boldsymbol{r}) = [\boldsymbol{w}_x(r), \boldsymbol{w}_y(r), \boldsymbol{w}_z(r)] = \|\boldsymbol{L}(\boldsymbol{r})\|\boldsymbol{R}^{-1}\boldsymbol{L}(\boldsymbol{r})[\boldsymbol{L}^{\boldsymbol{T}}(\boldsymbol{r})\boldsymbol{R}^{-1}\boldsymbol{L}(\boldsymbol{r})]^{-1}. \tag{3.2}$$

In this study, the Frobenius norm was used for $\|\cdot\|$. The covariance matrix was derived from MEG data, which was regularised with a diagonal matrix to deal with the singularity of the covariance matrix. The regularisation parameter was $\delta = 1\% \cdot tr(\boldsymbol{R})$ and the regularised covariance matrix was expressed as $\widetilde{\boldsymbol{R}} = \boldsymbol{R} + \delta \cdot \boldsymbol{I}$.

A 5 mm resolution of the scan grid was used to scan the whole brain and, at each scanned grid location, the vector beamforming reconstructed source time courses on three orthogonal directions. At location $\boldsymbol{r}$, the reconstructed time course was

$$s_x(\boldsymbol{r}) = \boldsymbol{w}_x^T(\boldsymbol{r}) \cdot \boldsymbol{X};\; s_y(\boldsymbol{r}) = \boldsymbol{w}_y^T(\boldsymbol{r}) \cdot \boldsymbol{X};\; s_z(\boldsymbol{r}) = \boldsymbol{w}_z^T(\boldsymbol{r}) \cdot \boldsymbol{X}. \tag{3.3}$$

The three orthogonal time courses $\boldsymbol{s} = [s_x \quad s_y \quad s_z]^T$ were projected onto the optimal orientation with the maximum power on each grid. Singular value decomposition was applied to the covariance matrix of the three output time series $\boldsymbol{s} \cdot \boldsymbol{s^T}$,

$$\boldsymbol{M} = \boldsymbol{s} \cdot \boldsymbol{s^T} = \boldsymbol{U} \cdot \boldsymbol{\Sigma} \cdot \boldsymbol{V^H}, \tag{3.4}$$

where the columns of matrices $\boldsymbol{U}$ and $\boldsymbol{V}$ are left and right singular vectors, respectively, and $\boldsymbol{V^H}$ is the conjugate transpose of matrix $\boldsymbol{V}$. The diagonal elements of matrix $\boldsymbol{\Sigma}$ are singular values, which were ranked by decreasing order with common convention. The orientation with the maximum power is the left singular vector corresponding to the maximum singular value $\boldsymbol{\gamma} = \boldsymbol{u}_1$, where $\boldsymbol{u}_1$ is the first column of matrix $\boldsymbol{U}$. Thus, the brain source activity at a scanning position $\boldsymbol{r}$ is

$$s(\boldsymbol{r}) = \boldsymbol{\gamma} \cdot \boldsymbol{s} = \boldsymbol{\gamma} \cdot [s_x \quad s_y \quad s_z]^T. \tag{3.5}$$

The number of scanned grid nodes across all of the patients in this study was of the order of 10^5. These scanned nodes resemble implanted sensors monitoring brain activities, on which kurtosis (g2) was measured to detect outliers present in brain activity, which can be highly associated with inter-ictal spikes (Robinson et al., 2004; Kirsch et al., 2006; Oishi et al., 2006). The kurtosis of a time series $S(t)$ is expressed as

$$g_2 = \sum_T \frac{[S(t) - \bar{S}]^4}{\sigma^4 T}, \tag{3.6}$$

where $\bar{S}$, σ and T are the mean, standard deviation and temporal length of the time series, respectively.

To obtain a stable estimate of the covariance matrix used for beamforming, we performed beamforming on 3 min of MEG data (Brookes et al., 2008). For each 3 min segment, we performed the beamforming with a 5 mm resolution scanning grid on which kurtosis were measured, and obtained a g2-distribution across the brain. An example of the g2-distribution is shown in Figure 3-1. All the local maxima of the g2-distribution were considered to be virtual sensors (VSs), which are demonstrated by pink dots in Figure 3-1. The numbers assigned to the VSs are the ranks of their kurtosis across the g2 value across all of the VSs.

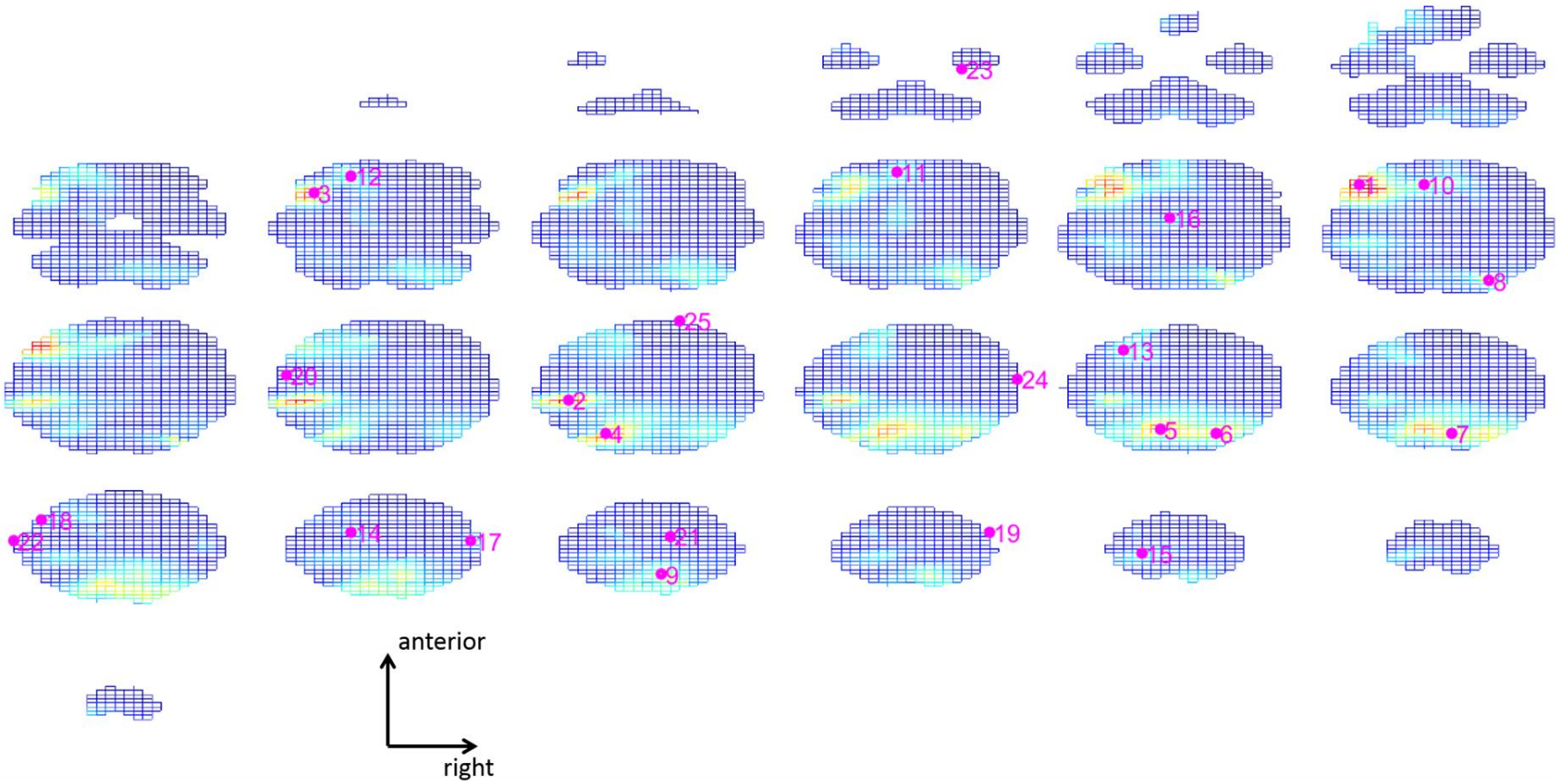

Figure 3-1 A g2-distribution generated by beamforming. This figure is composed of g2-distribution on 24 slices of the brain from bottom to top, which is arranged in this figure from left to right and from first row to last row. For each slice, the coordinate of the brain is shown in the last figure where the upward direction is the anterior of the brain and the right direction points to the right side of the brain. The colours show the values of g2, where red represents high g2 values and blue indicates low g2 values. All the local maxima of the g2-distribution (virtual sensors, VSs) are indicated by pink dots with number that give the rank of the kurtosis of the VS among all the VSs inside the brain.

We performed beamforming on a block of continuous MEG recordings with a non-overlapping 3 min sliding time window, which is illustrated in Figure 3-2. At the end of each block, we allowed the overlapping between the last two sliding windows, and this overlap is illustrated by the grey colour in Figure 3-2. We obtained multiple g2-distributions and their VSs for each patient. As can be seen in Figure 3-2, the g2-distributions from different segments for one patient had various distributions. We can denote the g2-distribution in segment i as $m_{g_2}^i$, which is a three-dimensional matrix and each element $m_{g_2}^i(\boldsymbol{r})$ is the value of kurtosis measured on the reconstructed time series from beamforming at location $\boldsymbol{r}$. To obtain the localisation results from various g2-distributions, we explored four solutions.

3.2.2 Solution 1: Voxels with maximum kurtosis on the summed g2-images

One straightforward solution is to sum up all the g2-distributions and the location with maximum kurtosis in the summed g2-distribution is the localized solution. Solution 1 can be expressed as

$$S_1: \max_{\boldsymbol{r}=v_{s1}} \sum_{i=1}^{M} m_{g_2}^i(\boldsymbol{r}), \tag{3.7}$$

where M is the number of 3 minutes segments of pre-processed MEG data, and the g2-distribution generated in each segment is $m_{g_2}^i(\boldsymbol{r})$, where $\boldsymbol{r}$ is the location of a voxel. The solution is the voxel v_{s1} that maximizes the summed g2-distribution across all the segments.

3.2.3 Solution 2: Voxels with maximum kurtosis on the summed g2-images with 1 s sliding window

The statistical parameter kurtosis is used to detect the interictal spike present in the time series, which is biased to the infrequent spikes. The bias can be eliminated by a sliding window. Scott et al. recommended the optimal sliding window length is 1 second (Scott et al., 2016). In our study, we used this suggested sliding window length and adopted the voxels with the maximum summed kurtosis value with the 1 second sliding window. Solution 2 is

$$S_2: \max_{\boldsymbol{r}=v_{s2}} \sum_{i=1}^{M_{1S}} m_{g_2,1S}^i(\boldsymbol{r}), \tag{3.8}$$

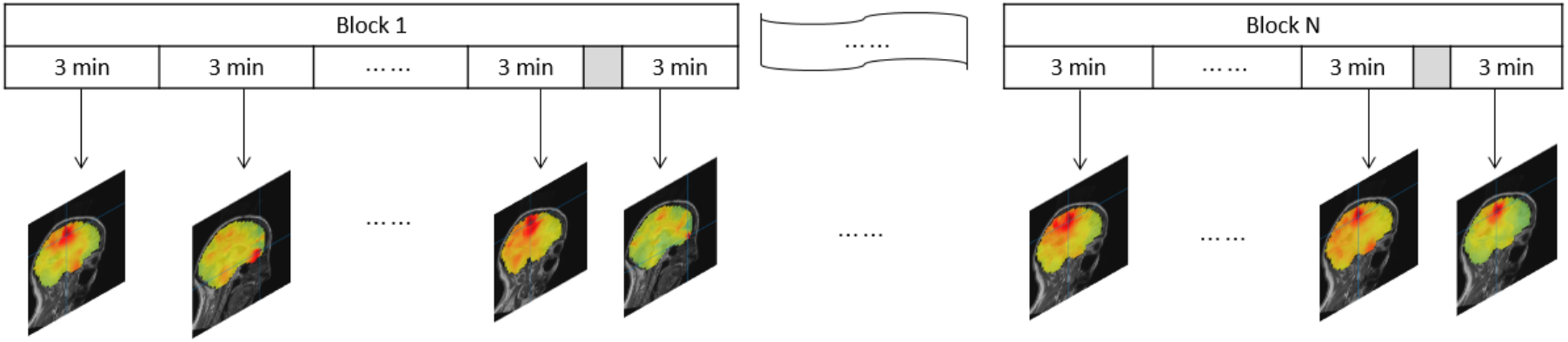

Figure 3-2 Multiple g2-distributions of one patient generated using beamforming. The first row shows the continuous recorded MEG blocks, on which beamforming was performed with a 3 min sliding window. There was no overlap between sliding windows except for the two windows at the end of each block, which are highlighted by the grey colour. In each 3 min sliding window, beamforming was applied to generate g2-distributions. Sagittal planes of the brain g2-distributions are shown in the second row. The colour in this map shows the value of kurtosis. Red represents high g2 values and green represents small g2 values.

where M_{1s} is the number of one second sliding windows along the MEG data used to perform localisation and $m^{i}_{g_2,1s}(\boldsymbol{r})$ is the g2-distribution in each 1 s sliding window. Solution 2 is the voxel v_{s2} that maximizes the summed g2-distribution with the sliding window.

3.2.4 Solution 3: Virtual sensor with maximum kurtosis

Another solution is the VS with the maximum kurtosis value among all the VSs of each patient. Solution 3 can be expressed as

$$S_{3:}\max_{j} g_2(s_{VS_j}), \quad VS_j \in A_{vs}, \tag{3.9}$$

where $g_2(s_{VS_j})$ is the kurtosis measured from the time series of the jth VS s_{VS_j} and A_{vs} is the set including all of the VSs obtained from one patient across all the segments. Note, the time series of VSs were visually inspected to ensure the VS contained authentic spikes without being contaminated by artefacts

3.2.5 Solution 4: Regions with persistent interictal spikes

This solution is the brain regions with the most persistent interictal spikes. First, we visualized time courses of VS with g2 above a threshold and determined VSs related to spikes. The threshold of VS selection is introduced in Section 0. Then, we performed three-dimensional segmentation on the g2-distributions and obtained VS-regions, which are the 3D regions around each of the VSs. The three-dimensional region around VS_j can be expressed as R_{VS_j}. The three-dimensional segmentation method is illustrated in Section 3.2.5.2 . The interictal spike map in the ith segment is m^{i}_{s} comprised of all the R_{VS_j} whose VSs were associated with interictal spikes defined in the first step; specifically,

$$m^{i}_{s}(v) = \begin{cases} 1 & v \in R_{VS^{s}_{j}} \\ 0 & v \in R_{VS^{ns}_{j}} \end{cases}, \tag{3.10}$$

where VS^{s}_{j} is the jth virtual sensor and is associated with interictal spikes, while VS^{ns}_{j} is the jth virtual sensor and is irrelevant to interictal spikes (non-spike). $R_{VS^{s}_{j}}$ and $R_{VS^{ns}_{j}}$ are regions segmented for virtual sensors VS^{s}_{j} and VS^{ns}_{j}, respectively. Equation (3.10) demonstrates that the voxel of the interictal spike map in the ith segment is 1 if the voxel lies in the segmented

region around a VS associated with interictal spikes, while the value of a voxel is 0 if it lies in the segmented regions around a VS unrelated to interictal spikes.

Finally, we obtained the count-map denoted by m_c, which shows the total times that a voxel was associated with interictal spikes. The count-map can be expressed as

$$m_c(v) = \sum_{i=1}^{M} m_s^i(v), \tag{3.11}$$

where M is the number of segments. Thus, we obtained a count-map that showed how many times one voxel was associated with interictal spikes across all the segments. Solution 4 is voxels v_{s3} with the maximum value in count-map, which are brain regions with the most persistent interictal spikes, expressed as

$$S_3: \max_{v_{s3}}\{m_c(v)\}. \tag{3.12}$$

3.2.5.1 VS selection

The g2-threshold was generated using the elbow method, which was the elbow point of the curve when all the g2 values on the scanned voxels were plotted in descending order. The elbow method was originally used in classification scenarios to determine the optimal number of clusters (Ketchen & Shook, 1996). One example of the determination of the optimal number of clusters is shown in Figure 3-3-(a) where the x-axis is the number of clusters and the y-axis is the corresponding value of the cost function. The elbow point of the curve is illustrated as a red dot in Figure 3-3(a), which is the smallest distance from each point on the curve to the orange dashed line that connects the first and the last points of the curve.

We also used the elbow method to find the number of voxels such that increasing the inclusion of more voxels did not contribute to a significant increase of kurtosis value. An example of the elbow method used to define the optimal number of included voxels is shown in Figure 3-3(b), in which the blue curve depicts the kurtosis values on all the scanned voxels in descending order. The red point on the curve represents the elbow point, which has the shortest distance to the dashed orange line that connects the first and the last points of the curve. The optimal number of voxels in this example is 1364 and its corresponding g2 is 4.25, which we can use as the g2-threshold to select a set of VSs as epileptic spike location candidates. We can denote the g2-threshold generated from the elbow method as g_{2e}. To include enough VSs, we imposed

an upper limit of the g2-threshold to be 4. Thus, the kurtosis threshold used to select VSs was min $\{g_{2e}, 4\}$.

We examined the effect of the end point of the curve in Figure 3-3(b) on the elbow method to evaluate the robustness of the elbow method. We can define the total amount of voxels in one g2-distribution as n_v. We investigated the number of selected VSs with the end of the curve varying from 6000 voxels to n_v voxels with step 100, which is illustrated in Figure 3-4. The dashed lines in the figure show the lines connecting the start point and the end points with varying included voxels, on which the elbow points were determined. The number of selected VSs with changing end points are expressed as $\left[n_{6000}^{BF_i} \quad n_{6100}^{BF_i} \quad \cdots \quad n_{n_v}^{BF_i}\right]$ for one beamforming segment BF_i.

We can measure the variability of the number of selected VSs using the standard deviation, which can be expressed as $\sigma^{BF_i} = \text{std}\{\left[n_{6000}^{BF_i} \quad n_{6100}^{BF_i} \quad \cdots \quad n_{n_v}^{BF_i}\right]\}$, where std$\{\cdot\}$ is standard deviation. σ^{BF_i} can demonstrate the variability introduced by varying end points of the curve. We illustrate σ^{BF_i} across all the beamforming segments for each patient in Section 3.3.1 .

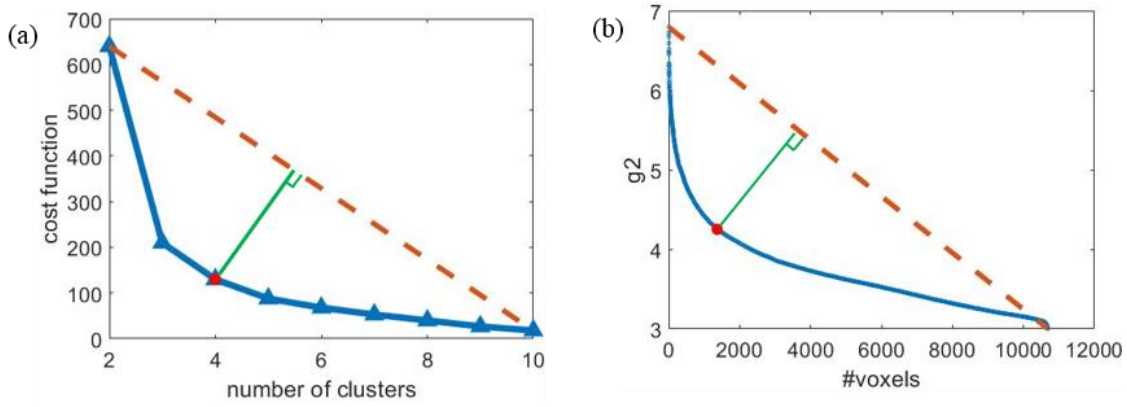

Figure 3-3 Elbow methods for determining (a) optimal cluster numbers and (b) g2-threshold. The blue curve with triangular markers in (a) is the value of the cost function, which reduces with increasing numbers of clusters. The blue curve in (b) depicts kurtosis magnitudes on all the scanned voxels in descending order. The red dots in the figures represent elbow points of the two curves. The green solid lines indicate the shortest distances from blue curves to the dashed orange lines, which connect the first and the last points of the curves.

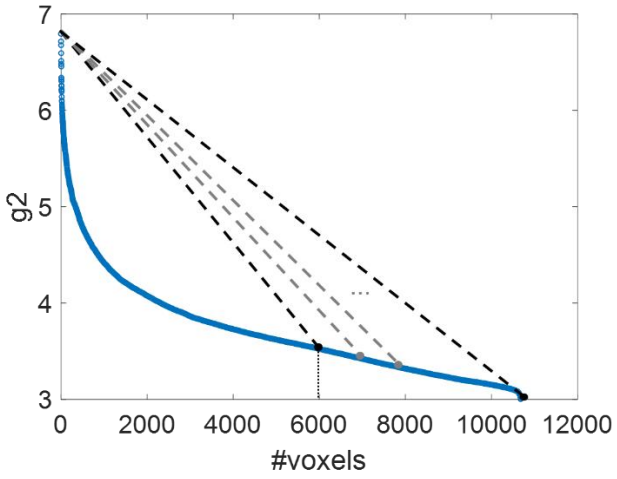

Figure 3-4 The effect of the end point on VSs selection. The blue curve in this figure is the same as the curve in Figure 3-3 (b). The end point of the curve changes from the voxel number 6000 to the total number of voxels, which are indicated by black dots on the curve. The other end points are shown by grey dots between them. The dashed lines in this figure connect the start point with the end point of the curve.

3.2.5.2 Three-dimensional segmentation of the g2-image

We performed three-dimensional segmentation on the g2-distribution shown in Figure 3-1. The three-dimensional segmentation method used here is region growing (Adams & Bischof, 1994; Zaitoun & Aqel, 2015). The seeds applied were all the local maxima, which are the VSs, of the g2-distribution. The corresponding segmented region of each VS is called a VS-region.

For each VS-region, the initial area was the voxel where the VS is located, $R_1 = v_{\mathrm{vs}}$. At step two, the growing region R_2 was first set to be R_1. Then, we examined all the neighbouring voxels of R_2, which were defined as the 26 connected voxels around it, shown in Figure 3-5. We denote the neighbouring area of this VS as N_{vs}. The examined condition was $g_2(v_{N_{\mathrm{vs}}}) < g_2(v_{\mathrm{vs}})$. This inequality ensures the kurtosis distribution in each segmented region is less than the seed of each region; thus, we denote this condition as the g2 gradient-descent condition. If the g2 gradient-descent condition was met, the voxel $v_{N_{\mathrm{vs}}}$ was merged into R_2. If not, the voxel $v_{N_{\mathrm{vs}}}$ was merged into R_o, which represented the region outside of this VS-region. This process was repeated until all the voxels in N_{vs} were examined.

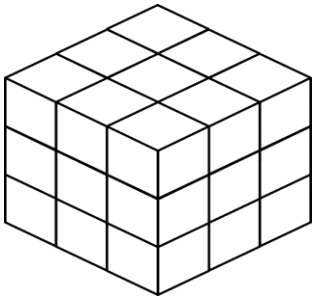

Figure 3-5 The neighbour region of a voxel. The voxel is located at the centre cube location and its neighbouring voxels are the 26 voxels around it.

The flow chart of this method for iterative step n is shown in Figure 3-6. At the nth step of the method, the region R_n was initially set to be the region of the last step R_{n-1}. We performed neighbourhood inclusion and condition examination on the voxels included in step $n-1$, which can be defined as the boundary of step $n-1$ and expressed as $B_n = R_{n-1} \cap \bar{R}_{n-2}$. R_{n-2} is the region defined at step $n-2$ and $\bar{R}_{n-2}$ is the area outside of the region R_{n-2}. For a voxel v_i in area B_n, we included voxels located in the neighbouring area defined in Figure 3-5 and excluded voxels in areas R_o and R_{n-1}. Because voxels in R_o and R_{n-1} have been examined in previous steps. Thus, the voxels v_{ij} in area $A_i = N_i \cap \bar{R}_o \cap \bar{R}_{n-1}$ were examined by the g2 gradient-descent condition. If the condition $g_2(v_{ij}) < g_2(v_i)$ was satisfied, v_{ij} was included in R_n. If this condition was not satisfied, v_{ij} was included in R_o. We repeated this procedure for all the voxels in area B_n and obtained the final R_n in step n. The stop condition for this iterative process was that the segmented regions in iterative step n and $n-1$ were the same. An example of the segmented area for one VS, VS-region, is shown in Figure 3-7, in which the seed is the VS highlighted by the colour green. Because all the VSs were local maxima, this VS-region only covers VS1 without enclosing all of the other VSs.

The VS-regions generated with the region growing method could not prevent intersections between different VS-regions. To obtain non-overlapping segmented areas, we only included voxels that exclusively lay in one segmented region as the VS-region. The VS-region with exclusive voxels for the VS-region shown in Figure 3-7 is illustrated in Figure 3-8. The VS-region with exclusive voxels shrank substantially compared with the VS-region in Figure 3-7. In the following analysis, we use the shrunk VS-region for each VS, which will be referred as VS-region for convenience.

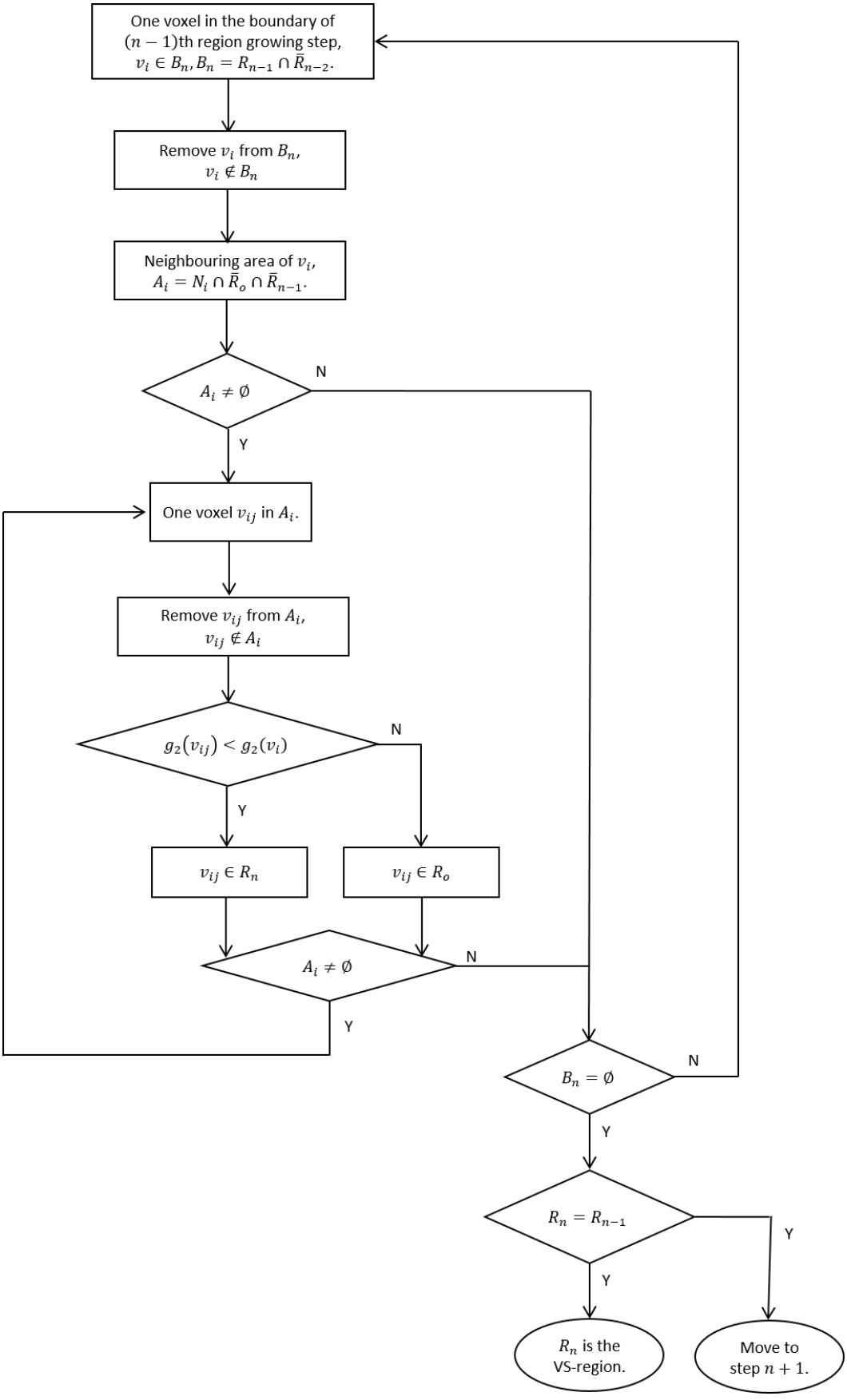

Figure 3-6 Flow chart of the region growing method. The nth step of region growing method used for three-dimensional segmentation.

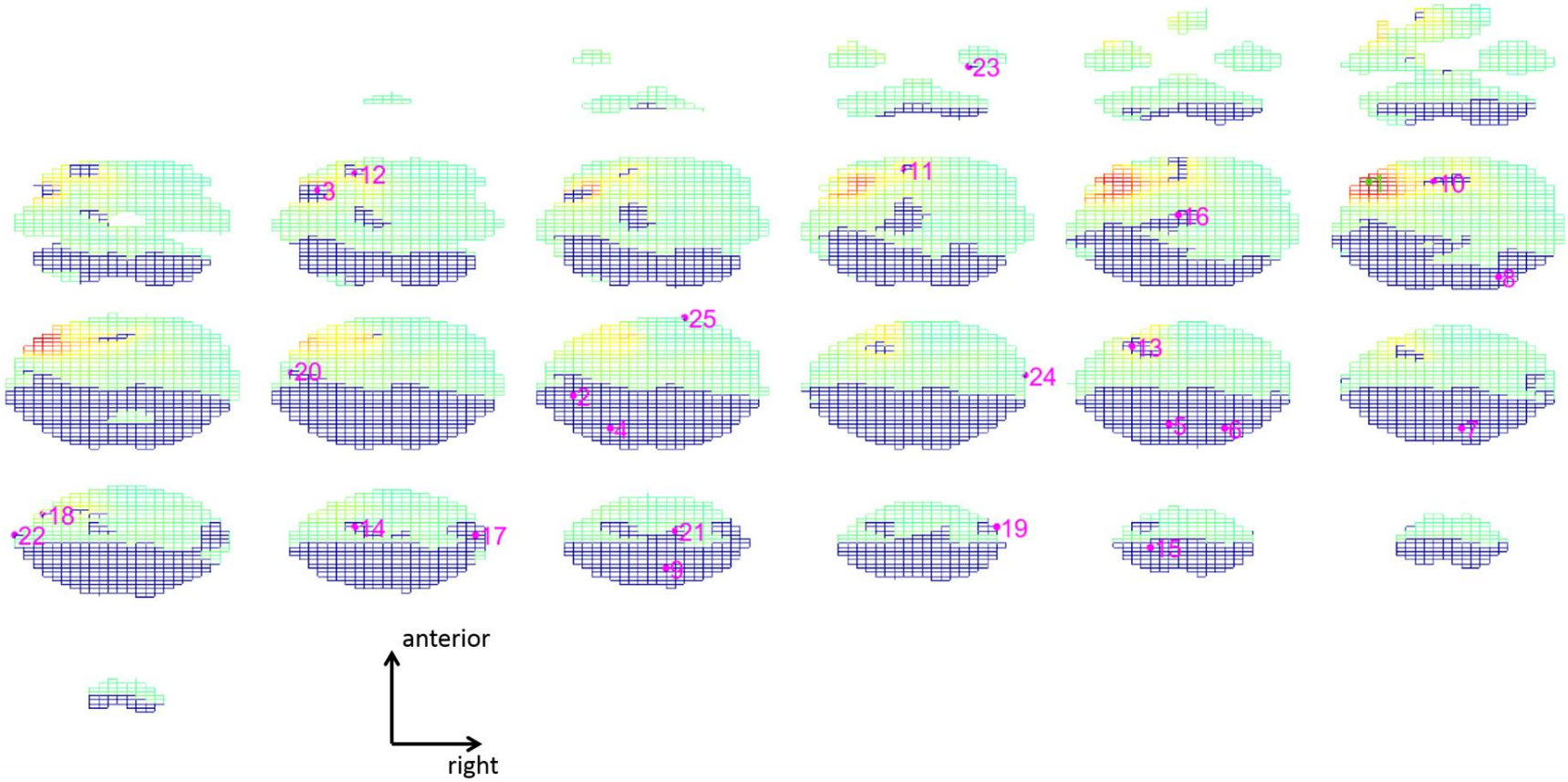

Figure 3-7 VS-region for VS1. This is a region-growing segmentation result for one seed VS1, shown by the green dot located on the last slice of the second row. The deployment of brain slices, the coordinates of the head and the colour map are the same as Figure 3-1. The segmented VS-region for VS1 is shown as the area highlighted by light blue, yellow and red. All the VSs are shown as pink dots. The brain area outside of this VS-region is shown by the blue grid that does not have any other colours.

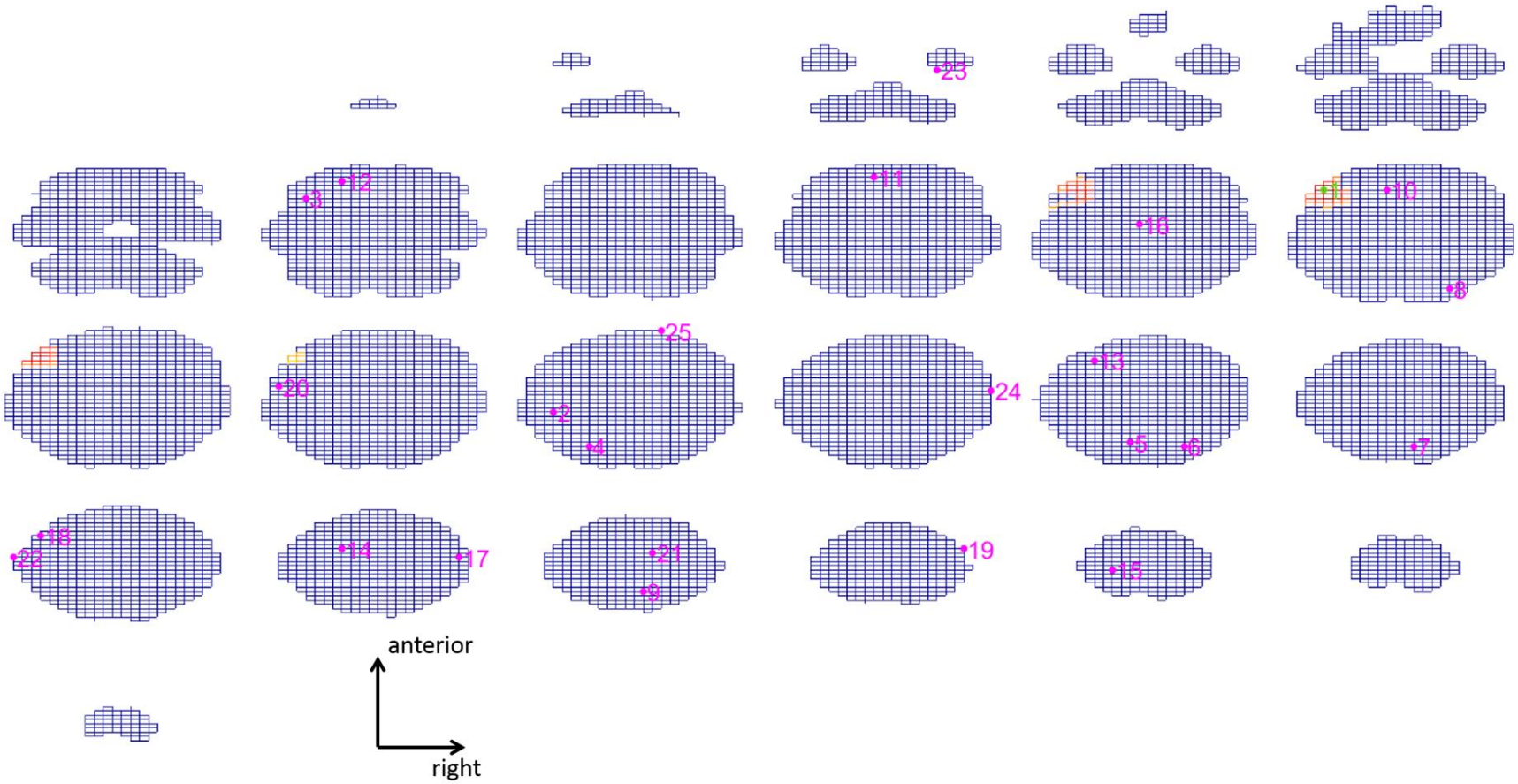

Figure 3-8 Shrunk VS-region. The VS-region with exclusive voxels generated for VS1, which is highlighted by the colour green. This figure, including the deployment of brain slices, the coordinates of the head and the colour map, is the same as Figure 3-7, while in this figure, the segmented area only includes voxels exclusively covered by this VS-region.

3.3 Results

3.3.1 The effects of the changing end point to the elbow method

For Solution 4, we selected VSs using a threshold, which is the kurtosis value at the elbow point introduced in Section 0. The elbow point is defined as the point on a curve having the minimum distance to the line connecting the start point and the end point of the curve. In this section, we quantify the effects of the varying end point of the curve on the number of VSs selected for all the beamforming segments in our patient cohort. The variability contributed by the various end points in the ith beamforming segment were measured by the standard deviation and denoted as σ^{BF_i}. For a patient with N segments, we obtained a set of standard deviations $[\sigma^{BF_1} \quad \cdots \quad \sigma^{BF_N}]$, from which the violin plot was generated (see Figure 3-9).

In each violin plot, the white dot represents the median, and the violin shaped curves along the two sides show the kernel density estimated from the data. The thick grey bar in the centre displays the interquartile range (the 25th percentile and the 75th percentile), while the thin grey bar indicates the range of the data excluding outliers.

As seen from the upper edge of the thick grey bar inside the violin shape, the 75th percentiles of the data are zero (0) for three patients (P007, P016 and P061) and within the range [1, 2] for ten patients (P012, P035, P037, P040, P040, P046, P049, P070, P072, P074), among which the 75th percentile for P035 is 2.07, slightly greater than 2. Thus, the contribution of the changing end point to the variability of the number of selected VSs is less than 2 VSs in 75% percent of

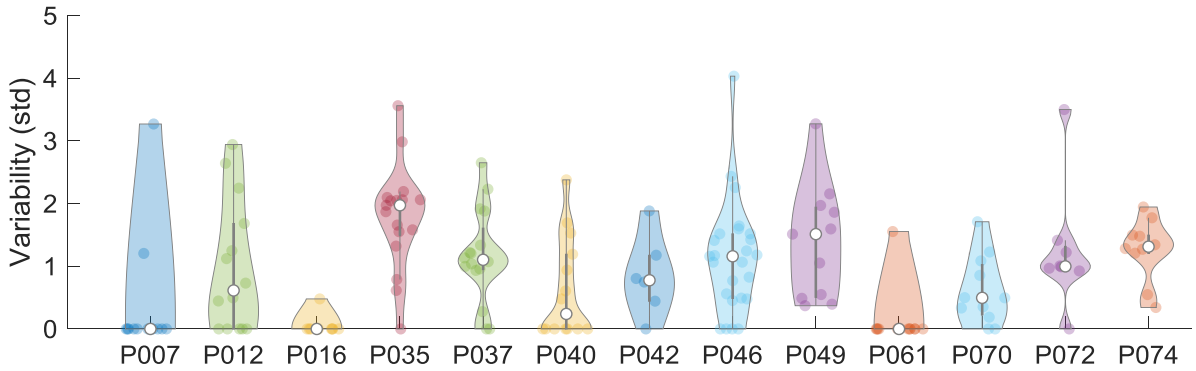

Figure 3-9 Variabilities introduced by changing end points. Violin plots illustrating the variability of the number of selected VSs with changing end points. Each dot represents the standard deviations of the varying numbers of selected VSs contributed by changing the end points of the curve for one beamforming segment. The thick grey bars inside the violins show the range spanning the 25th and 75th percentiles, and the thin grey bars indicate the distribution of data not including outliers. The medians of the data are indicated by white dots with grey outlines.

beamforming segments across all the patients. We can conclude that changing the end point of the curve used in the elbow method does not lead to dramatic changes to the number of VSs included for the following analysis.

3.3.2 Localized regions of solutions 1, 2, 3 and 4

We examined the concordance between each solution applied in this study with three validations introduced in Section 2.4 : the clinical onset, the clinical propagation and the surgical resection, shown in Table 3-1. "Con" classification represents the localized region being consistent with the validation. "Dis" classification is where the localized region was not consistent with the validation. "Partially-con" classification is used when multiple regions present in validations, and the localisation methods cover a subset of them. All the "Concordant" and "Partially-con" are highlighted by the light blue in this table.

The localized regions of four solutions for Patient P007 are shown in Figure 3-10. The four source solutions were projected onto the brain surface and their corresponding MRI images are shown in the subfigures. All the MRI images in this chapter are shown with left is left side of the brain and right is right side of the brain. The colour maps show the higher values as yellow and lower values as red. Solution 1 is shown in Figure 3-10(a) as a spherical region centred at the voxel v_{s1} with radius 25mm; the colour map shown is the summed g2-distributions across all the segments normalized by the number of segments. Solution 2, shown in Figure 3-10(b), is also shown by a sphere with radius 25mm but centred at voxel v_{s2}. The colour map registered on the brain surface and the MRI image are the averaged kurtosis across all the 1 second sliding windows. Solution 3, shown in Figure 3-10(c), is a 25mm^3 cube cantered at the VS with the maximum kurtosis across all the segments. The maximum kurtosis value is 25.62 shown above the MRI image. Solution 4 in Figure 3-10(d) shows the regions where persistent interictal spikes were present; the colour map depicted in this figure is the same as the colour map for Solution 1. The depictions of the four solutions for all the patients in this study are similar in format to the results illustrated for Patient P007.

The validations for Patient P007 are shown in Figure 3-10(e), in which the clinical EEG-MEG source localisation (EMSL) localized to the bitemporal lobe is indicated by the pink discs. Solution 1 and Solution 3 co-localized to the right side of the clinical onset and missed the left onset; thus, we classified the concordance as "Partially-con". Also, because this patient did not show propagations in clinical EEG-MEG source localisation, the validations between three of the solutions and clinical propagation are indicated as "-" for this patient in Table 3-1, which

Table 3-1 Validations of Solution 1, Solution 2, Solution 3 and Solution 4 with clinical onset, clinical propagation and surgical resection. The localisation validations of each patient are listed along with the four solutions. The last column shows the surgical outcome. Each solution was validated against the clinically localized onset regions and propagation regions, which are indicated as "Clinical O" and "Clinical P", respectively. The concordant validation results are indicated by "Con" and highlighted by the colour blue in this table. "Partially-con" indicates the localised results cover references, but not fully cover.The discordant validations are indicated by "Dis". The seizure free surgical outcome (Engel I) is indicated by "free" in the last column, while "Non-free" represents the patient has persistent seizures after surgery (Engel II-IV). We also concluded the concordance of one solution with one validation as "Dis" if the solution covered more regions than the validation areas, e.g. P012 and P070.

Pat	Solution1			Solution 2			Solution 3			Solution 4			Surgical outcome
	Clinical O	Clinical P	SR	Clinical O	Clinical P	SR	Clinical O	Clinical P	SR	Clinical O	Clinical P	SR	
P007	Partially-con	-	Dis	Dis	Dis	Dis	Partially-con	-	Dis	Dis	-	Dis	Non-free
P012	Dis	Con	Dis	Dis	Con	Dis	Dis	Dis	Dis	Dis	Dis	Dis	free
P016	Dis	Dis	Dis	Dis	Con	Con	Dis	Dis	Dis	Dis	Con	Con	free
P035	Dis	Con	Dis	Dis	Con	Dis	Dis	Dis	Dis	Dis	Con	Dis	free
P037	Dis	Dis	Dis	Con	Con	Con	Dis	Dis	Dis	Con	Dis	Con	free
P040	Dis	Dis	Dis	Dis	Dis	Dis	Dis	Dis	Dis	Dis	Dis	Dis	Non-free
P042	Dis	Dis	Dis	Dis	Dis	Dis	Dis	Dis	Dis	Dis	Dis	Dis	free
P046	Dis	-	Dis	Dis	-	Dis	Dis	-	Dis	Dis	-	Dis	Non-free
P049	Dis	Dis	Dis	Dis	Dis	Dis	Dis	Dis	Dis	Dis	Dis	Dis	Non-free
P061	Dis	Con	Con	Dis	Con	Con	Dis	Con	Con	Dis	Con	Con	free
P070	Dis	Dis	Dis	Dis	Dis	Dis	Dis	Dis	Dis	Dis	Dis	Dis	free
P072	Dis	Dis	Dis	Con	Dis	Con	Dis	Dis	Dis	Dis	Dis	Dis	free
P074	Dis	Dis	Dis	Dis	Dis	Dis	Dis	Dis	Dis	Dis	Dis	Dis	free

is the same as P046 since this patient also did not show clinical propagations. Patient P007 had left baso-mesial temporal lobe resected, shown in Figure 3-10(e) by the blue surface covering on the brain. This surgical outcome of this patient was classified as Engel II, which was not seizure-free, as indicated in the last column of Table 3-1. All four solutions were discordant with the surgical resection.

For Patient P012, localized results of Solutions 1, 2, 3, 4 are shown in Figure 3-11(a), (b), (c) and (d), respectively. Solution 1 and Solution 2 localized to parietal convexity and right parietal lobe, respectively, while Solution 3 was localized to right parietal lobe. Solution 4 generated an extended source including parietal convexity, right parietal lobe and left occipital lobe. Solution 1 co-localized with clinical spike propagation. Even though Solution 4 also covered the clinical propagation area, the concordance between Solution 4 and the clinical propagation is "Dis" because localized regions of Solution 4 spread out and covered more regions. The surgical resection of this patient was at left paracentral lobule, which was not localized by all the four solutions, and the patient was seizure free after surgery.

For Patient P016, the localisation results are shown in Figure 3-12. The localized regions of Solution 1 and Solution 3 are discordant with the clinical solutions and the surgical resection. Solution 2 and Solution 4 are concordant with clinical propagation and the surgical resection. It is shown in Figure 3-13 that Solution 1, Solution 2 and Solution 4 of Patient P035 were localized to the clinical spike propagation, while Solution 3 was discordant with clinical solutions and the surgical resection. The patient was seizure free after surgery.

The localized regions of Solutions 1, 2, 3 and 4 of Patient P037 are shown in Figure 3-14(a), (b), (c) and (d), respectively. Solution 1 and Solution 3 mis-localized to temporal lobe, which is discordant with all the validations, while Solution 2 and Solution 4 localized to the clinical spike onset and surgical resection, pre-central gyrus. This patient achieved seizure freedom after surgery.

The localisation results of the four solutions for Patient P040 are shown in Figure 3-15. The localized areas of all four solutions were discordant with any validations. This patient had post-surgical persistent seizures.

For Patient P042, Solutions 1, 3, 4 (see Figure 3-16) were localized to universal locations left parietal convexity, and Solution 2 was localized to the left posterior temporal lobe. None of the solutions were concordant with any validations for this patient. This patient achieved seizure-free surgical outcome.

For Patient P046, all four solutions localized to a universal location left anterior temporal lobe shown in Figure 3-17, which was discordant with all validations. This patient had persistent seizures after surgical resection.

For Patient P049, the localized regions of all four solutions were inconsistent with all three validations, shown in Figure 3-18. However, Solution 3 localized to left inferior temporal lobe, which is the same lobe as the surgical resection and the clinically localized onset. This patient did not achieve seizure freedom after surgical resection.

The localisation results of Patient P061 is shown in Figure 3-19. As can be seen, Solutions 1, 2 and 4 were consistent with the clinical propagation and the surgical resection. Solution 3 was localized to temporal lobe, which was discordant with all the validations. This patient was seizure free after surgery.

For Patient P070, Solutions 1, 2 and 3, shown in Figure 3-20, were discordant with all validations. Even though Solution 4 localized to extended areas covering surgical resection, clinical onset and clinical propagation, we classified it as discordant with all the validations because this solution was more extended. This patient achieved seizure freedom after surgery.

For Patient P072, Solutions 1, 3 and 4, in Figure 3-21, were discordant with all validations, while Solution 2 was localized to the surgical resection and the clinically localized onset. This patient achieved seizure freedom after surgery.

For Patient P074, the four solutions, shown in Figure 3-22, were discordant with all the validations. This patient achieved seizure freedom after surgery.

In Table 3-2, we summarize the validations of the four solutions shown in Table 3-1. The number of patients and the patients list that obtained concordant results with each validation method are shown in this table. The first validation is the interictal spike onset region localized in clinic using EEG and MEG. Solutions 1, 3, and 4 have only one patient localized to the clinical onset, among which Solutions 1 and 3 achieved 'Partially-con', while Solution 2 localized to the clinical onset in two patients. The second concordance of validations used in Table 3-2 is 'Clinical results', which includes both clinical onset and propagation. For this validation, Solutions 1, 2, 3 and 4 obtained concordance in 4, 6, 2 and 3 patients, respectively. For the validation of surgical resections, Solution 1, 2, 3 and 4 achieved concordance in 1, 4, 1 and 3 patients, respectively. From this table, we can conclude that Solution 2 outperformed

Solutions 1, 3 and 4 in terms of clinical results but Solutions 2 and 4 outperformed Solutions 1 and 3 in terms of surgical cavity.

Table 3-2 Summary of Solution 1, Solution 2, Solution 3 and Solution 4 validated against clinical EEG-MEG source localisation and surgical resections. The number of patients with concordant localized results for each solution are listed along with the clinical onset, clinical results (including onset and propagation) and surgical resection validations. The patients list with concordant validations for each solution is also shown.

Solution	Clinical Onset	Clinical results (Onset/Propagation)	Surgical resection (overlap)	Surgical resection (epilepsy)
Solution 1	1 P007, Partially concordant	4 P007, Onset, Partially concordant P012, Propagation P035, Propagation P061, Propagation	1 P061	4 P012 P016 P035 P061
Solution 2	2 P037 P072	6 P012, Propagation P016, Propagation P035, Propagation P037, Onset and Propagation P061, Propagation P072, Onset	4 P016 P037 P061 P072	6 P012 P016 P035 P037 P061 P072
Solution 3	1 P007, Partially concordant	2 P007, Onset, Partially concordant P061, Propagation	1 P061	3 P016 P049 P061
Solution 4	1 P037	3 P016, Propagation P035, Propagation P061, Propagation	3 P016 P037 P061	4 P016 P035 P037 P061

P007

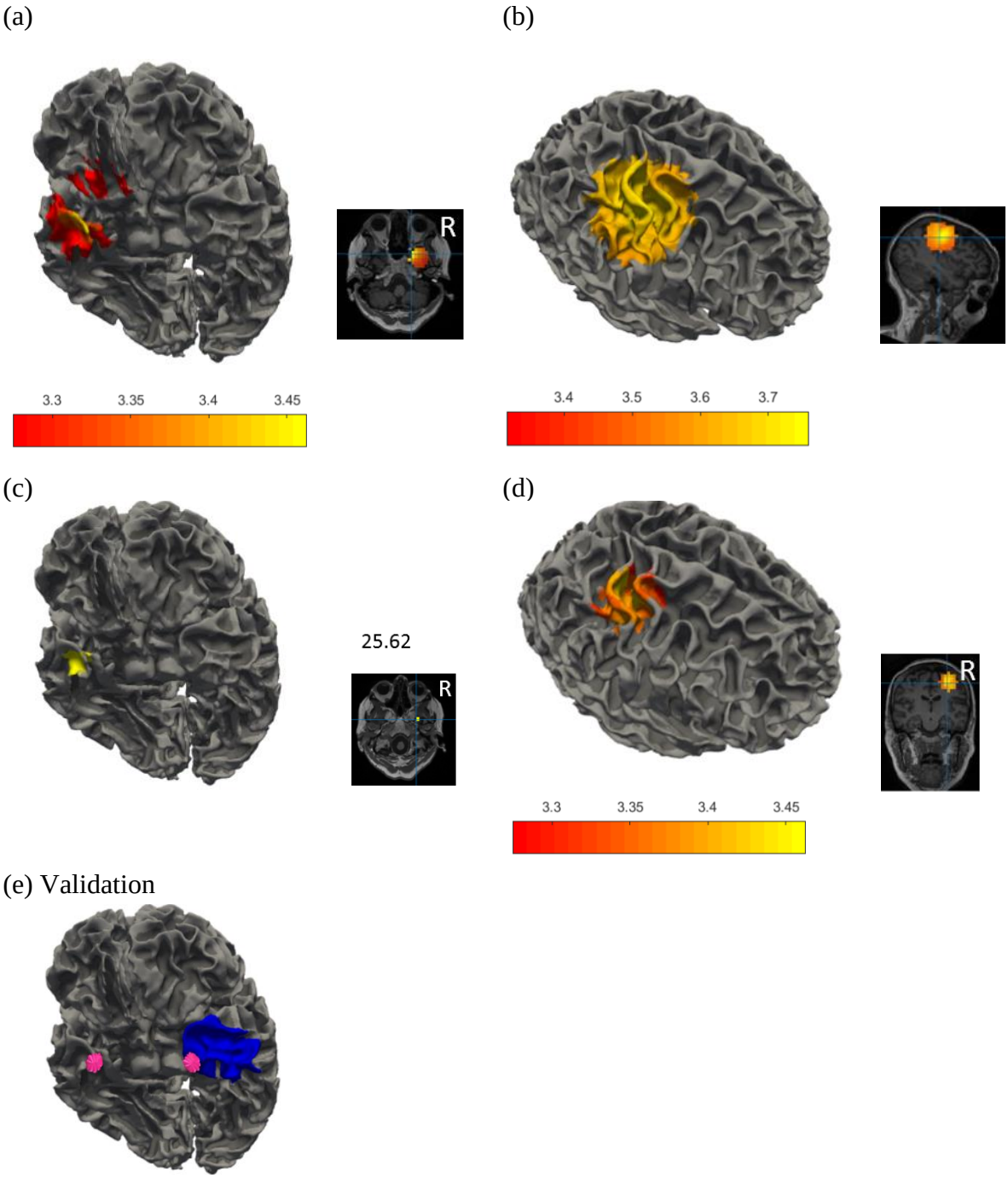

Figure 3-10 Source localisation for Patient P007 using Solution 1, 2, 3, 4 and validations. (a) Solution 1 and (c) Solution 3 with kurtosis value 25.62 were localized to the right mesial temporal lobe, which is consistent with one of the clinically localized areas. (b) Solution 2 and (d) Solution 4 were co-localized to right paracentral lobule. The subfigures of (a), (b), (c) and (d) show the corresponding sources registered onto the MRI images. In the colour maps shown in (a), (b) and (c), yellow represents the highest kurtosis value and red represents the lowest values. (e) The validations used in this study, in which surgically resected areas are indicated by the blue surface and pink discs indicate the clinically localized results. The clinical EEG-MEG source localisation was localized to bitemporal lobes for this patient.

P012

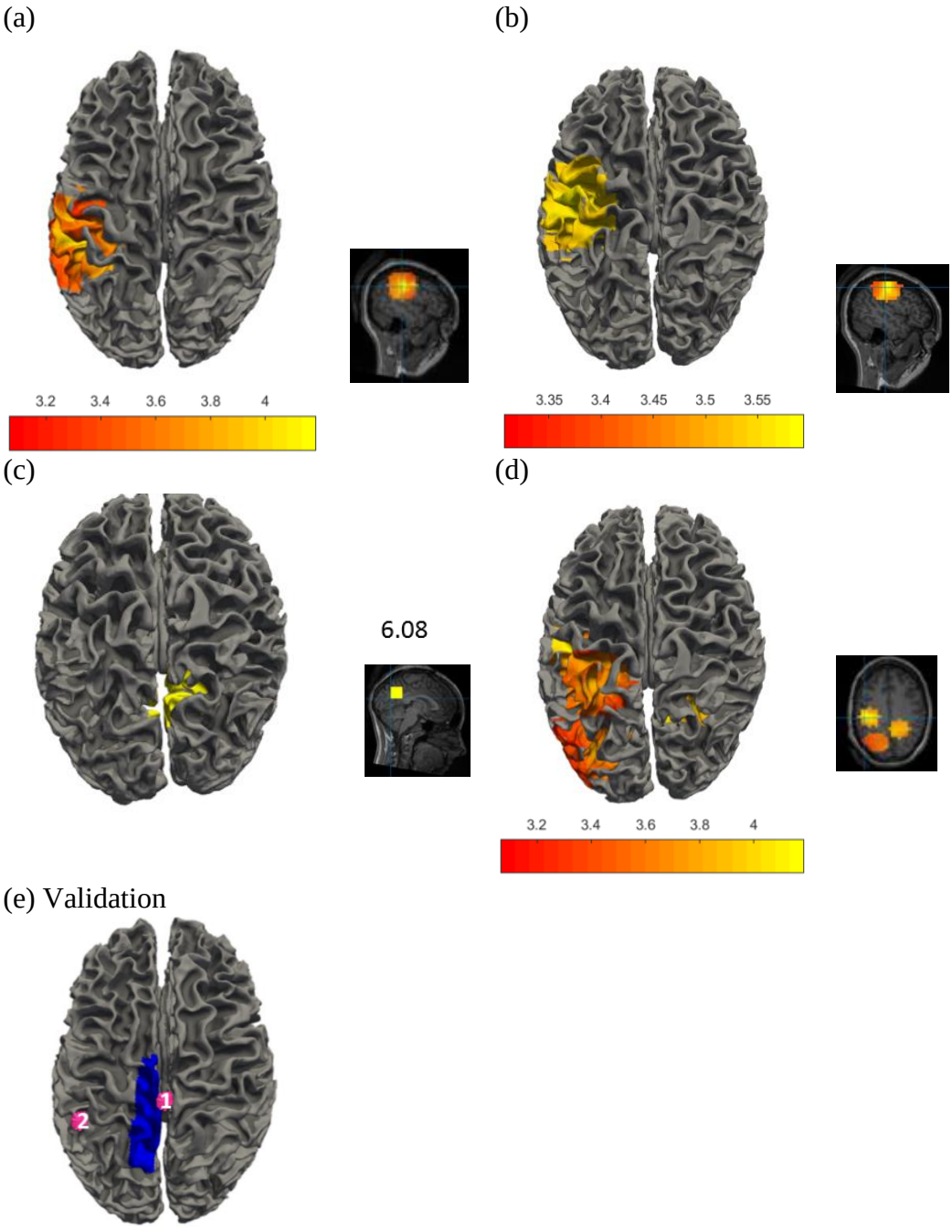

Figure 3-11 Source localisation for Patient P012 using Solution 1, 2, 3, 4 and validations. (a) Solution 1 and (b) Solution 2 were localized to the left parietal convexity concordant with the clinical propagation. (c) Solution 3 with kurtosis value 6.08 was localized the right parietal lobe. (d) Solution 4 are extending to left parietal convexity, right parietal lobe and left occipital lobe. The subfigures of (a), (b), (c) and (d) show the corresponding sources registered onto the MRI images. In the colour maps shown in (a), (b) and (c), yellow represents the highest kurtosis value and red represents the lowest values. (e) The validations used in this study, in which surgically resected areas are indicated by the blue surface and pink discs indicate the clinically localized results. The pink discs with number 1 and 2 demonstrate that the clinically localized interictal spikes originated from 1 paracentral lobule and later propagated to 2 left parietal convexity.

P016

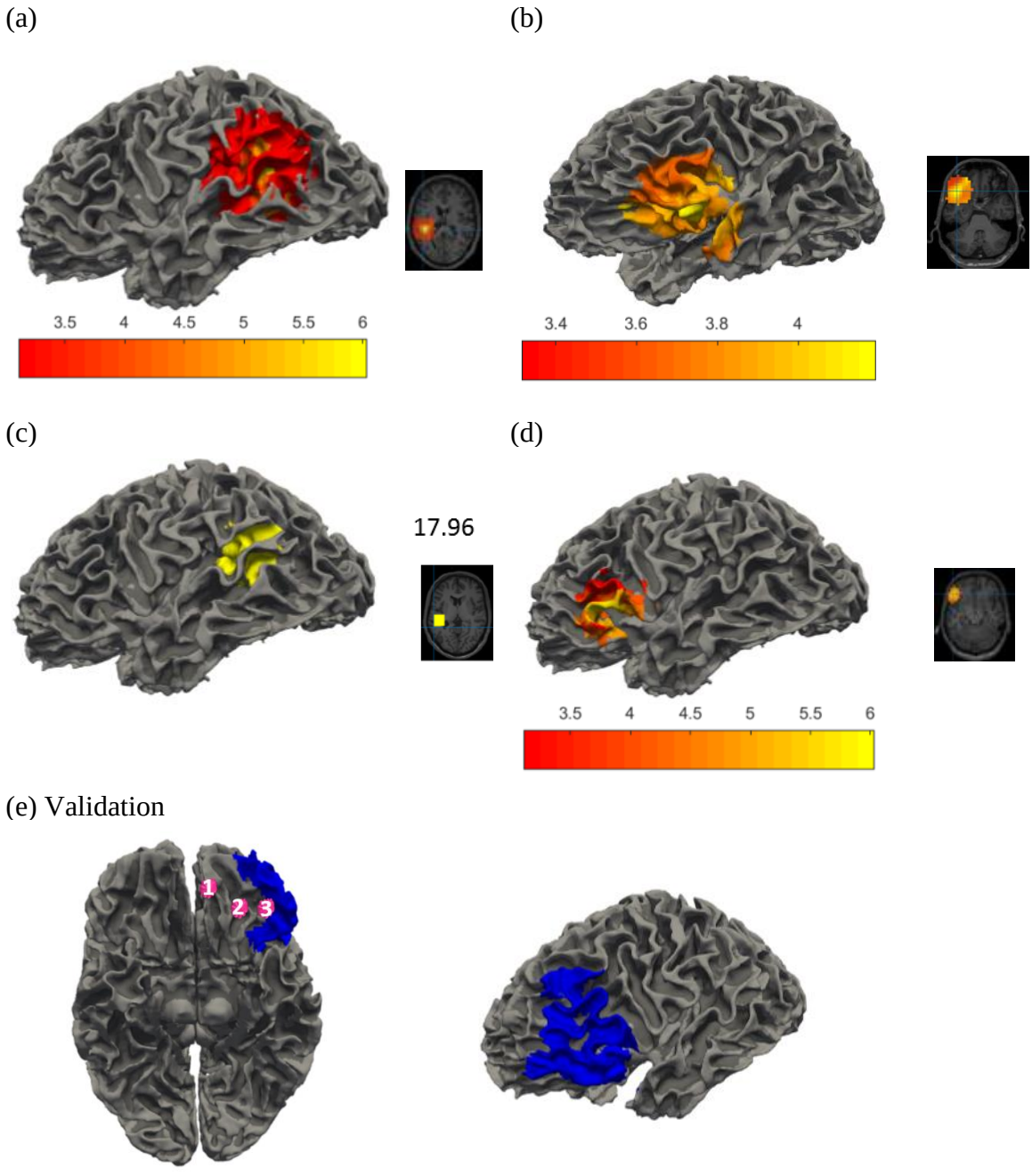

Figure 3-12 Source localisation for Patient P016 using Solution 1, 2, 3, 4 and validations. (a) Solution 1 and (b) Solution 3 co-localized to left posterior inferior temporal, while (b) Solution 2 and (d) Solution 4 localized to left inferior frontal gyrus. The kurtosis value of Solution 3 is 17.96. The subfigures of (a), (b), (c) and (d) show the corresponding sources registered onto the MRI images. In the colour maps shown in (a), (b) and (c), yellow represents the highest kurtosis value and red represents the lowest values. . (e) The validations used in this study, in which surgically resected areas are indicated by the blue surface and pink discs indicate the clinically localized results. In clinical EEG-MEG source localisation, the onset of the source located at rectal gyrus then propagate to medial orbitofrontal gyrus, later to lateral orbitofrontal gyrus. This propagation process is indicated by pink discs with white number 1, 2 and 3.

P035

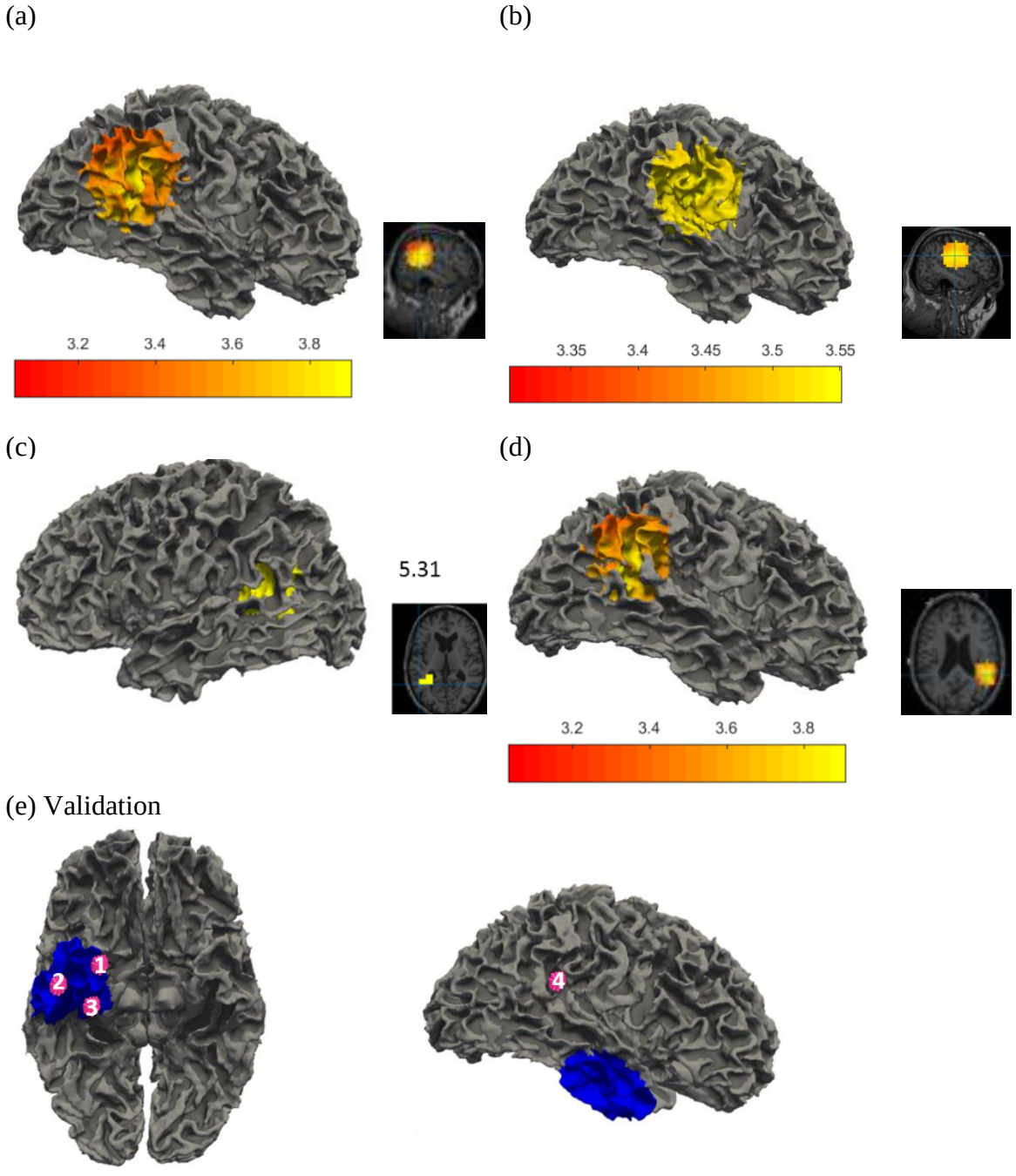

Figure 3-13 Source localisation for Patient P035 using Solution 1, 2, 3, 4 and validations. (a) Solution 1, (b) Solution 2 and (d) Solution 4 were co-localized to parietal convexity, which are concordant with the propagation of the clinical solutions. (c) Solution 3 with kurtosis value 5.31 localized to left posterior inferior temporal lobe, which is irrelevant with all the validations of this patient. The subfigures of (a), (b), (c) and (d) show the corresponding sources registered onto the MRI images. In the colour maps shown in (a), (b) and (c), yellow represents the highest kurtosis value and red represents the lowest values. (e) The validations used in this study, in which surgically resected areas are indicated by the blue surface and pink discs indicate the clinically localized results. In clinical EEG-MEG source localisation, the onset of the source located at antero-basal temporal cortex then propagate to infero-lateral temporal cortex, later to posterior temporal cortex and parietal convexity. This propagation process is indicated by pink discs with white number 1, 2, 3 and 4 in (e).

P037

(a) (b)

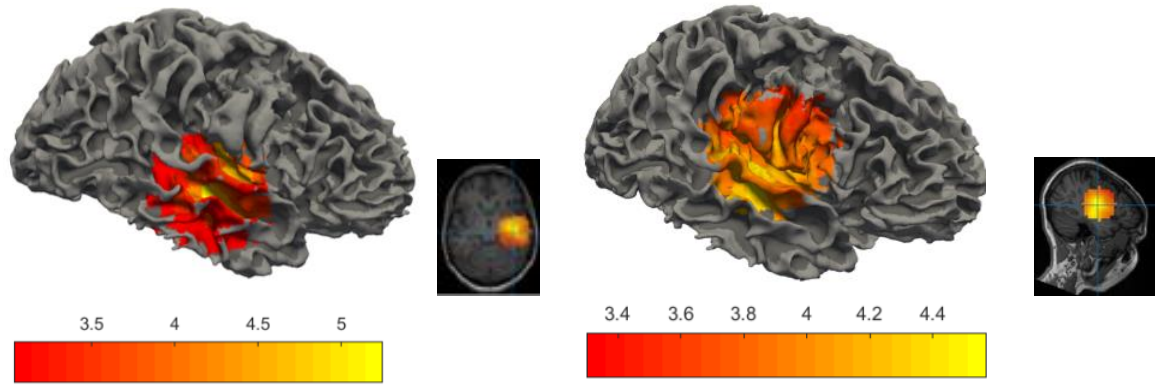

(c) (d)

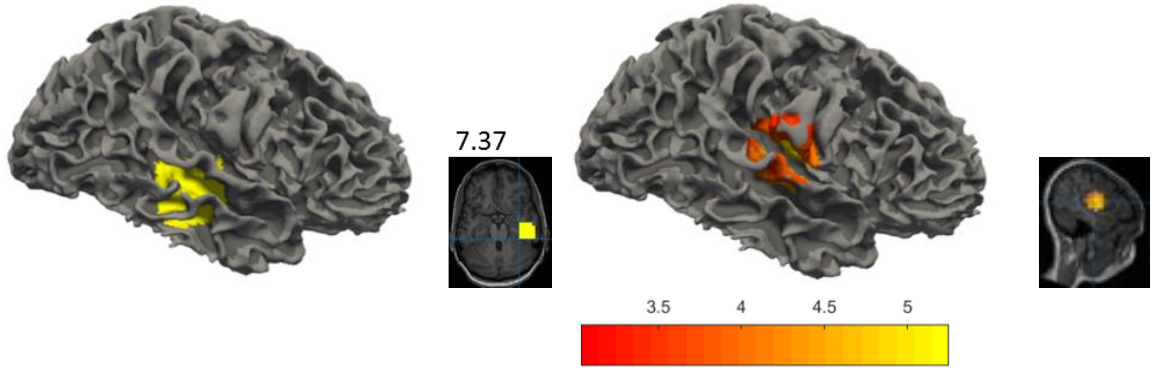

(e) Validation

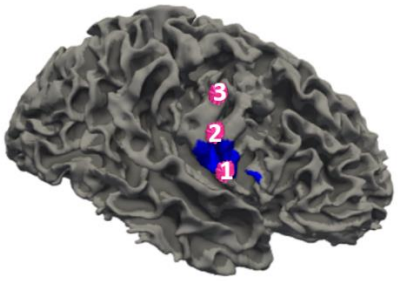

Figure 3-14 Source localisation for Patient P037 using Solution 1, 2, 3, 4 and validations. (a) Solution1 and (c) Solution 3 localized to right middle temporal lobe, while (b) Solution 2 and (d) Solution 4 localized to pre-central gyrus. The kurtosis of the VS for Solution 3 is 7.37 shown above the MRI image in (c). The subfigures of (a), (b), (c) and (d) show the corresponding sources registered onto the MRI images. In the colour maps shown in (a), (b) and (c), yellow represents the highest kurtosis value and red represents the lowest values. (e) The validations used in this study, in which surgically resected areas are indicated by the blue surface and pink discs indicate the clinically localized results. In clinical source localisation, the onset of the source located at base pre-central gyrus approximating face then propagate pre-central gyrus approximating hand, later propagate upward along the line of the pre-central gyrus. This propagation process is indicated by pink discs with white number 1, 2 and 3 in (e).

P040

(a) (b)

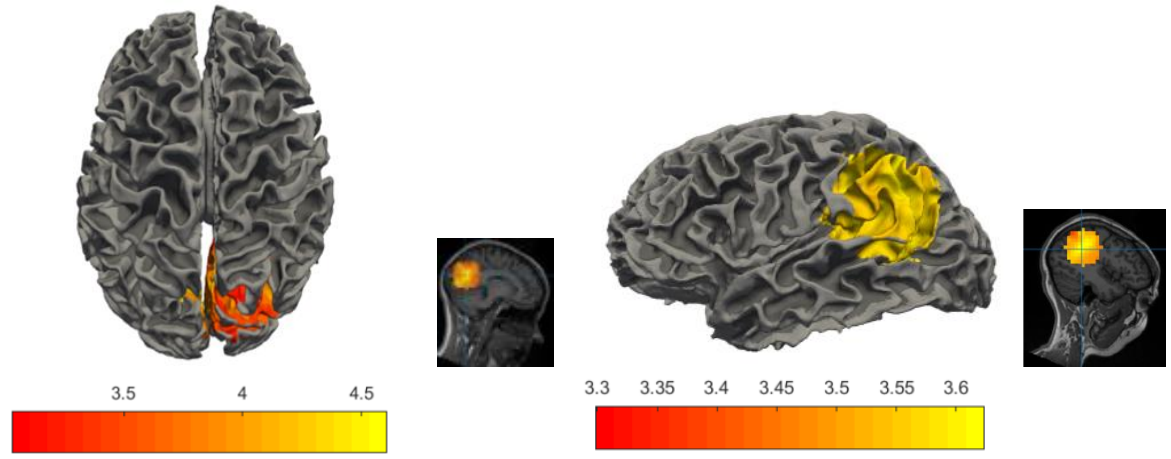

(c) (d)

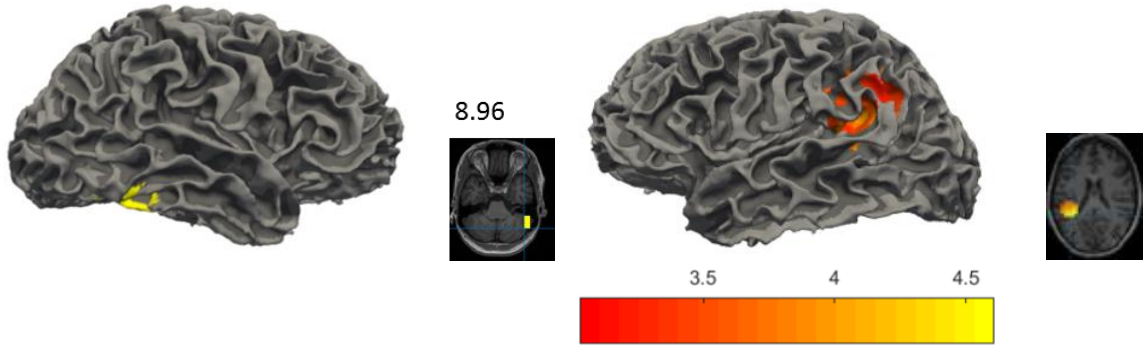

(e) Validation

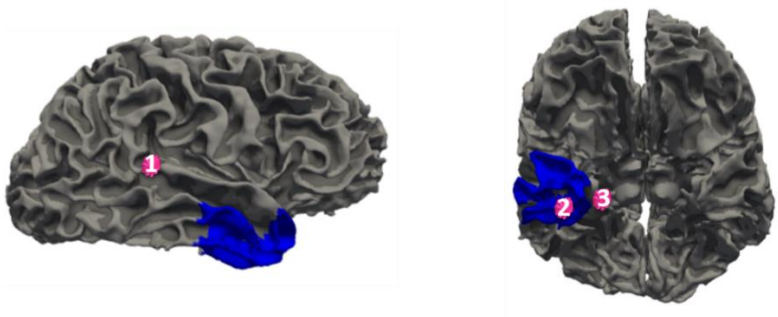

Figure 3-15 Source localisation for Patient P040 using Solution 1, 2, 3, 4 and validations. (a) Solution 1 localized to right occipital lobe. (c) Solution 3 with kurtosis value 8.98 localized to right posterior inferior temporal gyrus. (b) Solution 2 and (d) Solution 4 were co-localized to left parietal convexity. The subfigures of (a), (b), (c) and (d) show the corresponding sources registered onto the MRI images. In the colour maps shown in (a), (b) and (c), yellow represents the highest kurtosis value and red represents the lowest values. (e) The validations used in this study, in which surgically resected areas are indicated by the blue surface and pink discs indicate the clinically localized results. In clinical EMSL, the onset of the source located at posterior superior temporal gyrus, then propagate to lateral mesial temporal gyrus, and later to right uncus. This propagation process is indicated by pink discs with white number 1, 2 and 3 in (e).

P042

(a)

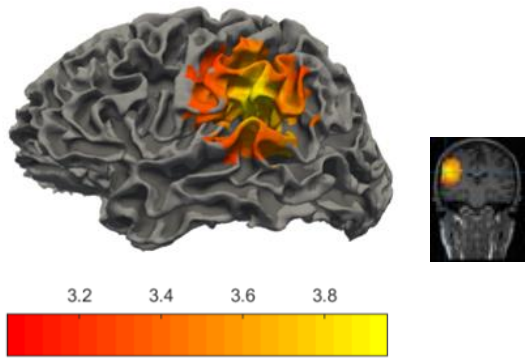

(b)

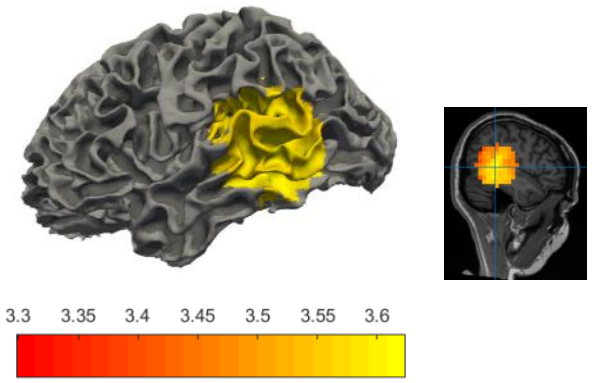

(c)

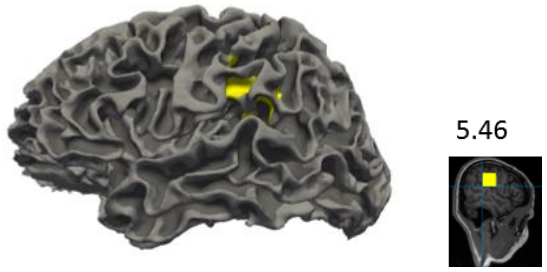

(d)

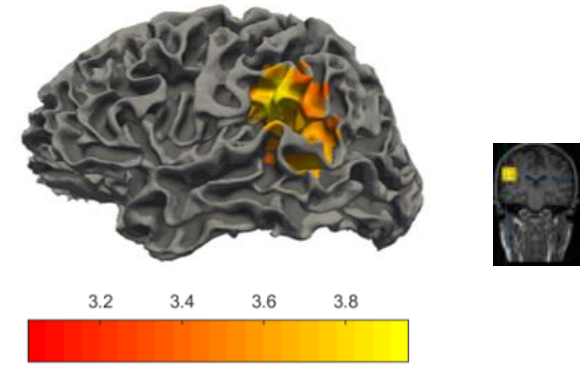

(e) Validation

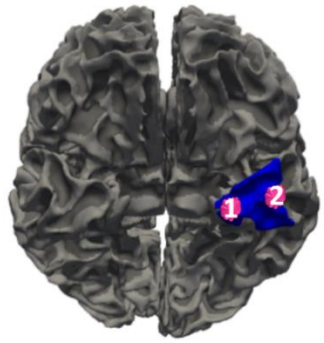

Figure 3-16 Source localisation for Patient P042 using Solution 1, 2, 3, 4 and validations. (a) Solution 1, (b) Solution 2, (c) Solution 3 and (d) Solution 4 were co-localised to left parietal convexity. The kurtosis of Solution 3 is 5.46 shown in (c). The subfigures of (a), (b), (c) and (d) show the corresponding sources registered onto the MRI images. In the colour maps shown in (a), (b) and (c), yellow represents the highest kurtosis value and red represents the lowest values. (e) The validations used in this study, in which surgically resected areas are indicated by the blue surface and pink discs indicate the clinically localized results. In clinical source localisation, the onset of the source located at baso-mesial temporal, then propagate to basolateral temporal cortex. This propagation process is indicated by pink discs with white number 1 and 2 in (e).

P046

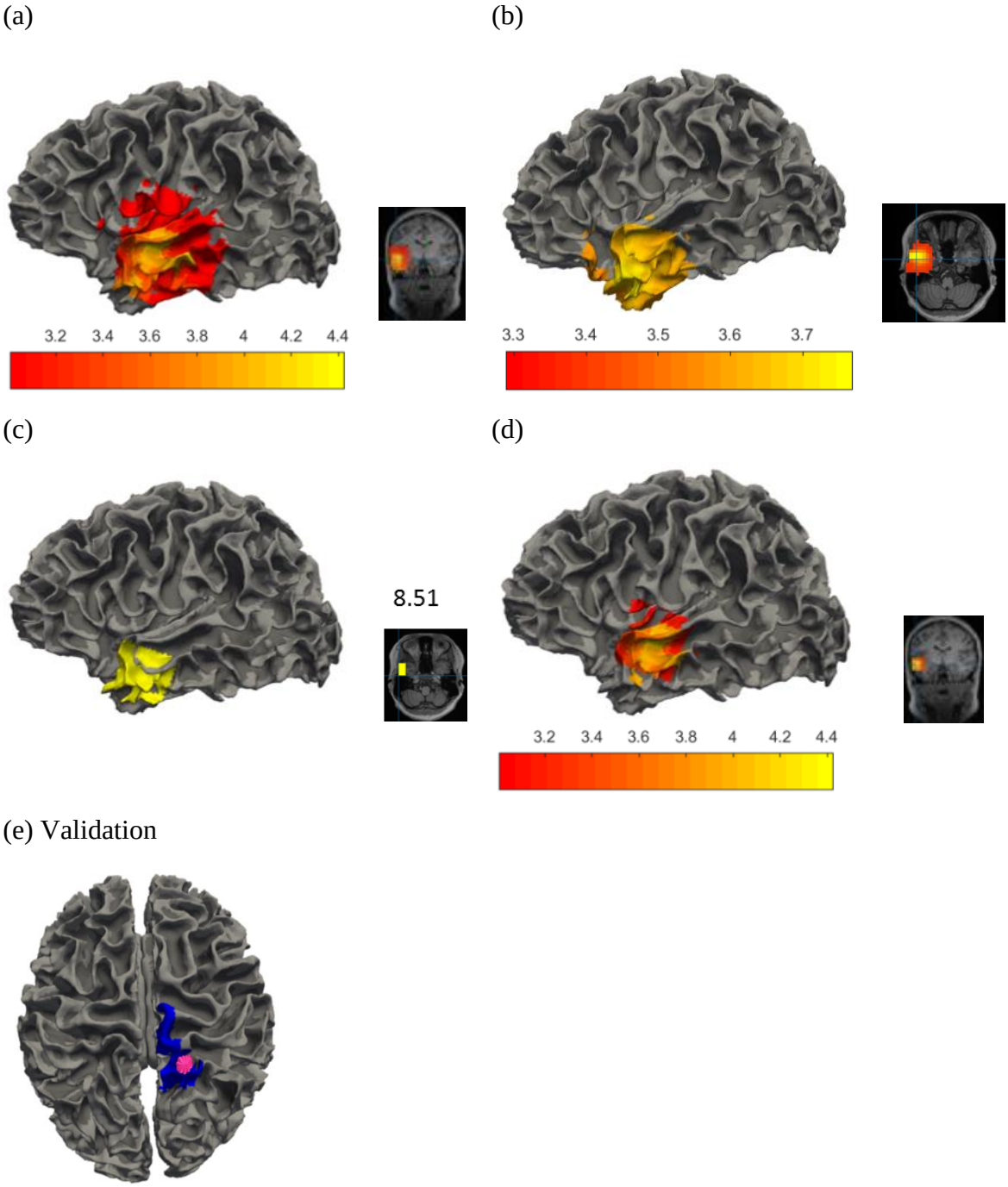

Figure 3-17 Source localisation for Patient P046 using Solution 1, 2, 3, 4 and validations. (a) Solution 1, (b) Solution 2, (c) Solution 3 and (d) Solution 4 were co-localized to left anterior temporal lobe. The kurtosis value of Solution 3 is 8.51 shown above the MRI image in (c). The subfigures of (a), (b), (c) and (d) show the corresponding sources registered onto the MRI images. In the colour maps shown in (a), (b) and (c), yellow represents the highest kurtosis value and red represents the lowest values. (e) The validations used in this study, in which surgically resected areas are indicated by the blue surface and pink discs indicate the clinically localized results. In clinical localisation, the source located at Right posterior paracentral lobule and precuneus demonstrated by the pink disc in (e), and no propagation found.

P049

(a)

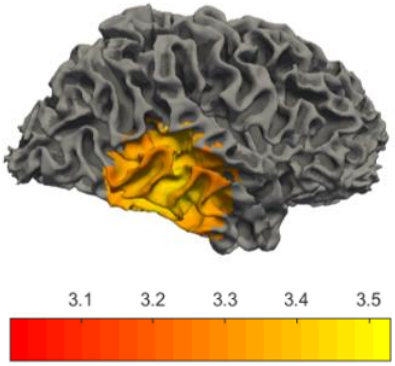

(b)

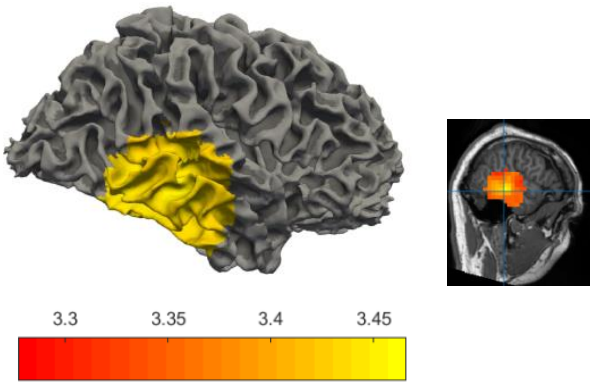

(c)

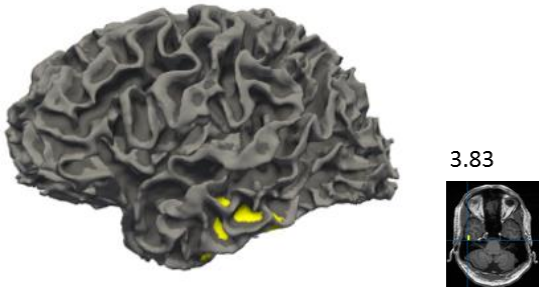

(d)

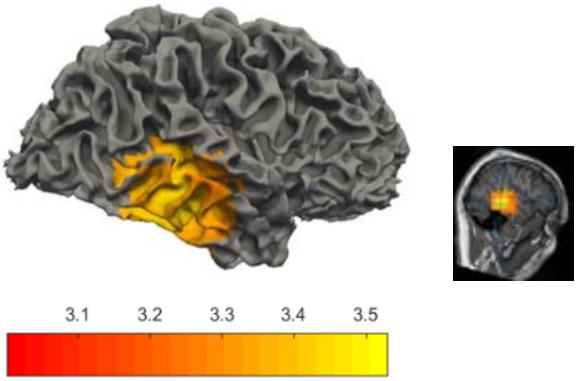

(e) Validation

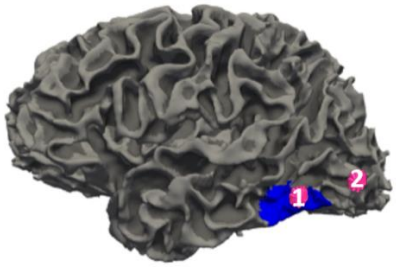

Figure 3-18 Source localisation for Patient P049 using Solution 1, 2, 3, 4 and validations. (a) Solution 1, (b) Solution 2 and (d) Solution 4 localized to right posterior temporal lobe, while (c) Solution 3 localized to left inferior temporal gyrus. The kurtosis value of the VS for Solution 3 is 3.83 shown above the MRI image in (c). The subfigures of (a), (b), (c) and (d) show the corresponding sources registered onto the MRI images. In the colour maps shown in (a), (b) and (c), yellow represents the highest kurtosis value and red represents the lowest values. (e) The validations used in this study, in which surgically resected areas are indicated by the blue surface and pink discs indicate the clinically localized results. In clinical EMSL, the onset of source located at left TPO junction demonstrated by a pink disc with number 1 in (e), then propagate to pre-occipital notch and PON indicated by a pink disc with number 2 in (e).

P061

(a)

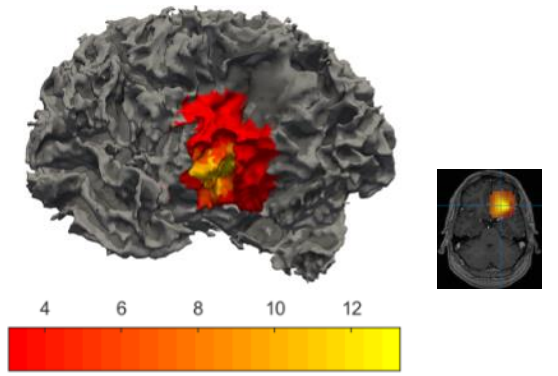

(b)

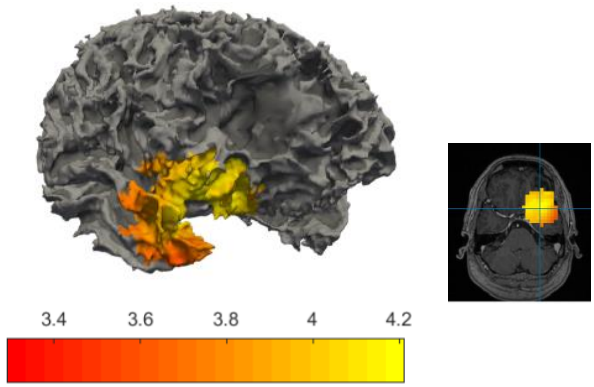

(c)

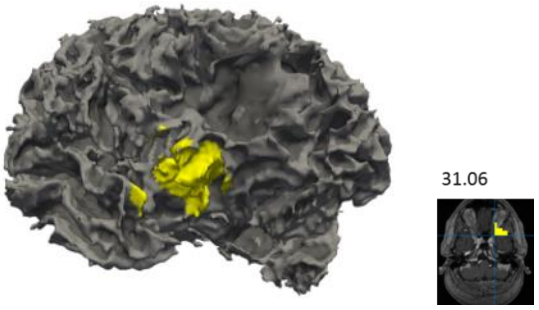

(d)

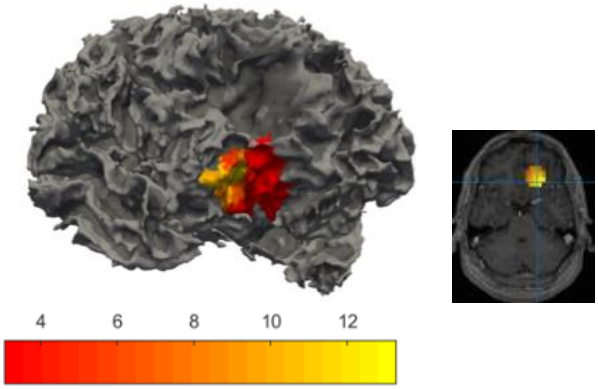

(e) Validation

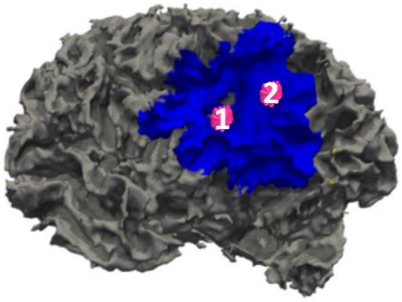

Figure 3-19 Source localisation for Patient P061 using Solution 1, 2, 3, 4 and validations. All of the solutions 1, 2, 3 and 4 were localized to the right-medial frontal gyrus, which are shown in (a), (b), (c) and (d), respectively. (c) Solution 3 with kurtosis value 31.06 shown above the MRI image. The subfigures of (a), (b), (c) and (d) show the corresponding sources registered onto the MRI images. In the colour maps shown in (a), (b) and (c), yellow represents the highest kurtosis value and red represents the lowest values. (e) The validations used in this study, in which surgically resected areas are indicated by the blue surface and pink discs indicate the clinically localized results. In clinical EEG-MEG source localisation, the onset of source located at right inferior frontal gyrus, then propagate to infero-medial frontal gyrus. The clinical spike onset and propagation are illustrated by the pink discs with number 1 and 2 in (e), respectively.

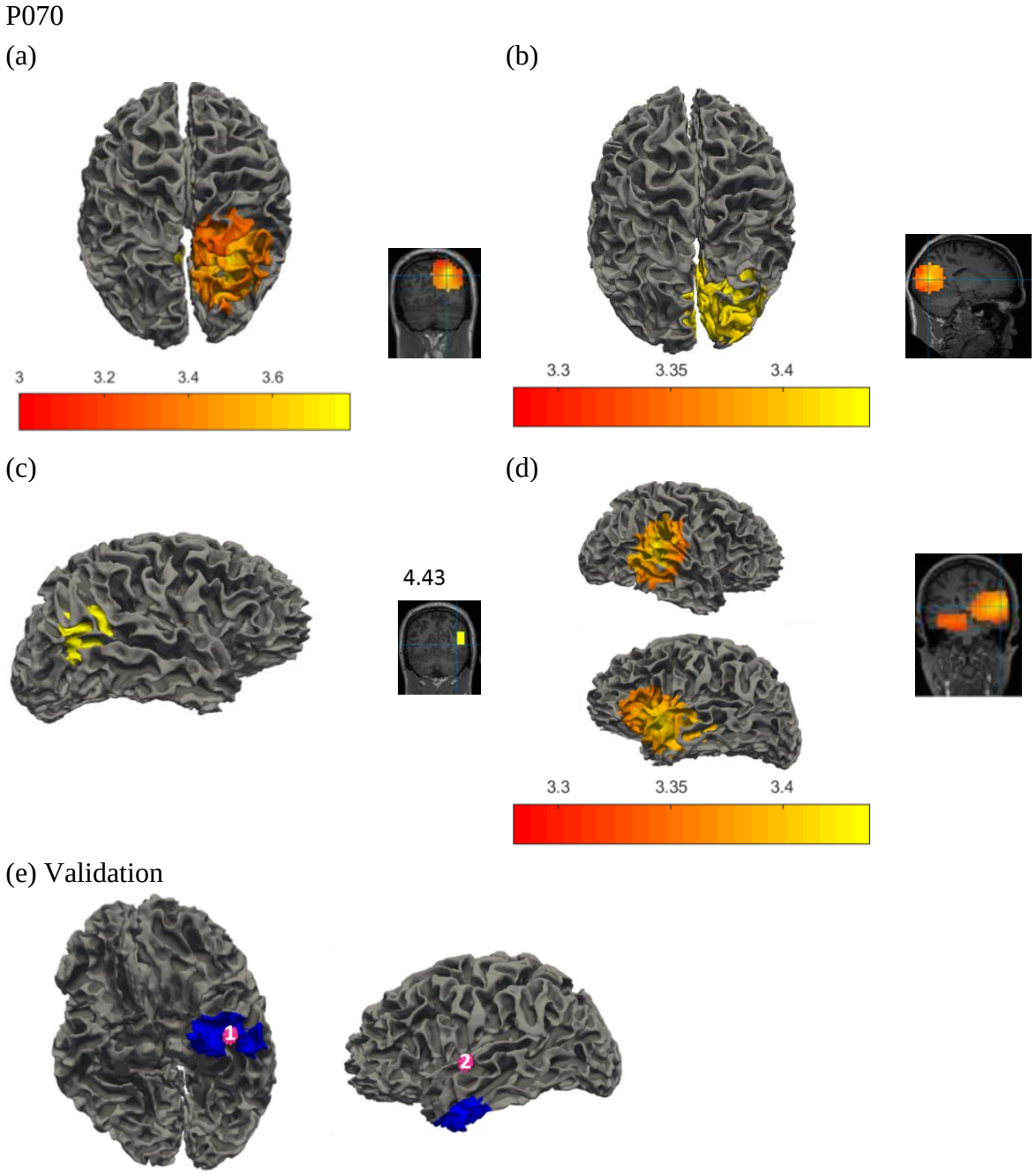

Figure 3-20 Source localisation for Patient P070 using Solution 1, 2, 3, 4 and validations. (a) Solution 1 localized to right superior parietal lobule. (b) Solution 2 was localized to right occipital lobe. (c) Solution 3 localized to right inferior parietal lobule and the g2 of the VS for Solution 3 is 4.43 shown above the MRI in (c). The localized regions of Solution 4 shown in (d) spread out to right posterior temporal lobe, right postcentral gyrus, left anterior temporal lobule and left inferior frontal gyrus. The subfigures of (a), (b), (c) and (d) show the corresponding sources registered onto the MRI images. In the colour maps shown in (a), (b) and (c), yellow represents the highest kurtosis value and red represents the lowest values. (e) The validations used in this study, in which surgically resected areas are indicated by the blue surface and pink discs indicate the clinically localized results. In clinical localisation, the onset of source located at anterior inferior temporal gyrus indicated by the pink disc with number 1 in (e), then propagate to posterior superior temporal gyrus demonstrated by the pink disc with number 2 in (e).

P072

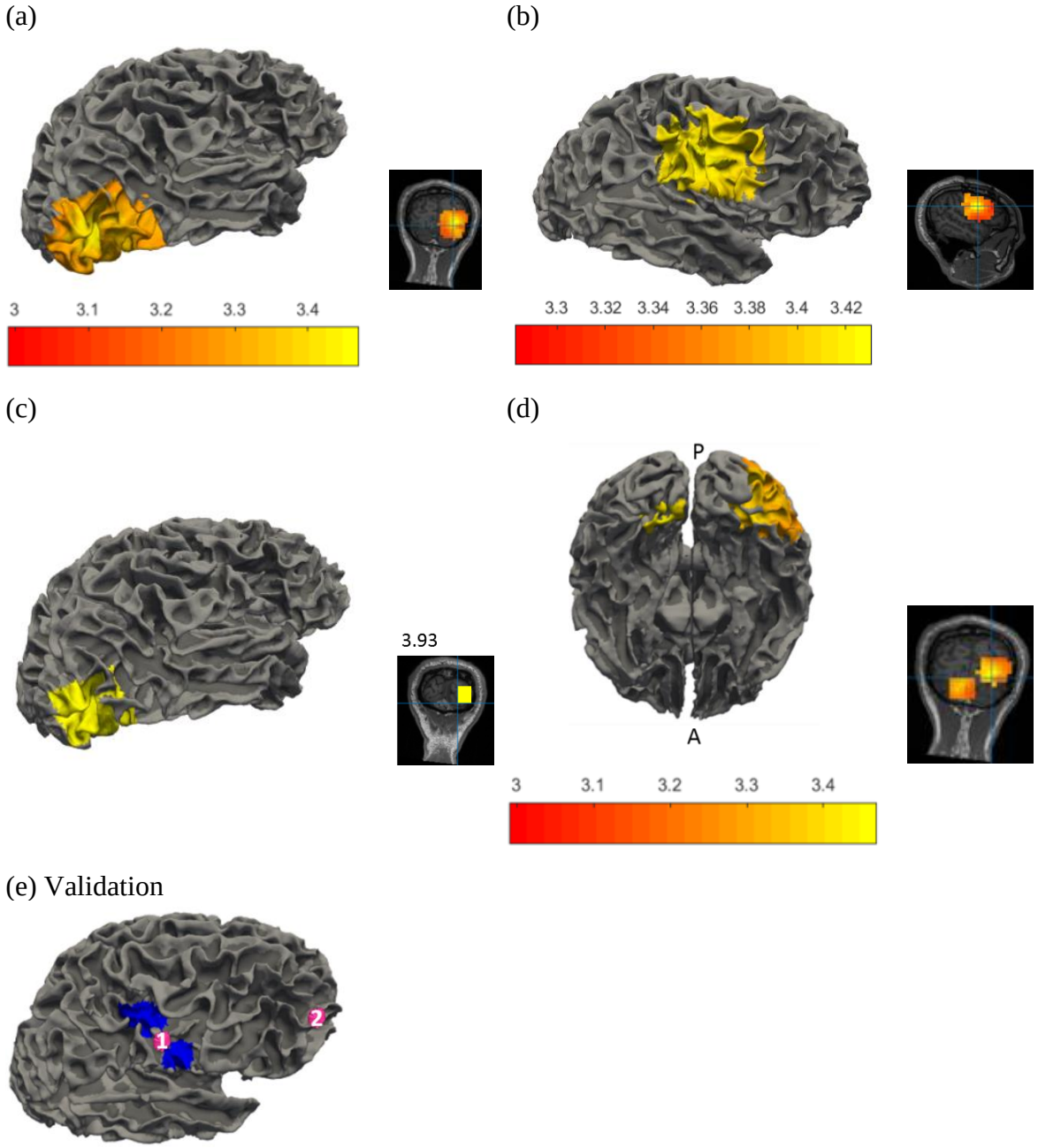

Figure 3-21 Source localisation for Patient P072 using Solution 1, 2, 3, 4 and validations. (a) Solution 1 and (c) Solution 3 with kurtosis value 3.93 localized to right occipital lobe. (b) Solution 2 was localized to the right premotor cortex, which is concordant with the surgical resection and the onset of the clinical localisation. (d) Solution 4 was localized to right occipital lobe, while it also localized to the left occipital lobe. In the figure of Solution 4, A represents anterior and P represents posterior. The subfigures of (a), (b), (c) and (d) show the corresponding sources registered onto the MRI images. In the colour maps shown in (a), (b) and (c), yellow represents the highest kurtosis value and red represents the lowest values. (e) The validations used in this study, in which surgically resected areas are indicated by the blue surface and pink discs indicate the clinically localized results. In clinical localisation, the onset of source located at right premotor cortex, then propagate to frontal pole. The clinical onset and propagation are shown by the pink discs with number 1 and 2, respectively, in (e).

P074

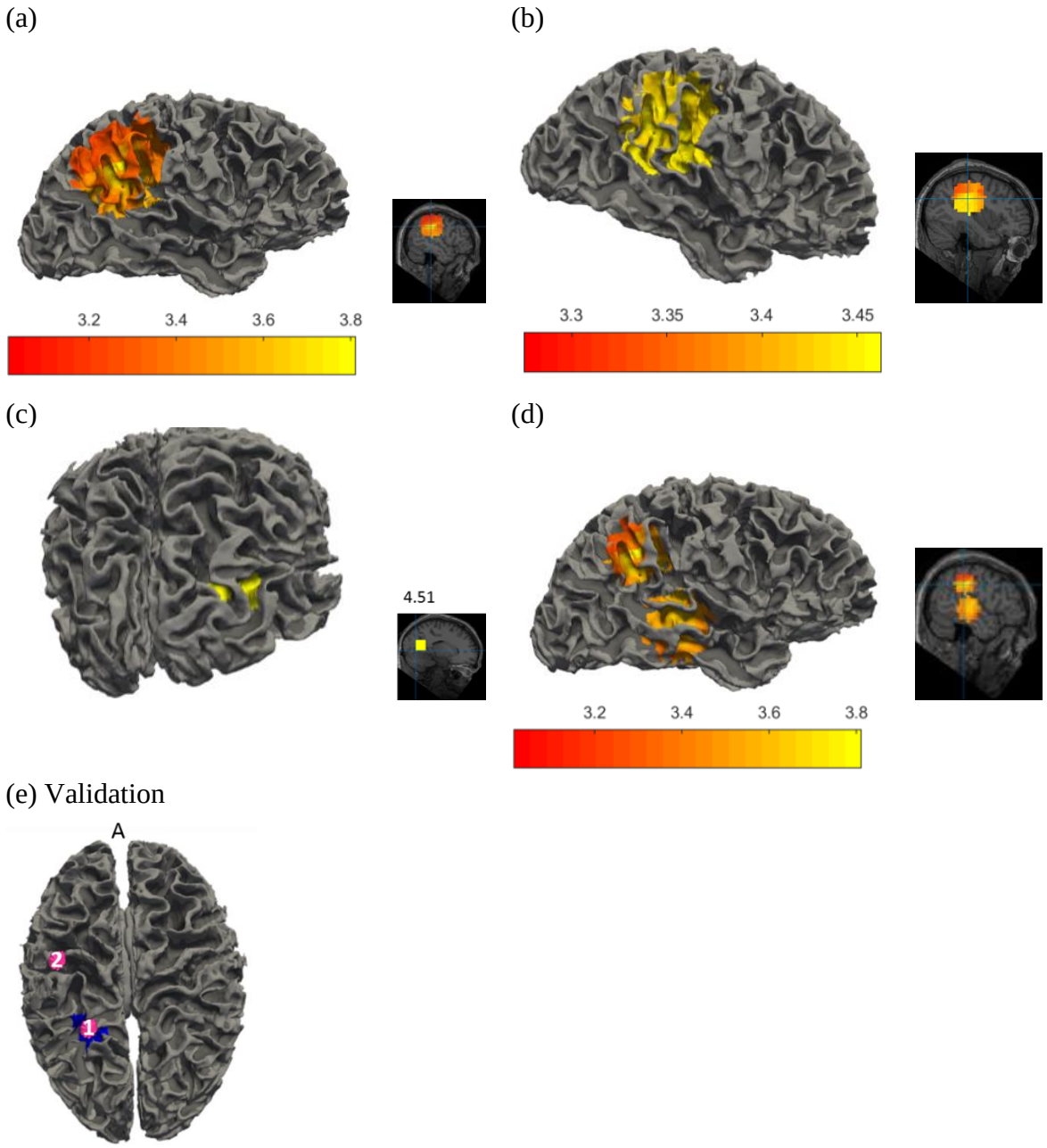

Figure 3-22 Source localisation for Patient P074 using Solution 1, 2, 3, 4 and validations. (a) Solution 1 and (b) Solution 2 were localized to right parietal convexity. (c) Solution 3 with kurtosis value 4.51 localized to right middle occipital gyrus. (d) Solution 4 localized to an extended area including posterior right temporal lobe and right parietal convexity. The subfigures of (a), (b), (c) and (d) show the corresponding sources registered onto the MRI images. In the colour maps shown in (a), (b) and (c), yellow represents the highest kurtosis value and red represents the lowest values. (e) The validations used in this study, in which surgically resected areas are indicated by the blue surface and pink discs indicate the clinically localized results. In clinical EEG-MEG source localisation, the onset of source located at junction of the post-central sulcus and superior parietal lobule, then propagate to Ipsilateral pre-central gyrus. The onset and propagation are shown by the pink discs with number 1 and 2, respectively, in (e). The anterior of the brain is indicated by the 'A' in (e).

3.4 Discussion

In this work, we applied beamforming to reconstruct brain source activities and obtained virtual sensors (VSs) on which kurtosis was used to detect outliers in order to localise spike discharges. We examined the localised regions extracted from the kurtosis distribution and VSs with four solutions and tested the four solutions with validations including clinical EEG and MEG source localisation and surgical resections.

Among the four solutions, Solutions 1 and 2 applied the selection strategy that considered the regions with maximal kurtosis as the source candidates, but with sliding window lengths 3 min and 1 sec, respectively. We can see from the validations that Solution 2 outperformed Solution 1 in terms of both clinical source localisation and surgical resections. This benefit was obtained because of the bias correction introduced by using sliding windows with more appropriate length. The value of kurtosis can be affected by the frequency of the spikes; infrequent spikes lead to high kurtosis and can be diminished by frequent spikes. Harpaz et al. (2015) proposed the use of a sliding window with length that contains only one spike to obtain the optimal kurtosis distribution and showed the kurtosis index revealed lesions by using sliding windows in two epilepsy patients. Scott et al. (2016) also recommended the use of a 1 second sliding window to localise interictal spikes on VSs. Our study validated that the sliding window was better in localizing spikes than the long segment. However, the performance of the sliding window Solution 2 was limited as it localized to the surgical resection in only four out of nine seizure-free patients. Scott et al. (2016) tested their algorithm with only seven patients. Therefore, future work is needed where the length of the sliding window is adjusted in a patient-specific manner, possibly depending on the spike rate for each patient.

Besides the various spike rates, another factor that reduced the performance of Solution 2 might have been the spread propagations of the interictal spikes. Solution 2 localized to clinical propagations in four patients (P012, P016, P035, P061), of which Solution 2 localized to the surgical cavities of two patients (P016 and P061) and failed to localize the surgical resection of the other two patients (P012 and P035). It can be seen from the clinical results that the interictal spike propagations in patients P012 and P035 were more spread, and the clinical propagations in patients P016 and P061 were more local.

Solution 4 localised to regions with persistent spikes, which localised to surgical resections in only three out of nine seizure free patients. This method localised to the clinical propagations in three patients (P016, P035, P061) and localised to the clinical onset in just one patient (P035).

The localised spike propagation in this work corresponded to the peak of the averaged interictal spikes, which have higher signal-to-noise ratio (SNR) (Plummer et al., 2019). From the validation results of Solution 2 and Solution 4, we may conclude that kurtosis beamforming might be more robust to spike propagation or these methods are robust with high SNR sources. Future work would be to study of directed connectivity or propagations of interictal spikes across reconstructed VSs, which may help us to distinguish different states of spike propagations (Conrad et al., 2019; Tomlinson et al., 2016; Tomlinson et al., 2017; Tomlinson et al., 2019a).

Solution 3 had the worst performance among the four solutions. It utilised the VS with maximal kurtosis as the localised result. This finding is contrary to the report by Hall et al. (2018). Their study implemented kurtosis beamforming on 22 epilepsy patients and they chose the single VS with spikes present as the localised region. They reported that the chosen VS co-localised to the surgical cavities in 9 out of 13 seizure-free patients and in 3 out of 5 seizure-persistent patients. However, this selection strategy in our work obtained concordant localisation results with surgical resection in only one patient (P061). While this method localised to one of the clinical localised regions for P007, this was because this patient had rare and high amplitude spikes. Thus, this method might be sensitive to patients with low frequency and high amplitude spikes.

3.5 Conclusion

We applied kurtosis beamforming to MEG recordings to localise epileptic sources with four strategies. The localised results of four strategies were validated against clinical source localisations and surgical resections. We do not recommend the solution using the VS with the maximal kurtosis. The solution that adopted the region with persistent interictal spikes localised to spike propagation better than spike onset and so is not a good biomarker for epileptogenic zone localisation. Two solutions applied sliding windows with different lengths; of these, the one second sliding window delivered better performance. It is possible that patient-specific sliding window lengths may have the potential to improve the localisation performance of kurtosis beamforming.

Chapter 4 Automatic detection of interictal spikes in MEG source space

4.1 Introduction

Kurtosis beamforming has been used in presurgical evaluation to localize the epileptogenic zone (EZ) for patients with drug resistant focal epilepsy. The local maxima of the kurtosis map generated by the beamforming are defined as virtual sensors (VSs). The manual inspection of VS time series reconstructed using beamforming has been commonly used to confirm whether VSs are present with genuine interictal spikes rather than artefacts (Agirre-Arrizubieta et al., 2014; de Gooijer‐van de Groep et al., 2013; Hall et al., 2018; Kirsch et al., 2006; Oishi et al., 2006; Rose et al., 2013; Tenney et al., 2014). However, automatic spike detection on VSs has not been developed to help identify spike-related VSs reconstructed by beamforming.

Studies on automatic spike detection of spikes on MEG sensors have been developed in a few studies. Khalid et al. (2016) extracted features for spike and non-spike groups using common spatial pattern that can maximise the data variance of one group and output the unit variance of the other group. The linear discriminant analysis was applied as the classifier. Later, they developed another automatic MEG spike detection method that detected abnormal discharges with amplitude over a threshold, then warping path lengths calculated by the dynamic time warping method were used to quantify the similarity across discharges on various channels (Khalid et al., 2017). Discharges on two electrodes were defined to be similar if the warping path length was smaller than a similarity threshold. If the number of electrodes with similar discharges was over a distribution threshold, these discharges were detected as a threshold.

It has been shown that epileptic spikes recorded by MEG and EEG can be visually identified using similar empirical knowledge (Iwasaki et al., 2005; Zijlmans et al., 2002). However, Fernandes et al. showed that EEG and MEG spikes are significantly different in terms of morphological parameters including duration, sharpness and shape (Fernandes et al., 2005), which suggests that EEG spike automatic detection methods are not applicable to MEG spike detection. Nowak et al. provided the quantitative range of morphological parameters for MEG spikes (Nowak et al., 2009). However, their study only included four refractory epilepsy patients, which might not be sufficient for detecting spikes across a broader population of patients.

The key component of automatic detection of interictal spikes is feature extraction from the abnormal discharges and background data. Feature extraction can be performed in the time domain and the frequency domain. In the time domain, the commonly extracted features include mimetic parameters that describe the morphology of the abnormal discharges. In particular, the autoregressive method assumes the recording is stationary and detects the non-stationary component present in the data (Exarchos et al., 2006; Gotman et al., 1979; İnan & Kuntalp, 2007b; Liu et al., 2002; Senhadji et al., 1995; Tzallas et al., 2006). Frequency domain features such as the power spectrum in each sub-band have been implemented using the Fourier transform, wavelet transform, Walsh transform and Hilbert transform (Adjouadi, Cabrerizo, et al., 2004; Exarchos et al., 2006; Feucht et al., 1997; Richard et al., 2015; Yuan et al., 2012). An alternative approach to feature-based detection methods is template matching, which detect transients in the data that are highly correlated with a template (Sankar & Natour, 1992; Stevens et al., 1972). It was not clear that which method performs the best among the automatic detection methods (Halford, 2009; Wilson & Emerson, 2002). In our study, we combined aspects of frequency spectrum analysis, statistical parameters and mimetic parameters for spike detection.

An interictal spike is characterised as a sharp, high-amplitude event mostly followed by a slow wave. Intracranial studies in focal epilepsy patients have demonstrated that the sharp part of the spike discharge is initiated by large postsynaptic depolarisation (Babb et al., 1987; Isokawa-Akesson et al., 1989; Kooi, 1966; Wyler et al., 1982). The amplitude reduction of background activity and high frequency oscillations after the sharp wave discharge indicates fast repolarization (Urrestarazu et al., 2006). Previous mimetic methods for spike detection only considered the morphological description of the sharp wave and ignored the quantification of the slow wave/repolarization that usually follows the sharp component (Adjouadi, Sanchez, et al., 2004; Dingle et al., 1993; Exarchos et al., 2006; Gotman & Gloor, 1976; İnan & Kuntalp, 2007a; Tzallas et al., 2006; Webber et al., 1994). In our study, we also included mimetic parameters describing the slow wave that follows the sharp peak.

The approach of this work was as follows. First, we detected abnormal discharges on the VSs reconstructed from MEG sensor data using beamforming. Second, clustering on the VS locations and discharge morphologies was performed to generate representative discharges from the many transients detected on the VSs; expert annotations were performed on the clusters. Third, features used for interictal spike detection were extracted from the frequency spectrum and statistical parameters of the background data around the detected abnormal

discharges, and the abnormal transient including the sharp events and the following slow wave were described by mimetic parameters. Fourth, a classifier was applied to the annotated events using leave-one-patient-out. Finally, classification performance was validated against expert labelling.

4.2 Methods

4.2.1 Data

Epilepsy patients, MEG data recordings and pre-processing steps used in this chapter are described in Section 2.1 , 2.2 and 2.3 , respectively. Virtual sensors (VSs) are local maxima of g2-distributions generated by beamforming from MEG recordings, which is described in Section 3.2.1 . Interictal spike detection in this chapter was performed on all the VSs selected by a threshold defined by the elbow method (described in Section 0).

4.2.1.1 Detection of abnormal discharges

We detected all the abnormal discharges with high magnitudes on the z-scored VS time series. Here, we denote the VS time series as $s_{\mathrm{vs}}(t)$. We detected all the peaks of $s_{\mathrm{vs}}(t)$ with absolute amplitudes exceeding a threshold defined by $\mathrm{mean}[s_{\mathrm{vs}}(t)] + n \cdot \mathrm{std}[s_{\mathrm{vs}}(t)]$, where $\mathrm{mean}[\cdot]$ is the expectation and $\mathrm{std}[\cdot]$ is the standard deviation. n was set to be 5 initially. If there were no peaks with amplitudes over the threshold, we decreased n by 0.2. The decrease of n by value 0.2 was repeated until at least one peak above the threshold was detected on a VS.

Then, we extracted 200 ms data around detected peaks as abnormal discharges to be classified as spikes or non-spikes using the following procedures. If the temporal distance between peaks was smaller than 200ms, we merged these events into one event. Also, we extracted 1s and 3s of data centred around the absolute maximum of the detected abnormal discharges as the baseline.

An example of event detection on a VS is shown in Figure 4-1. The abnormal discharge is indicated by the dotted line and the 1s and 3s background data are demonstrated by the solid lines with arrows. In this chapter, we use $s(n)$, $b_1(n)$ and $b_3(n)$ to denote the detected abnormal discharge, the 1 s background data and the 3 s background data, respectively.

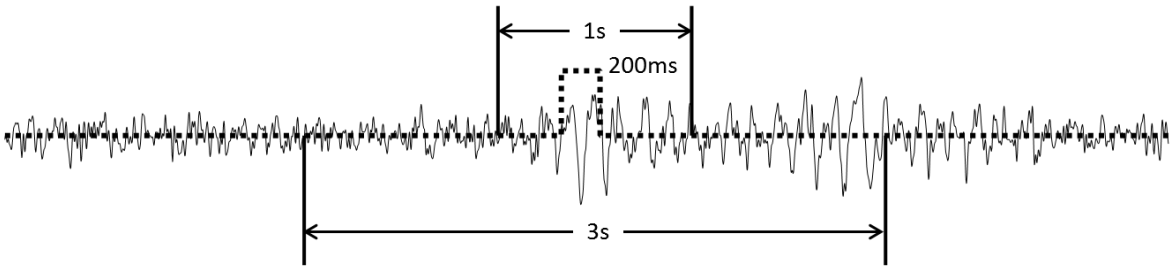

Figure 4-1 Event detection. The solid line in this figure represents the time series of a VS. An abnormal discharge detected by the amplitude threshold is indicated by the dotted line. The 1 s and 3 s of background data centred on the absolute maximum of the abnormal discharge are indicated in this figure, which are considered as the background of the abnormal discharge.

4.2.1.2 Representative abnormal discharges

Since the number of detected abnormal discharges is very large, we obtained the most representative detected discharges for each patient on which the labelling by clinicians was performed. We clustered all the detected discharges by their locations in the brain first, then discharges in each spatial cluster were further clustered by their morphologies. The distance measure used for both clustering procedures was the Euclidean distance and the cluster method used was the hierarchical method with "average" linkage, which determines the distance between clusters with the averaged distance between all pairs of objects in any two clusters (Maharaj, 2000). The linkage is defined as the distance between two clusters, and the average linkage between cluster r and s can be expressed as

$$d_{\text{avg}}(r,s) = \frac{1}{n_r n_s}\sum_{i=1}^{n_r}\sum_{j=1}^{n_s}\left\|e_{ri} - e_{sj}\right\| \tag{4.1}$$

where n_r and n_s are the numbers of events in clusters r and s, respectively, and e_{ri} and e_{sj} represent the locations of the ith event and the jth event in cluster r and s, respectively. $\|\cdot\|$ is the L^2 norm (Euclidean distance). Events to be clustered for the spatial clustering were the locations of VSs. For the morphological clustering, events to be clustered were the 1 s time series. The resulting hierarchical dendrogram was cut at the height of 3 cm for the spatial clusters, which indicates that the averaged distances between all pairs of VSs in any two clusters was more than 3 cm.

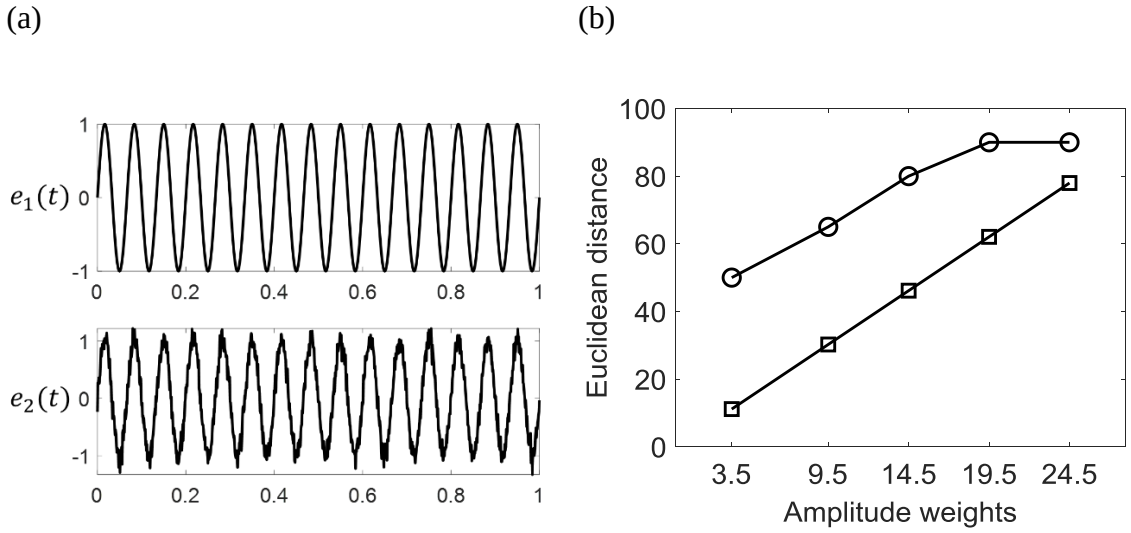

Figure 4-2 The effect of the amplitude on the Euclidean distance between two waveforms. (a) The waveforms of $e_1(t)$ and $e_2(t)$. (b) The line with the square markers shows the distance of $e_1(t)$ and $e_2(t)$ modulated by the weights vector $\boldsymbol{w}$. The x-axis is the weight vector $\boldsymbol{w}$ and y-axis is the corresponding distances of $e_1(t)$ and $e_2(t)$ multiplied by the weight. The line with circle markers in (b) shows the upper limit we set for the within-cluster distance in various amplitude ranges.

Furthermore, we performed morphological clustering on discharges detected on VSs in each spatial cluster obtained in the previous step. First, we classified events by their absolute maximum value into five ranges: $\boldsymbol{r}_1 = [0 \quad 7]$, $\boldsymbol{r}_2 = [7 \quad 12]$, $\boldsymbol{r}_3 = [12 \quad 17]$, $\boldsymbol{r}_4 = [17 \quad 22]$ and $\boldsymbol{r}_5 = [22 \quad 27]$. The reason we performed waveform clustering separately for different amplitude ranges was that the Euclidean distance is biased by the amplitudes of waveforms. We can illustrate the effect of the distance introduced by the amplitude by an example. Say, one waveform is a sinusoidal signal with frequency 15 Hz: $e_1(t) = \sin(2\pi f \cdot t)$, $f = 15\text{Hz}$; the length of data sampled is 1 s with sampling frequency 1000 Hz, $t = 0, 1/f_s, \cdots, 1$. A second waveform is $e_1(t)$ plus the normally distributed noise $n(t)$: $e_2(t) = e_1(t) + 0.1 \cdot n(t)$, where $n(t) \sim N(0,1)$. The waveforms $e_1(t)$ and $e_2(t)$ are shown in Figure 4-2(a). We assign the amplitude weights to both waveforms $e_1(t)$ and $e_2(t)$. The weights vector is $\boldsymbol{w} = [\bar{\boldsymbol{r}}_1, \bar{\boldsymbol{r}}_2, \bar{\boldsymbol{r}}_3, \bar{\boldsymbol{r}}_4, \bar{\boldsymbol{r}}_5] = [3.5, 9.5, 14.5, 19.5, 24.5]$, where $\bar{\boldsymbol{r}}_i = mean\{\boldsymbol{r}_i\}$, $i = 1, \cdots 5$. The Euclidean distance of waveform $w_i \cdot e_1(t)$ and $w_i \cdot e_2(t)$ is modulated by the value of weight w_i, where w_i is an element of the weights vector $\boldsymbol{w}$. The change of $d_E(w_i \cdot e_1(t), w_i \cdot e_2(t))$ introduced by the weight value is shown by the line with square markers in Figure 4-2(b). It can be seen that the distance between two waveforms increases monotonically with the increase of the weight. We can conjecture that if we cut the hierarchical

dendrogram with a specific threshold, the cluster method tends to under-separate discharges with lower amplitude and over-separate discharges with higher amplitude.

In each amplitude range, we clustered detected discharges using the hierarchical method with average linkage, which is expressed in Eq. (4.1). We cut the hierarchical dendrogram by setting the number of clusters. Initially, the number of clusters k assigned was all the integers between 2 and $n_{\text{cluster}}^{\max}$, where $n_{\text{cluster}}^{\max}$ was the maximal cluster number assigned defined as $\min\{0.2n_{\text{eve}}, 40\}$, where n_{eve} is the number of events to be clustered. The optimal cluster number was obtained by the Calinski-Harabasz (CH) criterion (Caliński & Harabasz, 1974). The CH index can be express as

$$Var_{\text{CH}} = \frac{Var_B}{Var_w} \times \frac{N-k}{k-1}, \tag{4.2}$$

where N is the number of observations and k is the number of clusters. Var_B is the overall between-cluster variance, which can be expressed as

$$Var_{\text{B}} = \sum_{i=1}^{k} n_i \|e_i - e_a\|^2, \tag{4.3}$$

where n_i is the number of observations in cluster i, e_i is the centroid of cluster i, e_a is the mean of all the observations and $\|\cdot\|$ is the Euclidean distance. Var_{B} measures the sum of the Euclidean distances of the cluster centroid to the average of observations weighted by the number of observations in each cluster. Var_w is the overall within-cluster variance and is defined as

$$Var_{\text{w}} = \sum_{i=1}^{k} \sum_{e \in c_i} \|e - e_i\|^2, \tag{4.4}$$

where e is an observation and c_i is the ith cluster. Var_{w} measures the sum of the distance of observations in one cluster to its centroid across all the clusters. The optimal cluster number is the one with the highest CH index.

Additionally, we imposed an upper limit of the within-cluster distance to ensure consistency of the inner cluster events. The within-cluster distance of cluster r can be expressed by $d_{\text{avg}}(r, r)$. The within-cluster distance limits set for five amplitude ranges [0, 7], [7, 12], [12, 17], [17, 22] and [22, 27] were 50, 65, 80, 90 and 90, respectively. The reason to set different

limits for the within-cluster distances was that the distance between two events is affected by their amplitudes as shown in Figure 4-2(b), in which the upper limit for the within-cluster distances we set for all of the amplitude ranges is shown by the line with the circle markers.

The representative discharges were the centroid waveforms of each cluster. Neurophysiologists (US and WD) and one experienced researcher (RL, the author) labelled the representative discharges as "spike" or "non-spike" for each patient. To aid the labelling, we also included the sensor data of twenty magnetometers. First, we calculated the Euclidean distance between the discharge to be labelled and their corresponding sensor waveforms. The one with the minimum Euclidean distance and its neighbouring nineteen sensors were included to supply sensor information for labelling. We also provided 30 s of data as background activities for labelling. One example of the labelling interface is shown in Figure 4-3.

4.2.2 Features: quantitative parameters

In this study, we classified discharges into spike and non-spike using features extracted from abnormal discharges and the background data. We denote the discharge to be determined as $s(n)$ and $s(n) = s_a(n/f_s)$, where f_s is the sampling frequency and $s_a(\cdot)$ represents the continuous signal. The 1 s and 3 s background data around the discharges are represented by $b_1(n)$ and $b_3(n)$.

We performed statistical measures and frequency spectrum analysis on detected discharges and background data. One of the characteristics of interictal spikes is that they stand out from the background data. The three features we obtained were:

1. The absolute maximal peak value of the detected discharges $s_p = \max[|s(n)|]$. The amplitude was calculated on the z-scored VS time series; thus, it showed the amplitude of the discharge relative to the whole VS segment.
2. The kurtosis obtained on the 3 s background data $k_3 = g_2[b_3(n)]$, which revealed the local data distribution around the detected discharges.
3. The relative spectrum power of alpha band $RP = \frac{P_{al}[b_1(n)]}{P_{rest}[b_1(n)]}$, where $P_{al}[b_1(n)]$ is power spectrum of 8-12 Hz and $P_{rest}[b_1(n)]$ is the sum of power spectrum at 3-7 Hz and 13-70 Hz. This variable was used to distinguish the interictal spikes and alpha waves, which is one of the most common physiological waveforms present in patients' resting state recordings.

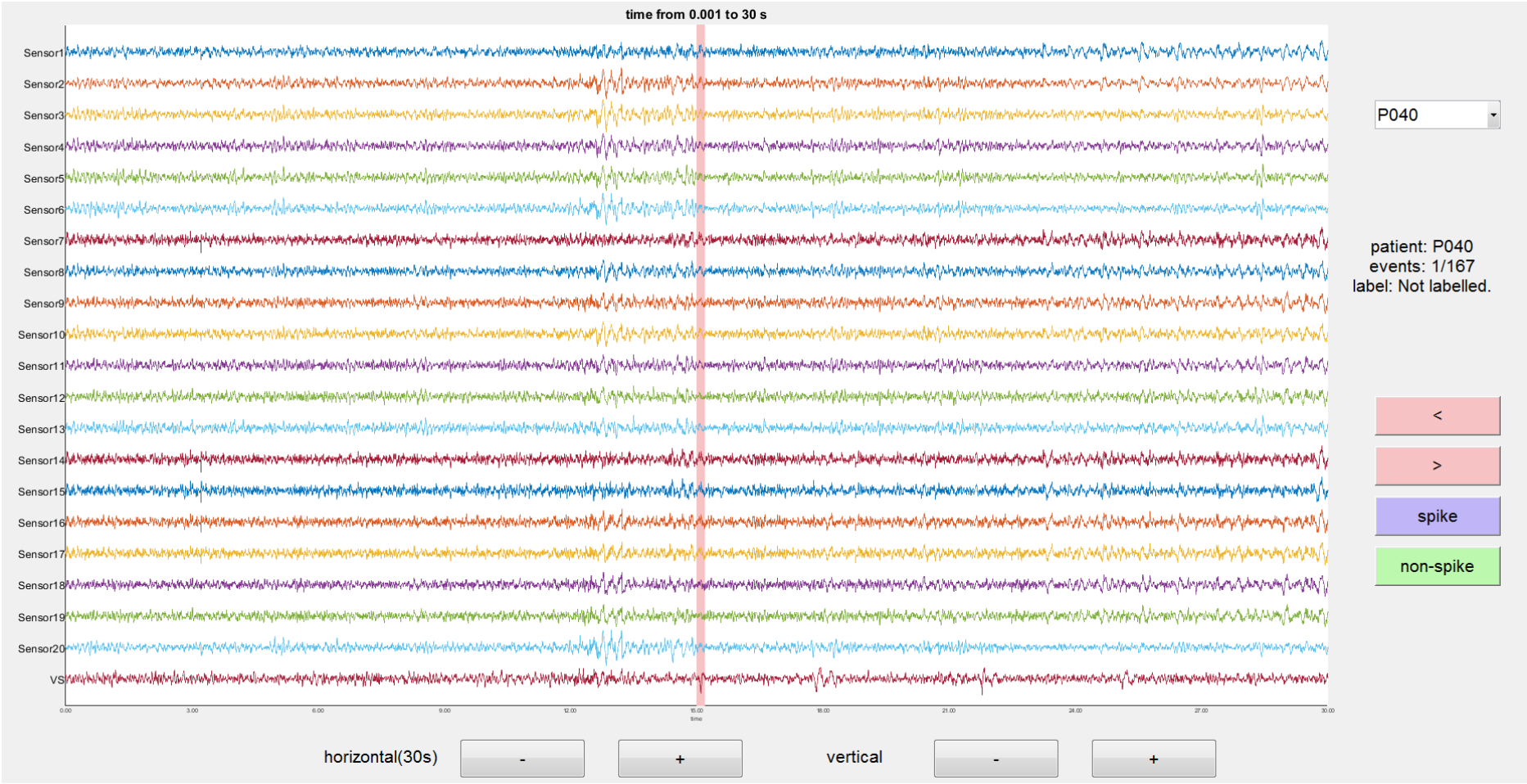

Figure 4-3 Example of labelling interface. The bottom time series is the VS, on which one abnormal discharge was detected and highlighted by the colour pink. The corresponding time series on 20 MEG sensors were shown above the VS. Readers can adjust the horizontal and vertical scales of time series shown on the screen by clicking button '-' and '+' next to the label 'horizontal' and 'vertical'. The '30s' in the brackets following 'horizontal' represents the time series length shown in this screen is 30 s. On the right side of the interface, readers can choose one patient to label from the menu. Clicking button '<' and '>' can show the previous and the next discharge, respectively. The button 'spike' and 'non-spike' can be clicked by readers to label a discharge as spike or non-spike.

We also obtained morphological parameters as interictal spike detection features. In the literature, the most commonly used variables to quantify spike discharges are duration, sharpness and slopes (Adjouadi, Sanchez, et al., 2004; Dingle et al., 1993; Exarchos et al., 2006; Gotman & Gloor, 1976; İnan & Kuntalp, 2007a; Tzallas et al., 2006; Webber et al., 1994). We calculated similar parameters to evaluate the morphologies on the sign corrected and smoothed detected discharges. We performed the sign correction on discharges using

$$s_{\text{sign}} = \text{sgn}\left[s(n_p)\right] \cdot s(n)$$
$$n_p = \text{argmax} \ \ |s(n)| \tag{4.5}$$

We applied Savitzky-Golay smoothing filters on the sign corrected signal s_{sign} and we denote the smoothed discharges as $\tilde{s}(n)$. We calculated the following variables to quantify the morphology of discharges, which are illustrated in Figure 4-4. In Figure 4-4, the solid line represents $\tilde{s}(n)$ and the peak of $\tilde{s}(n)$ is $\tilde{s}(n_p)$, which is illustrated by a dot denoted by p. The local minima along the two sides of the peak p are indicated by m_1 and m_2, and the relative height of the peak p to m_1 and m_2 are d_1 and d_2, respectively. The corresponding sample of the peak p, local minima m_1 and m_2 are located at sample n_p, n_1 and n_2, respectively.

- Width of the peak: w_p. The prominence of the peak p is Pr_p shown in Figure 4-4, is defined as the smaller relative height of the peak to two local minima (or the endpoint of the curve) along two sides of the peak. The width w_p was determined corresponding to half Pr_p.
- Amplitude difference between rising and falling slopes d_{12}. Considering the amplitude of the detected discharges, we normalised the slope differences $|d_1 - d_2|$ by $\max(d_1, d_2)$.
- Duration between points m_1 and m_1: $n_{12} = n_2 - n_1$. We also included the smaller slope duration $n_s = \min(n_2 - n_p, n_p - n_1)$.

In addition to the morphological parameters measured from the sign-corrected and smoothed discharges, following parameters were also generated to examine the background activities and signal-to-noise ratios of the discharges:

- Multiple phases measure d_m. The abnormal discharges can have multiple peaks in addition to the maximal peak. The amplitude difference between the peak with the maximum amplitude and other peaks were obtained and denoted as d_m. Brain physiological oscillations tend to have small d_m, while typical interictal spikes have a relatively large d_m,

which can result from normal brain activities around spikes or the slow wave discharges following spikes. An example of the multiple phase measure d_m is shown in Figure 4-4, in which the additional peak following the discharge is shown by the dotted line with peak point p_m. The height difference between the peak p_m and the maximal peak p is the multiple phase measure d_m.

- Signal quality: d_{sm}. In order to estimate the morphology of discharges, we performed smoothing on the detected discharges using Savitzky-Golay filter. The signal quality measure d_{sm} is the Euclidean distance between the smoothed discharge and the original discharge in the discharge span $[n_1, n_2]$, which are the positions of points m_1 and m_2. The distance d_{sm} can reveal the amount of noise removed by the smoothing procedure.

In our study, we also included the morphological measures of slow waves present in the interictal spike discharges. A spike with a sharp event and a slow wave discharge is shown in the Figure 4-5. The point a is the maximal peak of the discharge. We included the following local minimum b, the local maximum c and the local minimum d in the temporal sequence to

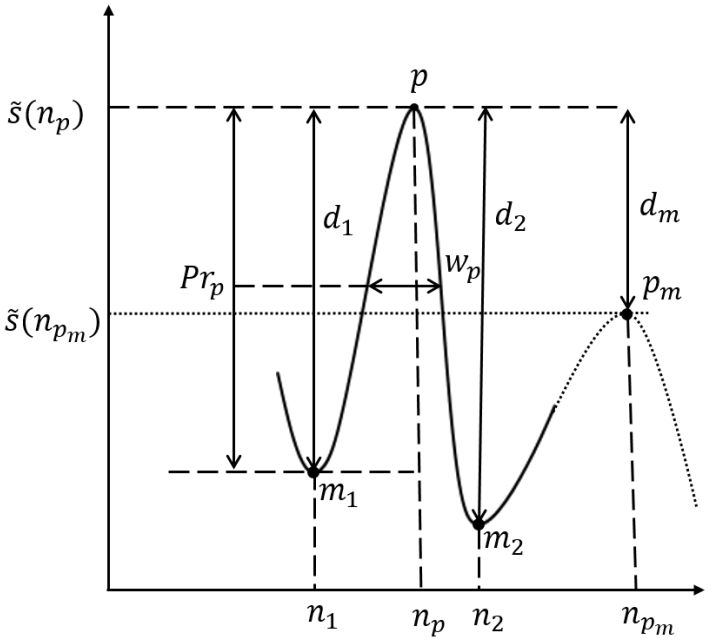

Figure 4-4 Morphological parameters of a discharge. The sign-corrected and smoothed detected discharge is shown by the solid curve, whose maximal peak is the point p located at sample n_p. The prominence of the peak p is p_{r_p}. The width of the peak w_p is the half prominence width. The two local minima located along two sides of the peak p are points m_1 and m_2, and their corresponding samples are n_1 and n_2, respectively. The distance of local minima points m_1 and m_2 to the peak p are d_1 and d_2, respectively. An example of a multiple phase is illustrated by the dotted curve, whose peak is indicated by the point p_m located at sample n_{p_m} and its distance to the maximal peak p is d_m.

quantify the repolarization component. We defined the slope magnitude as the absolute difference of the amplitude between the start point and the end point of the slope. The slope magnitudes for slopes ab, bc and cd are shown in Figure 4-5 as d_{ab}, d_{bc} and d_{cd}, respectively. The following variables were used for the repolarization quantification:

- The repolarization wave magnitude: d_r. The slow wave magnitude is the amplitude difference between the peak a and the peak c, $d_r = d_{ab} - d_{bc}$.
- The relative magnitude of slope bc and slope cd: $\bar{d}_{bc}$ and $\bar{d}_{cd}$. $\bar{d}_{bc}$ and $\bar{d}_{cd}$ are the magnitudes d_{bc} and d_{cd} normalized by the distance d_{ab}.
- The widths of points b and c: w_b and w_c. The width is defined as the sample span in which the amplitude at point $b(c)$ increases (decreases) by half of the smaller slope magnitude between two slopes along two sides of the point b (c). In Figure 4-5, since the slopes along two sides of the point b are d_{bc} and d_{ab} and $d_{bc} < d_{ab}$, the width w_b is the sample span in which the amplitude of the point b increases by $\frac{d_{bc}}{2}$. The width w_c is the sample span in which the amplitude of the point c decreases by $\frac{d_{cd}}{2}$, $d_{cd} < d_{bc}$.

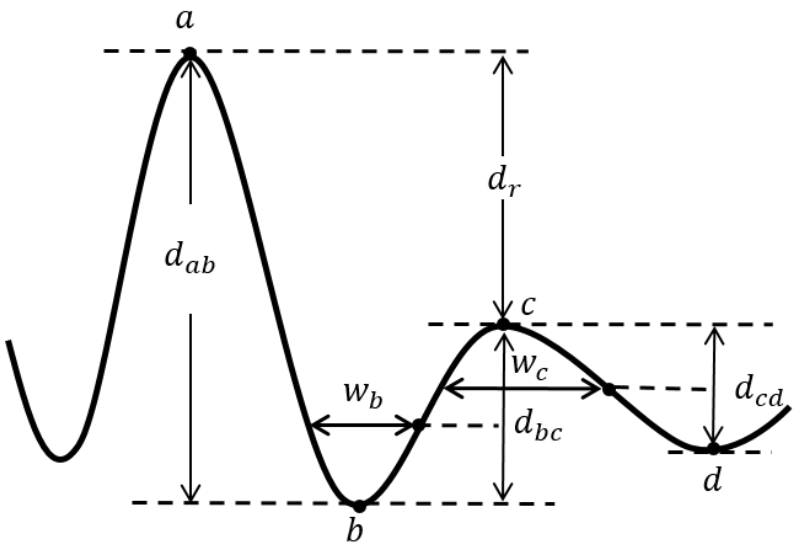

Figure 4-5 An interictal spike with sharp wave and repolarization. The peak of the spike is point a. Points b, c and d are the following minima and maxima. The slope magnitudes for slopes ab, bc and cd are d_{ab}, d_{bc} and d_{cd}, respectively. The repolarization magnitude is d_r. The wave widths for points b and c are w_b and w_c, respectively.

4.2.3 Classification

The classifier applied to the features introduced in Section 4.2.2 was a machine learning ensemble method: bootstrap aggregating, which is also called bagging (Breiman, 1996;

Breiman, 2001). This method generates bootstrap replicas from the training dataset with replacement and applies a homogeneous weaker learner to each bootstrap dataset. Bootstrap replicas were randomly sampled N instances from the training dataset with size N. The weaker learner we used for the bagging was the decision tree classifier. For the binary classification problem, the predicted class for an observation from the trained classification model is the class that yields the largest average of the posterior probabilities computed across all the weaker learners, which was a decision tree in our application.

Leave-one-patient-out cross validation was applied to validate the generalization of the classification method. In one round of cross validation, the samples of one patient are the test data and the samples of all the remaining patients are the training dataset. Additionally, the numbers of "spike" and "non-spike" labels were imbalanced, which would contribute to a bias in favour of the majority class ("non-spike"). We applied the synthetic minority oversampling technique (SMOTE) to generate synthetic instances from the minority class (Chawla et al., 2002). We denote the sample size ratio of the oversampled minority class and the original minority class as

$$r_{\mathrm{SMOTE}} = \frac{n'_{\mathrm{mi}}}{n_{\mathrm{mi}}}, \tag{4.6}$$

where n_{mi} is the sample size of the original minority group and n'_{mi} is number of observations in the oversampled minority group. The ratio between the sample size of the oversampled minority group and the majority groups can be denoted as

$$r_{mi-ma} = \frac{n'_{\mathrm{mi}}}{n_{\mathrm{ma}}} = r_{\mathrm{SMOTE}} \cdot \frac{n_{\mathrm{mi}}}{n_{\mathrm{ma}}}, \tag{4.7}$$

where n_{ma} is the sample size of the majority group. To determine the oversampling ratio r_{SMOTE}, we evaluated r_{mi-ma} versus averaged area under the curve (the averaged AUC, see Section 4.2.5). The range of r_{mi-ma} was modulated by the SMOTE ratio r_{SMOTE} with

$$\left\{ r_{\mathrm{SMOTE}} | r_{\mathrm{SMOTE}} \geq 2, r_{\mathrm{SMOTE}} \cdot \frac{n_{\mathrm{mi}}}{n_{\mathrm{ma}}} \leq 13 \right\}. \tag{4.8}$$

4.2.4 Association between features

We have 14 features designed in Section 4.2.2 . We used Spearman's rank correlation to evaluate the association between all the features. Hierarchical clustering was applied to cluster

all the correlated features. The correlation among features were performed using function: *corrplot*() of a R package (Wei et al., 2017).

4.2.5 Performance criteria

The receiver operating characteristic (ROC) curve was used as the performance metric for the classification method. The ROC curve is a plot of the true positive rate (sensitivity) against the false positive rate (1-specificity) of the classifier as threshold is varied. The area under the ROC curve (AUC) indicates the discriminatory ability of a classifier. The higher AUC is, the better the discriminatory ability of a classifier. The maximum AUC is 1, which indicates a perfect classifier, while AUC of 0.5 indicates a classifier with no discriminatory power (chance performance).

For each leave-one-patient-out cross validation, the classifier was trained with 12 out of the total 13 patients and was tested on the remaining one patient. We performed 50 iterations for each cross-validation round. It is worth noting that there are two ways to combine the ROC curves of 50 iterations for each cross-validation (Bradley, 1997):

1. Pooling. The ROC curve is generated by the true positive rate and the false positive rate of the classifier with various thresholds. Each point on the combined ROC curve is generated by averaging the true positive rate and the false positive rate points generated from the 50 iterations around it. In our study, the moving average with a sliding window that included 10% of all the points generated from 50 iterations was applied to produce the combined ROC curve. An example of the pooling method is show in Figure 4-6, in which the red solid line represents the combined ROC curve from the points on the ROC curves generated in 50 iterations, which are illustrated by the grey dots, using the pooling approach.
2. Averaging. An alternative approach to combine ROC curves from multiple iterations is to adopt the parameter AUC. The AUC can be generated from the ROC curve of each iteration. The ROC curve characteristics from multiple iterations can be combined by averaging the AUC of each iteration. An issue with this approach is that it cannot contribute to a combined ROC curve directly but characterises it with the parameter AUC.

We used the SMOTE method to oversample the instances in the minority group. To determine the optimal sample size ratio r_{SMOTE}, we applied leave-one-patient-out classification with various SMOTE parameter r_{SMOTE} shown in Eq. (4.8). We performed 50 iterations for each setting and used the average method to combine the ROC curves, which was the averaged AUC

across 50 iterations, to evaluate the performance. The averaged AUC for each patient with various SMOTE ratio r_{SMOTE} shown in Eq. (4.8) can be expressed as

$$\overline{\mathrm{AUC}}_{p_i} = \sum_{r_{\mathrm{SMOTE}}} \overline{\mathrm{AUC}}_{p_i}(r_{\mathrm{SMOTE}}). \tag{4.9}$$

Then, we calculated the averaged AUC across all 13 patients

$$\overline{\mathrm{AUC}} = \sum_{i=1}^{13} \overline{\mathrm{AUC}}_{p_i}. \tag{4.10}$$

The averaged AUCs across all the patients for each group size ratio r_{mi-ma} were obtained to determine the optimal r_{SMOTE}. Since AUC=0.5 indicates a classifier with no discriminatory power, we performed a statistical test to determine whether the AUC of a classifier was different from 0.5 (Mandrekar, 2010). The null and alternative hypothesis were

$$\begin{aligned} H_0&: \mathrm{AUC} = 0.5, \\ H_1&: \mathrm{AUC} \neq 0.5. \end{aligned} \tag{4.11}$$

Let's denote the estimated AUC as θ. The t-test can be tested on the statistic

$$\frac{\theta - 0.5}{\mathrm{SE}(\theta)}, \tag{4.12}$$

where $\mathrm{SE}(\theta)$ is the standard error of the estimated AUC θ. $\mathrm{SE}(\theta)$ can be given by the standard error of the Wilcoxon statistic $\mathrm{SE}(W)$ (Hanley & McNeil, 1982) as

$$SE(W) = \sqrt{\frac{\theta(1-\theta) + (N_p - 1)(Q_1 - \theta^2) + (N_n - 1)(Q_2 - \theta^2)}{N_p N_n}}, \tag{4.13}$$

where N_p and N_n are the numbers of negative and positive observations, respectively, and

$$Q_1 = \frac{\theta}{(2-\theta)} \text{ and } Q_2 = \frac{2\theta^2}{(1+\theta)}. \tag{4.14}$$

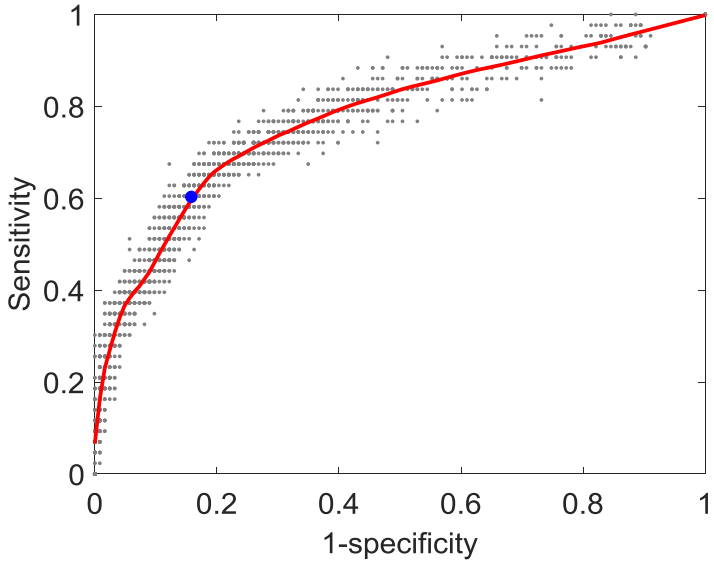

Figure 4-6 The combined ROC curve using the pooling method . The grey dots show the points of ROC curves from all 50 iterations. The red solid line represents the combined ROC curve. The blue dot represents the sensitivity and specificity obtained using the combination method average.

To assess whether the classifier in this study had discriminatory power, we performed the z-test on the statistic in Eq. (4.12). The critical value for 5% two tailed is 1.96. If the standard score in Eq. (4.12) is greater than 1.96, the null hypothesis is rejected and the AUC is significantly greater than 0.5. Furthermore, we evaluated the classification performance with leave-one-patient-out cross validation for each patient using sensitivity and specificity:

$$\text{Sensitivity} = \frac{\text{TP}}{\text{TP} + \text{FN}}, \qquad \text{Specificity} = \frac{\text{TN}}{\text{TN} + \text{FP}}, \tag{4.15}$$

where TP is true positive, FN is false negative, TN is true negative and FP is false positive. The sensitivity and specificity of the classifier for each patient were the averaged sensitivity and specificity across 50 iterations. An example of the averaged sensitivity and specificity is shown by the blue dot on the combined ROC curve using pooling method in Figure 4-6.

4.2.6 Cross-reader agreement evaluation

Labels of representative discharges were made by three readers in this study: two from experienced neurophysiologists US and WD and one from an experienced researcher RL (the author). The performance of classifier was evaluated using sensitivity, specificity and AUC introduced in Section 4.2.5 . To evaluate the cross-reader agreement, we adopted similar

performance criteria including sensitivity and specificity. In this procedure, we considered annotations from one reader as the reference and evaluated the agreement of labels from the remaining readers against the reference. The sensitivity and specificity generated from the inter-reader agreement were compared with the sensitivity and specificity of the classifier trained using labels from the reference reader.

Additionally, the AUC was also adopted to evaluate the performance of inter-reader agreement. However, we can only obtain a confusion matrix for the agreement between readers. Therefore, we estimated the approximate AUC from the sensitivity and specificity (Idrees et al., 2017), which can be expressed as

$$\widehat{\mathrm{AUC}} = \frac{1}{2} \cdot (\text{Sensitivity} + \text{specificity}). \tag{4.16}$$

To be consistent, the AUC of the classifiers in these cases were calculated using Eq. (4.16) rather than the ROC curve introduced in Section 4.2.5

4.3 Results

4.3.1 Ratio used for SMOTE

Because the two groups of data "spike" and "non-spike" were imbalanced, we applied the SMOTE method to oversample the minority group to reduce the bias in favour of the majority class. We evaluated the performance of various SMOTE ratios using averaged AUC versus the ratio between the minority group and the majority group r_{mi-ma}. The averaged AUC used was the averaged AUC across 13 patients with 50 runs. The sample ratio of two groups used to evaluate SMOTE ratio was $r_{mi-ma} = r_{\mathrm{SMOTE}} \cdot \frac{n_{\mathrm{mi}}}{n_{\mathrm{ma}}}$ with $\left\{ r_{\mathrm{SMOTE}} | r_{\mathrm{SMOTE}} \cdot \frac{n_{\mathrm{mi}}}{n_{\mathrm{ma}}} \leq 13 \right\}$. The evaluation curves obtained for three readers are shown in Figure 4-7(a), (b) and (c). The blue dashed lines in the figure represent the performance of the classification without applying SMOTE to oversample the minority group. As can be seen, the performance of the classification with the SMOTE method outperformed the classification performance without SMOTE for all the SMOTE values shown in the figure. For reader RL shown in Figure 4-7(c), the averaged AUC monotonically increased with increasing r_{mi-ma} and the increase stabilized from the ratio $r_{mi-ma} = 6.74$. Similar monotonic increase can be observed in the r_{mi-ma} range [1.17, 5.87] in Figure 4-7(a) for reader US, and the evaluation curve fluctuates after the

(a)

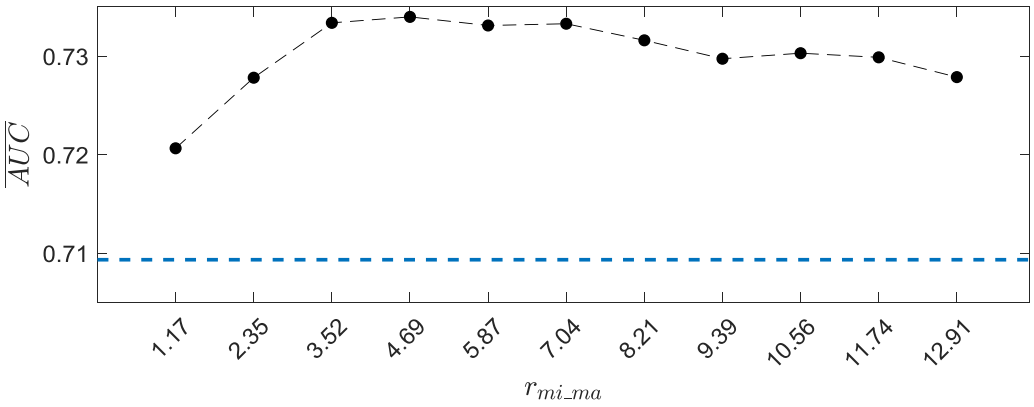

(b)

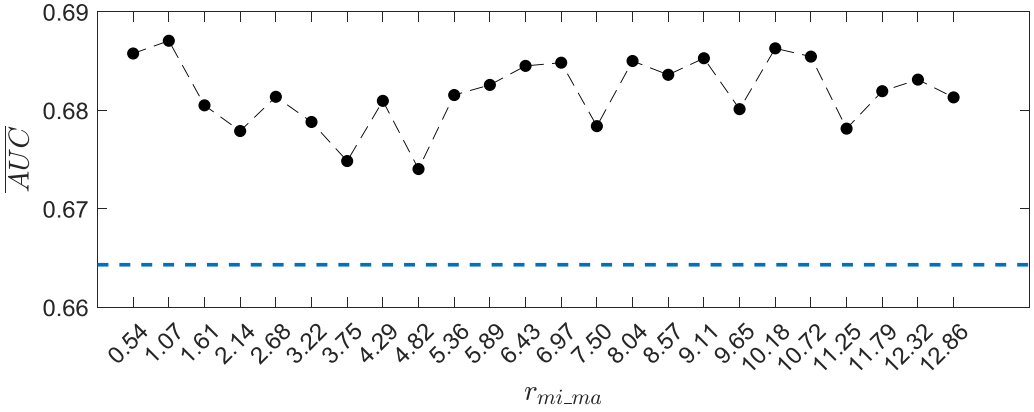

(c)

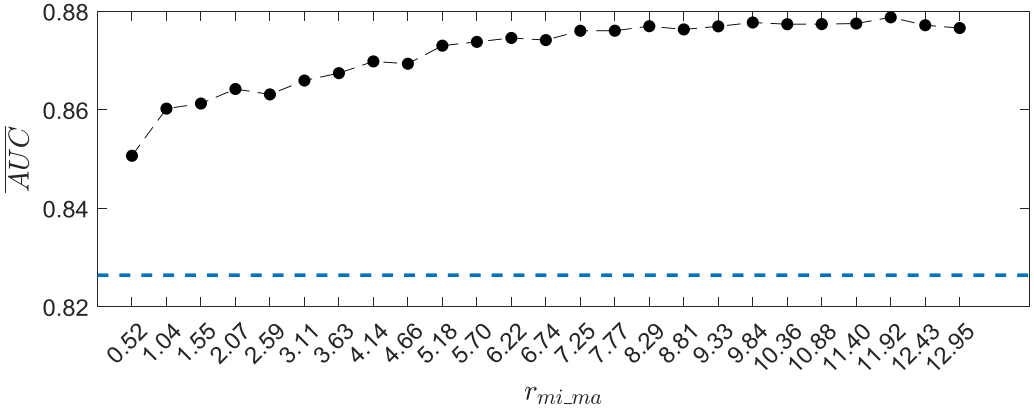

Figure 4-7 The averaged AUC and r_{mi-ma} curve for three readers (a) US, (b) WD and (c) RL. The x-axis is the sample size ratio between two groups r_{mi-ma}, while the y-axis is the corresponding averaged AUC. Each back dot represents one r_{mi-ma} parameter and its corresponding averaged AUC. The blue dashed line represents the averaged AUC without applying SMOTE method to balance the data.

Table 4-1 Number of "spike" and "non-spike" labelled by three readers (neurophysiologists: US and WE; experienced researcher: RL). The number of spike labels are given in the column #spike, while the number of non-spike annotations are given in the column #non-spike. The sample size ratio between spike and non-spike class are listed in the last column.

Patient	#spike	#non-spike	#spike/#non-spike
US	399	680	0.5868
WD	228	851	0.2679
RL	222	857	0.2590

point 5.87. However, there was no monotonic increase but only fluctuations observed in Figure 4-7(b) for reader WD. The optimal point $[r_{mi-ma}, \overline{\text{AUC}}]$ is the point with the highest averaged AUC value, which was [4.69, 0.73], [1.07, 0.69], and [5.70, 0.87] for readers US, WD and RL, respectively. However, we can apply the uniform two group size ratio $r_{mi-ma} \approx 6$ for the SMOTE method for the three readers, at which the averaged AUC were 0.73, 0.68 and 0.87 at r_{mi-ma} were 5.87, 5.89 and 6.22, respectively. Their $\overline{\text{AUC}}$ differences to the optimal $\overline{\text{AUC}}$ were all less than 0.01, which indicates the choice of $r_{mi-ma} \approx 6$ for three readers had similar classification performance compared with the optimal values.

Additionally, we can see from (a), (c) and (d) in Figure 4-7 that the x-axis in (a) is sparser than the x-axis in (b) and (c). The non-uniform x-axis was because r_{mi-ma} was modulated by the SMOTE ratio r_{SMOTE} and multiplied by a constant $n_{\text{mi}}/n_{\text{ma}}$, which varied between the three readers. The change of r_{mi-ma} by increasing r_{SMOTE} was greater for readers with greater $n_{\text{mi}}/n_{\text{ma}}$. The sample sizes for spike and non-spike classes and their ratios are given in Table 4-1. For reader US, the group size ratio was $n_{\text{mi}}/n_{\text{ma}} = 0.59$, while $n_{\text{mi}}/n_{\text{ma}}$ of the remaining two readers were 0.27 and 0.26. Because reader US had the greater value of $n_{\text{mi}}/n_{\text{ma}}$, the increase step of r_{mi-ma} was greater and the x-axis was sparser.

4.3.2 Association between features

We performed hierarchical clustering with Spearman's rank correlation to identify associations among features. Spearman's rank correlations are shown in Figure 4-8, in which the numbers in the square show the Spearman's correlation coefficients. The number of clusters were adjusted to ensure correlations between features in one cluster are less than 0.8. The clustered features are indicated by the black squares. We can see that features n_{12} and n_s were highly correlated with coefficient 0.86. n_{12} is the duration between two local minima along the peak:

m_1 and m_2, while n_s is the smaller of the durations of the rising slope and the falling slope. The high correlation between these two features indicates that if the duration of a peak was small, the rising or falling slope of the peak also tended to be small. Other highly correlated (>0.8) features were w_p and d_{sm}, which implies that the peak with longer duration tended to have larger distance between the original discharge and the smoothed discharge. This is because the Euclidean distance is related to the length of the data. The remaining features do not show correlation coefficient over 0.8, which suggests that the features designed in this study were not redundant.

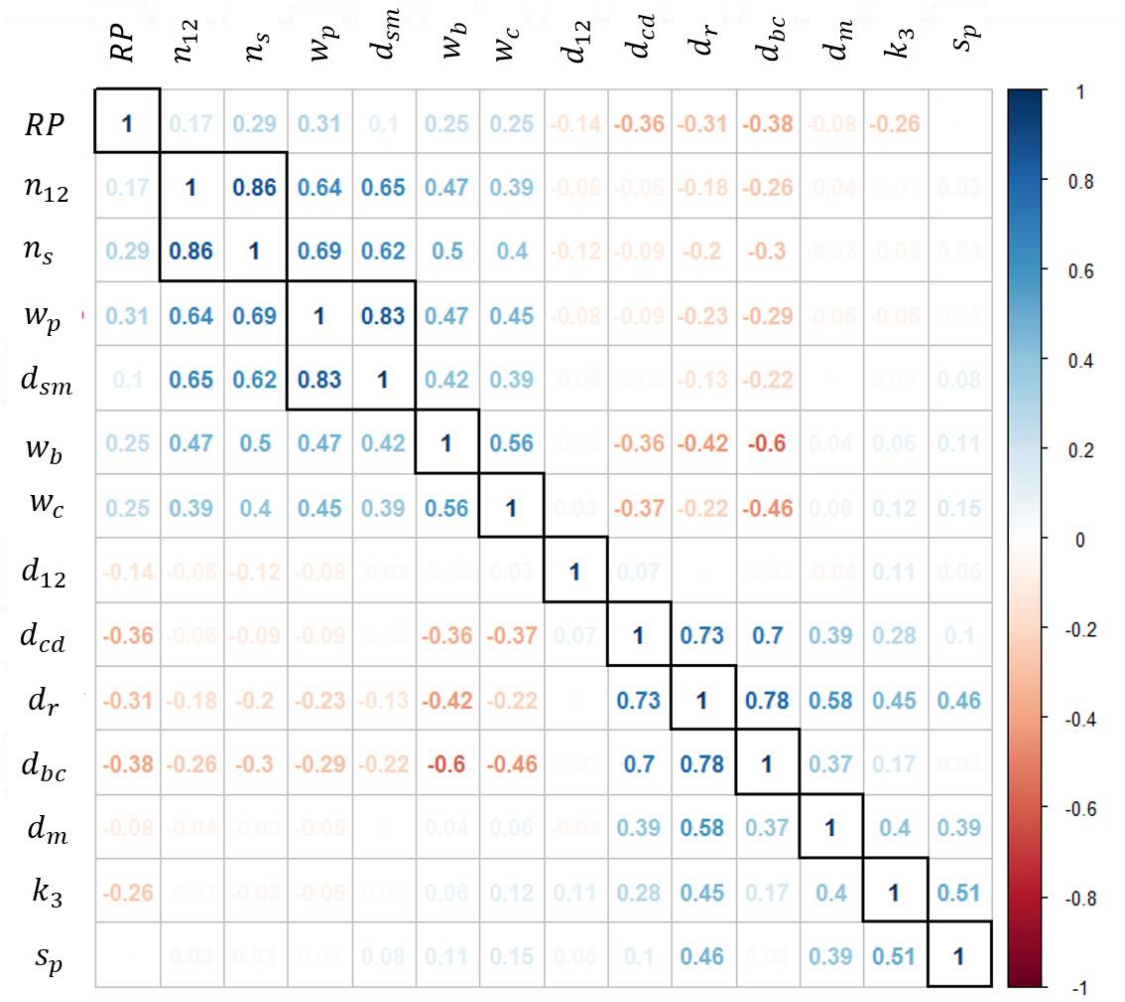

Figure 4-8 Features clustered by Spearman's rank correlation . The blue colour indicates high positive correlations and the red colour indicates high negative correlation. The pale colours indicate little or no correlation present. The number in each square shows Spearman's rank correlation coefficient between a pair of features. The clustered features are outlined by black squares.

4.3.3 Performance of classification for each patient

We averaged sensitivity and specificity for each patient using the bagging classifier with oversampling parameters that satisfied $r_{mi-ma} \approx 6$ over 50 iterations. The averaged sensitivity and specificity for each patient with labels of all three readers are shown in Figure 4-9. The averaged sensitivity and specificity across thirteen patients are shown in the last column of each figure. Both the sensitivity and specificity with the reader RL show in Figure 4-9(c) are above 75%, while the sensitivity for the reader US (see Figure 4-9(a)) and the specificity for the reader WD (see Figure 4-9(b)) are above 75%. Overall, the performance of the classifier validated against the annotations from two neurophysiologists are moderate, while the performance validated against the researcher RL is stronger with averaged sensitivity 77.3% and 81.8% specificity.

We obtained the combined ROC curve for each patient with the pooling method introduced in Section 4.2.5 with classifiers trained by spike labels from two neurophysiologists and one researcher shown in Figure 4-10 (a), (c) and (c), respectively. The averaged sensitivity and specificity shown in Figure 4-9 for each patient is indicated by the square marker on each ROC curve in Figure 4-10. Because the combined ROC curve for each patient and the averaged sensitivity and specificity indicated by the square marker in Figure 4-10 were generated using pooling and average combination methods, respectively. The square marker may not sit directly on the ROC curve in Figure 4-10. The dashed line in Figure 4-10 indicates chance performance. Additionally, we applied the averaged AUC across 50 iterations for each patient to evaluate the performance of the classifier trained with the annotations from the three readers, which is shown in Figure 4-11. We performed the statistical test introduced in Section 4.2.5 to check whether the classifier had the discriminatory capability for each patient. Significant statistical test results are indicated by asterisks above the bar plots, which indicate where the AUC was significantly greater than 0.5 with 5% significance level. Of note, statistical tests for the averaged AUC across all the patients, shown in the last column of the bar plots, were not performed.

For the labels from reader US, the AUC was significantly greater than 0.5 for 10 out of 13 patients (see Figure 4-11(a)), of which P042 and P074 obtained AUC over 0.8 and their ROC curves in Figure 4-10(a) were also very close to the upper left corner.

(a)

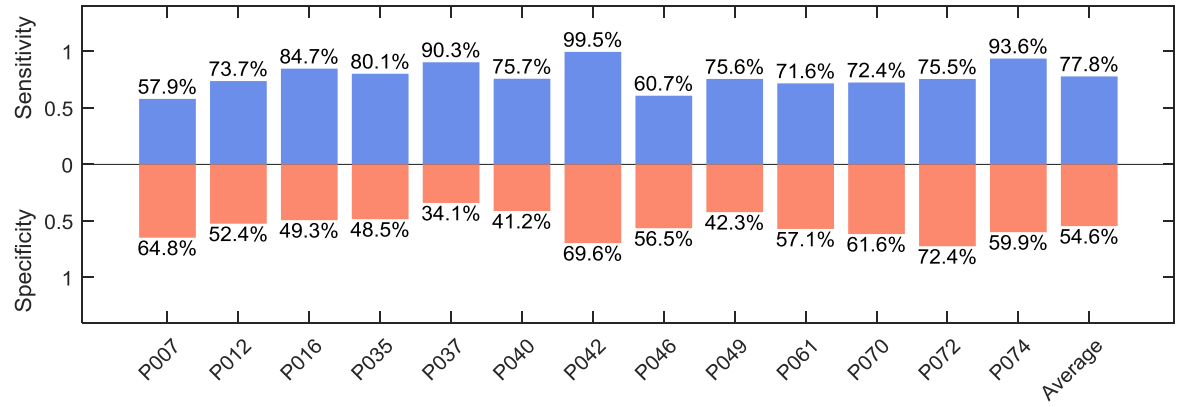

(b)

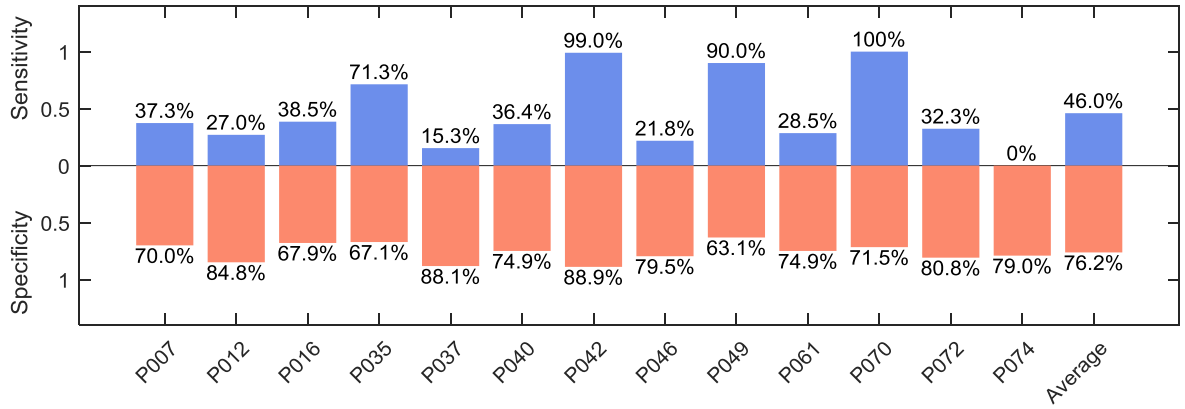

(c)

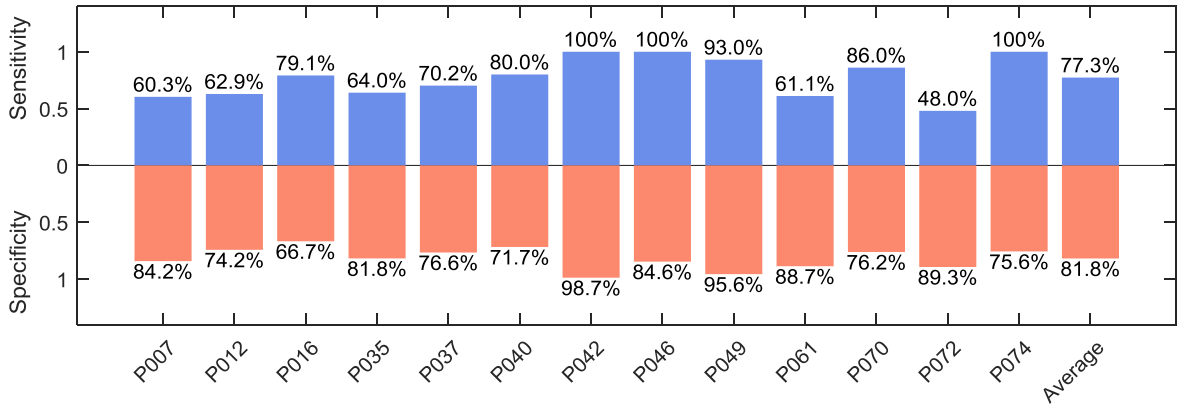

Figure 4-9 The averaged sensitivity and specificity across 50 iterations for each patient with annotations for three readers (a) US, (b) WD and (c) RL. The blue bars represent the sensitivity, while the red bars illustrate the specificity. The last column of each bar plot is the averaged sensitivity and specificity for each reader.

For reader WD, shown in Figure 4-11(b), AUC was significantly greater than 0.5 for only three patients, of which P042 and P070 had AUC over 0.9 and their ROC curves in Figure 4-10(b) were very close to the upper left corner.

The AUCs of the classifier were significantly greater than 0.5 for all 13 patients for annotations from reader RL, of which P042, P046, P049 and P074 obtained AUC over 0.9 and ROC curves were close to the upper left corner as shown in Figure 4-10(c).

The last bars in Figure 4-11 represent the averaged AUCs across 13 patients for the three readers. The classifiers with neurophysiologist readers US and WD labels had fair and poor performance with $\overline{\mathrm{AUC}} = 0.734$ and $\overline{\mathrm{AUC}} = 0.679$, respectively. The classifier with the researcher reader RL labels had good discriminatory capability with $\overline{\mathrm{AUC}} = 0.874$.

(a)

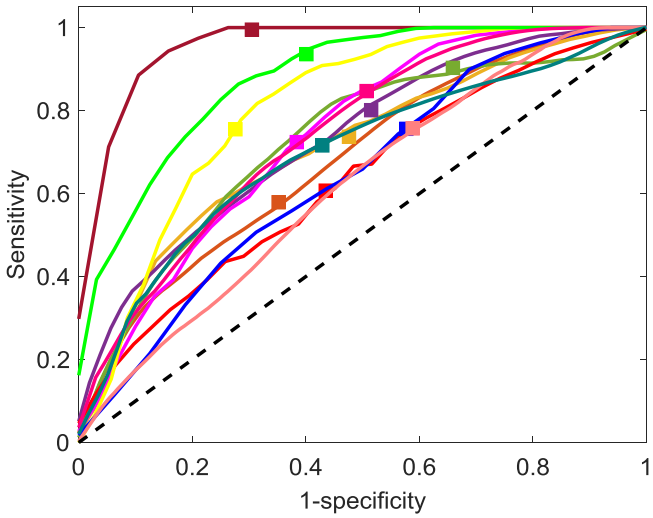

(b)

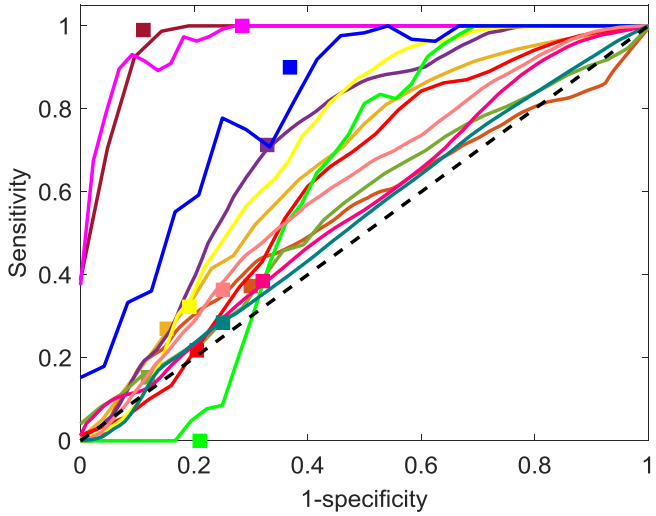

(c)

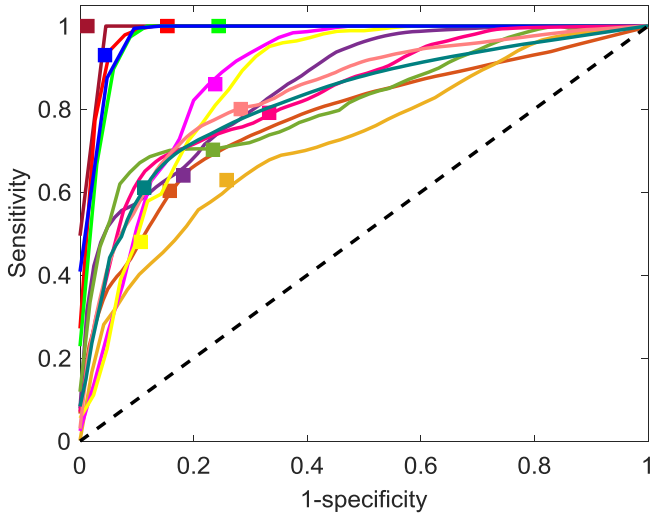

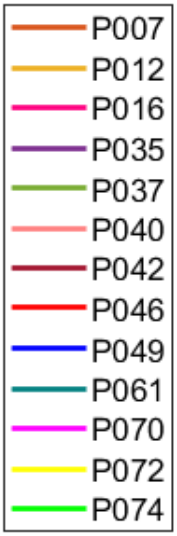

Figure 4-10 The combined ROC curves using the pooling method for each patient with the classifier trained by labels from readers (a) US, (b) WD and (c) RL. Each colour represents one patient, which are labelled by the legend on the right. The square marker associated with each ROC curve is the averaged sensitivity and false positive rate from 50 iterations for each patient.

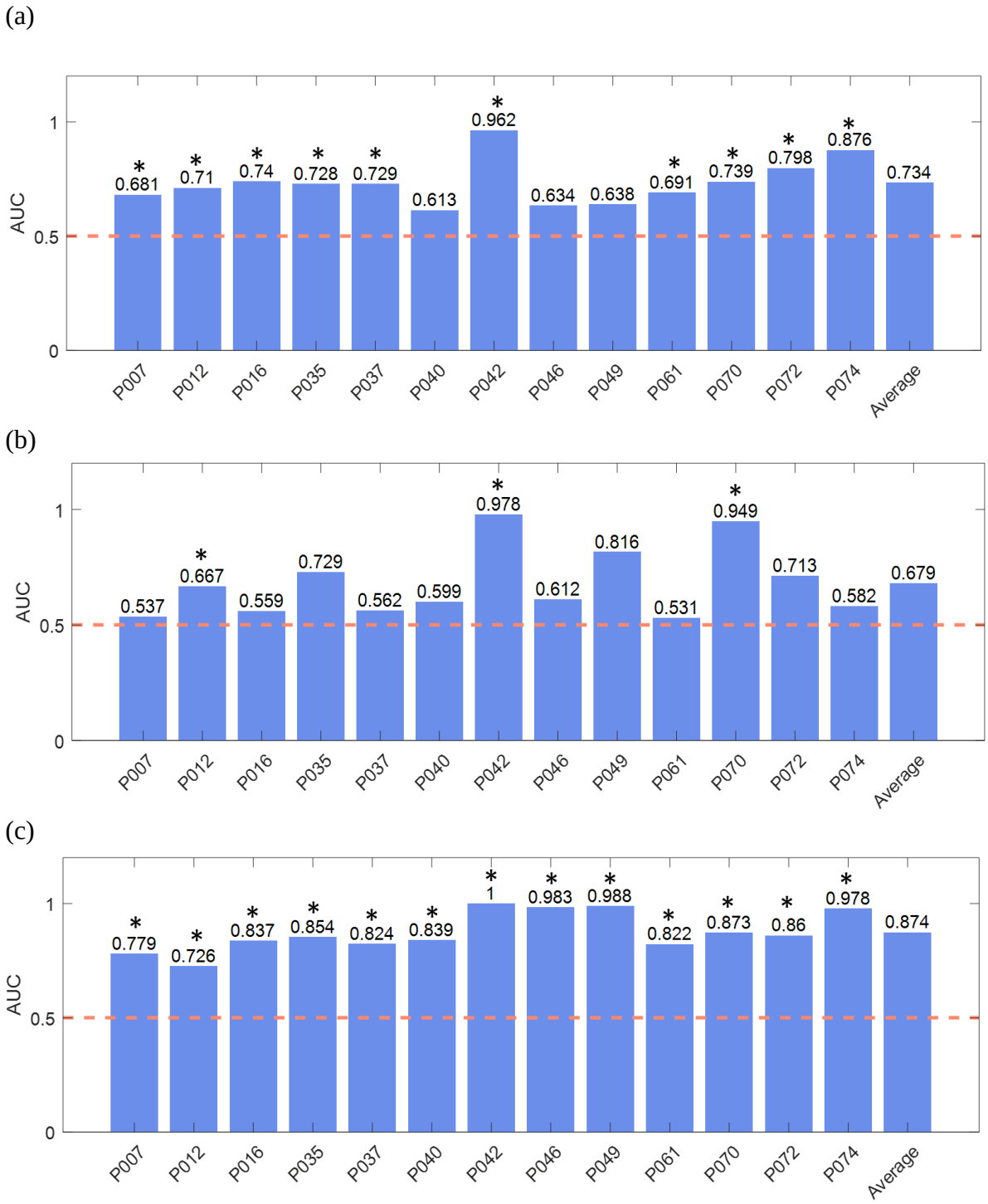

Figure 4-11 The averaged AUC for each patient with annotations from three readers (a) US, (b) WD and (c) RL. Each bar represents the AUC for one patient; the last bar of each figure shows the averaged AUC across all thirteen patients. The red dashed line indicates $\overline{\mathrm{AUC}} = 0.5$. The asterisks above the bar plot indicate where the AUC was significantly greater than 0.5 with 5% significance level. The statistical test was not performed on the averaged AUC across patients, so no asterisks are present on the last column of the bar plot.

4.3.4 Cross-reader evaluation

In our study, we acquired spike annotations from two neurophysiologists. Their cross-reader evaluations are shown in Table 4-2. The number of events labelled as "spikes" by both experts are shown in the third column. We can see that one patient had zero events labelled as "spikes" by both experts the same times (P074), while three patients only have one event labelled as "spike" by both experts (P042, P049, P070).

Table 4-2 Cross-reader evaluation between two neurophysiologists. The first column is the patient number. The second column is the total number of events labelled by the experts. The following two columns show the number of "spikes" and "non-spikes" labelled by the experts consistently. The column "#inconsistent events" shows the number of events with different labels for each patient and the percentage of inconsistent labels for each patient is shown in the brackets. The column "#consistent events" shows the number of events with consistent labels for each patient and the percentage of consistent labels for each patient is shown in the brackets. Incidents with only one observation are highlighted by the pink colour and the case with no consistent observations is highlighted by the colour grey.

Patient	#events	#consistent spikes	# consistent non-spike	#inconsistent events	#consistent events
'P007'	166	3	99	64 (38.55%)	102 (61.45%)
'P012'	62	18	19	25 (40.32%)	37 (59.68%)
'P016'	128	22	59	47 (36.72%)	81 (63.28%)
'P035'	95	4	51	40 (42.11%)	55 (57.89%)
'P037'	67	12	27	28 (41.79%)	39 (58.21%)
'P040'	167	3	138	26 (15.57%)	141 (84.43%)
'P042'	23	1	18	4 (17.39%)	19 (82.61%)
'P046'	45	8	19	18 (40.00%)	27 (60.00%)
'P049'	25	1	16	8 (32.00%)	17 (68.00%)
'P061'	172	65	54	53 (30.81%)	119 (69.19%)
'P070'	45	1	30	14 (31.11%)	31 (68.89%)
'P072'	47	4	33	10 (21.28%)	37 (78.72%)
'P074'	37	0	31	6 (16.22%)	31 (83.78%)
Average	1079	142	594	343 (31.79%)	736 (68.21%)

We considered one of the readers as the reference and evaluated the performance including sensitivity and specificity for the remaining readers, this time also including researcher RL (see Figure 4-12(a)). We also included the averaged sensitivity and specificity across all the patients, which are the last bars in Figure 4-9(a), (b) and (c). The three reference readers were US, WD and RL shown in the panels (1), (2) and (3) in Figure 4-12(a), respectively. For all the three reference readers, the classifier outperformed the readers with respect to the sensitivity but was

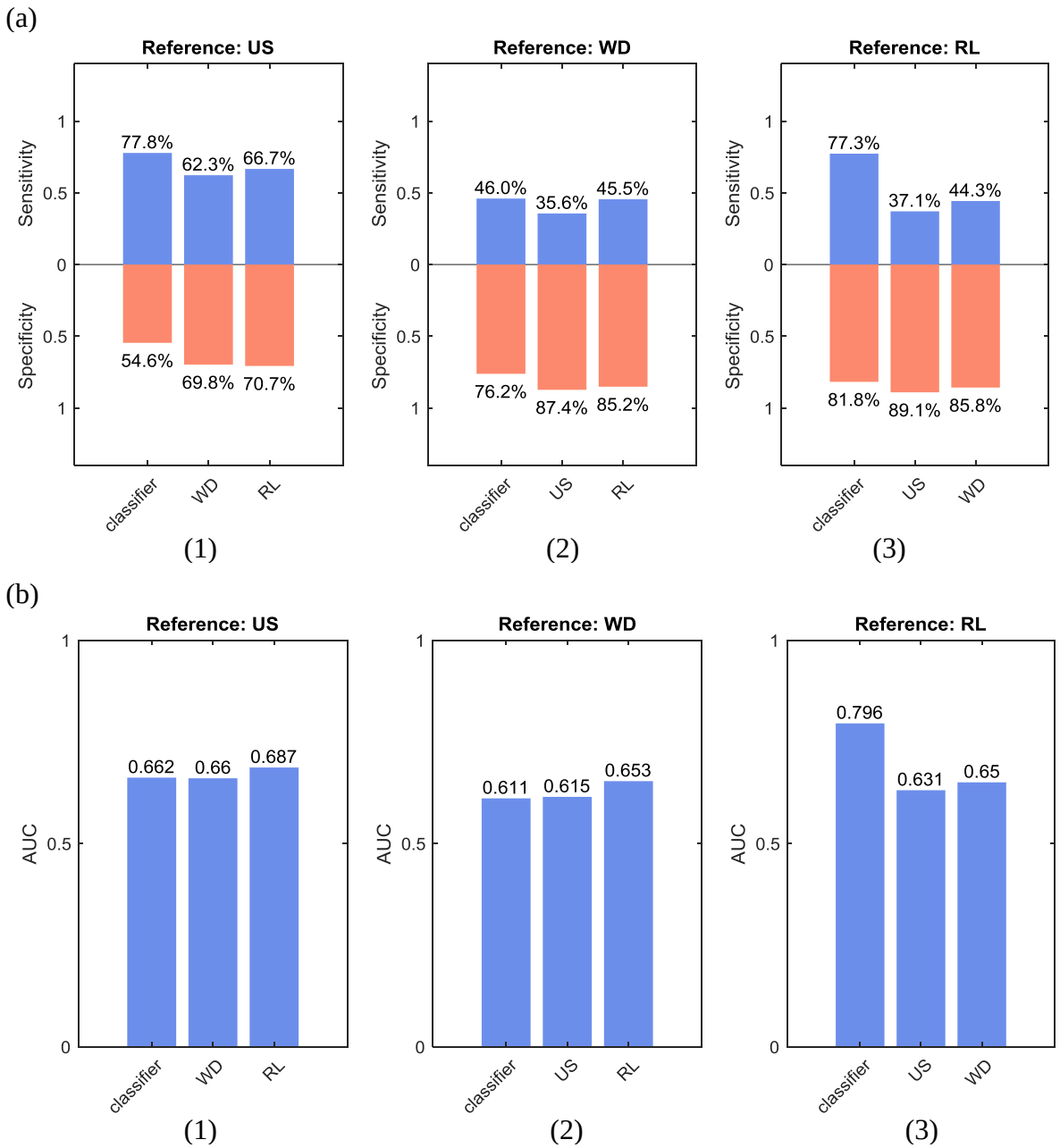

Figure 4-12 Evaluate classifier against cross-reader agreement rate . Comparing the performance of (a) sensitivity and specificity and (b) AUC with different readers as reference. The three columns of (a) and (b) who the performances with reference readers US, WD and RL as indicated. The sensitivity and specificity are shown by the blue bars and red bars, respectively.

inferior to the readers in terms of specificity. But sensitivities and specificities of classifiers can be adjusted by changing threshold that used to classify two groups.

The performances based on AUC of classifier and reader labels with one of the readers as reference are shown in Figure 4-12(b). The AUC for the classifier was also generated using Eq. (4.16) rather than the averaged AUC across thirteen patients shown in Figure 4-11. The averaged AUC in Figure 4-11 for the three readers US, WD and RL were 0.734, 0.679 and 0.874, which were greater than the AUC estimated using Eq. (4.16) with 0.662, 0.611 and 0.796. Thus, we use Eq. (4.16) to estimate AUC to be consistent. With one of the neurophysiologists as reference (US or WD), the classifier performed as good as the other neurophysiologist (WD or US, respectively); their AUCs are shown as the left two bars in Figure 4-12(b) (1) and (2). With the researcher RL as reader, the classifier performance was higher than the two neurophysiologists. It is interesting to note that the researcher (RL) obtained slightly better consistency than the neurophysiologist when considering the other neurophysiologist as reference, which is demonstrated by the right two bars in Figure 4-12(b) (1) and (2).

4.4 Discussion

This work developed an automatic spike detection method on VSs reconstructed from MEG data. The performance of the classifier varied with the discharge labels from different readers. This is because the spike labelling by different neurophysiologists can be different. The agreement rate of discharge labels in this study was 68%. In previous studies, the agreements of cross-reader markings were less than 50% (Black et al., 2000; Scheuer et al., 2017; Webber et al., 1993; Wilson et al., 1996). The heterogeneity of labelling from different neurophysiologists complicates the development of automatic spike detectors. Nonetheless, the performance of the classifier proposed in this study was comparable with the human experts. Still, the limited classification performance trained with labels from different readers indicate the automatic detection method proposed was not flexibly applicable to various neurophysiologists. With the researcher RL as reader (author), the classifier performance was higher than the two neurophysiologists. This is probably because the researcher designed the classifier using the same knowledge about interictal spikes as was used for discharge labelling.

Studies on spike detection on MEG virtual sensors (VSs) have not been developed yet in the literature, although there are two works that proposed methods to detect spikes on MEG sensors (Khalid et al., 2016; Khalid et al., 2017). Khalid et al. (2016) extracted features for spike and non-spike groups using common spatial pattern that can maximise the data variance of one

group and output the unit variance for another group. The linear discriminant analysis was used to classify the features extracted for both classes using common spatial pattern. Linear discriminant analysis can be applied to classify two classes that are normally distributed with equal covariance matrix. The normal distribution of spike and non-spike classes were validated in this study, while the equivalent covariance matrix was not justified in this work.

Later, Khalid et al. (2017) proposed a method that detected abnormal discharges with amplitude over a threshold, then warping path lengths calculated by the dynamic time warping method were used to quantify the similarity across discharges on various channels. Discharges on two electrodes were defined as similar if the warping path length was smaller than a similarity threshold. If the number of electrodes with similar discharges was over a distribution threshold, these discharges were detected as a threshold. In this work, 30 focal epilepsy patients were included. The amplitude, similarity and distribution threshold were estimated on 10 randomly selected epilepsy patients and tested on the remaining 20 patients.

Both studies reported excellent performance, with both sensitivity and specificity exceeding 90%. However, their work cannot be reasonably compared with our study because the detection performances were assessed using different approaches. Khalid et al. (2016) performed evaluation using the leave-one-out method by training the classifier on 48 MEG segments and testing on the remaining one segment. The total 49 segments were from 20 epilepsy patients. The performance of the detector in the Khalid et al. (2017) studies was delivered using cross-validations by partitioning the whole dataset from either 20 patients or 30 patients into training and testing datasets. In our study, the performance of the detector was reported using the leave-one-patient-out procedure, which can quantify the generalisation of this detection method to a broad epilepsy patient cohort.

In addition, it is not fair to compare performance of classifiers across different studies directly, since the number of patients, duration of recordings and variability of spikes are not consistent. It is important to compare the performance of spike detection methods against cross-reader agreement rate within a study, since classifiers or parameters of detection methods are trained or estimated from labels achieved in the same study. However, both studies did not report cross-reader agreement rate, so the heterogeneities of spikes included in these two studies remain unclear.

The manual inspection of VSs to confirm the presence of authentic interictal spikes has been widely implemented for kurtosis beamforming to improve the performance of EZ localisation

artefacts (Agirre-Arrizubieta et al., 2014; de Gooijer-van de Groep et al., 2013; Hall et al., 2018; Kirsch et al., 2006; Oishi et al., 2006; Rose et al., 2013; Tenney et al., 2014). The number of VSs is of the order of ten and the manual inspection can be tedious and cumbersome especially when the MEG recording is about one hour. The detection of interictal spikes on MEG VSs can help this manual inspection.

Additionally, the association of interictal spikes with the seizure onset zone or the surgical resection with seizure-free surgical outcome are still under debate (Bartolomei et al., 2016; Conrad et al., 2019; Goncharova et al., 2009; Hufnagel et al., 2000; Libenson et al., 2014). Goncharova et al. (2009) showed that the spatial distribution of spike rates is associated with the location of the seizure onset, but the area with the highest spike rate coincided with the seizure onset zone, where seizures start, in only half of the patients. Libenson et al. (2014) showed that the frequency of spikes is instable by comparing consecutive nights of sleep. Hufnagel et al. (2000) showed that the earliest spike in a sequence across the brain and the spike with the highest amplitude are good indicators of the EZ. Bartolomei et al. (2016) showed that maximal SI (spike frequency index) and maximal EZ (epileptogenicity index) were consistent in 18 out of 32 patients, and this consistency showed up in 15 out of 20 in patients with FCD (focal cortical dysplasia). Conrad et al. (2019) showed that the intracranial electrode with the highest spike frequency can localise the seizure onset zone. The spike automatic detection method on VS MEG enables the spatiotemporal analysis in the brain source level built from the MEG recordings, which has the potential to improve performance of localisation of EZs.

4.5 Conclusion

The spike automatic detection method developed in this study had varying performance when validated against labels from different readers. The classifier obtained similar performance as inter-rater agreement by neurophysiologists. Thus, this automatic detection method may be useful to assist in localisation of the epileptogenic zone using kurtosis beamforming and enable the spatiotemporal analysis of interictal spikes for focal epilepsy patients.

Chapter 5 Localisation of maximal interictal spike frequency (MISF) in reconstructed source space and its prediction of long-term surgical outcome

5.1 Introduction

Kurtosis beamforming can localise interictal spikes from continuous MEG data, potentially releasing neurophysiologists from time-consuming spike annotations works. The local maxima of kurtosis distributions generated by beamforming are called virtual sensors (VSs), which are considered to be source candidates. It has been widely accepted in practice that visual inspection of VSs that include genuine interictal spikes and artefacts can improve the localisation performance (Agirre-Arrizubieta et al., 2014; de Gooijer-van de Groep et al., 2013; Hall et al., 2018; Kirsch et al., 2006; Oishi et al., 2006; Rose et al., 2013; Tenney et al., 2014). However, each beamforming result can contribute tens of VSs, so visual examination of all the VSs can be as tedious as manual annotation of interictal spikes at the MEG sensor level. It would be beneficial for presurgical evaluation to develop a paradigm that can reduce visual inspection work involved in verification of VSs reconstructed by kurtosis beamforming.

This study has aimed to localise the region that generates interictal spikes, which is considered the epileptic irritative zone. However, the minimum amount of cortex that must be resected to produce seizure freedom is defined as the epileptogenic zone (EZ). It has been shown in previous studies that the irritative zone can be more extensive than the EZ (Bartolomei et al., 2016; Lüders et al., 2006; Plummer et al., 2019; Rosenow & Lüders, 2001). Therefore, it is necessary for us to propose other biomarkers to refine the EZ from the extended irritative zone defined by the brain regions with genuine interictal spikes present using beamforming.

It has been shown in intracranial studies that quantifications of interictal spikes can help localise the EZ in presurgical evaluation. Hufnagel et al. (2000) showed that the earliest spike in a sequence across the brain and the spike with the highest amplitude are good indicators of the EZ. Goncharova et al. (2013) showed that the spatial distribution of the spike rate is associated with the seizure onset zone, which is the area of the cortex that generates clinical seizures. Krendle et al. (2008) showed that absolute spike rate can predict surgical outcome. Conrad et al. (2019) showed that the intracranial electrode with the highest spike frequency can localise the seizure onset zone. Interictal spike propagation across intracranial electrodes has the potential to indicate the region that generates the interictal spikes (Tomlinson et al., 2019b).

It has also been found that quantification of scalp EEG can aid the localisation of the EZ. Coutin-Chruchman et al. (2012) showed that dipole fitting localisation from the spike cluster with the largest quantity of interictal spikes can localize to the surgical resections.

In this study, we proposed a practical and effective paradigm that only required manual review performed on representative transient discharges extracted from the VSs rather than on the continuous VSs. Interictal spike frequencies were calculated across the regions with authentic spikes. The regions with the maximal interictal spikes frequencies (MISF) were validated against the clinical source localisation results and surgical resections. From the validation results, we concluded that MISF can localise to the epileptogenic zone at the brain lobe level. Also, the association of the MISF region and the clinical solutions can predict surgical seizure freedom.

5.2 Methods

5.2.1 Data

Epilepsy patients, MEG data recordings and pre-processing steps used in this chapter were described in Section 2.1 2.2 and 2.3 , respectively. Virtual sensors (VSs) are local maxima of g2-distributions generated by beamforming from MEG recordings. The analysis in this chapter was performed on the VS with the maximal kurtosis value in each segment.

5.2.2 Abnormal discharges detection and cluster

The detections of abnormal discharges were implemented on the first VS (maximal kurtosis) using the amplitude threshold method illustrated in Section 4.2.1.1 Examples of abnormal discharges detection on VS1 in a beamforming segment BF1 are demonstrated in Figure 5-1(a), in which the abnormal discharges are indicated by the dotted lines and corresponding 1 second background data are highlighted by the dashed lines. We clustered all the abnormal discharges detected in one segment by their 1 second background data using Euclidean distance. The morphological clustering and the determination of the optimal number of clusters were introduced in Section 4.2.1.2 We can denote the morphological cluster in each segment as MC_j^i, which represents the jth discharge cluster in segment i. Example of the morphological clusters in all the beamforming segments of one patient are shown in Figure 5-1(b). There are 13 beamforming segments for this patient and the segments were clustered into two groups. The centroid of each cluster and its corresponding MEG sensor data were supplied to a

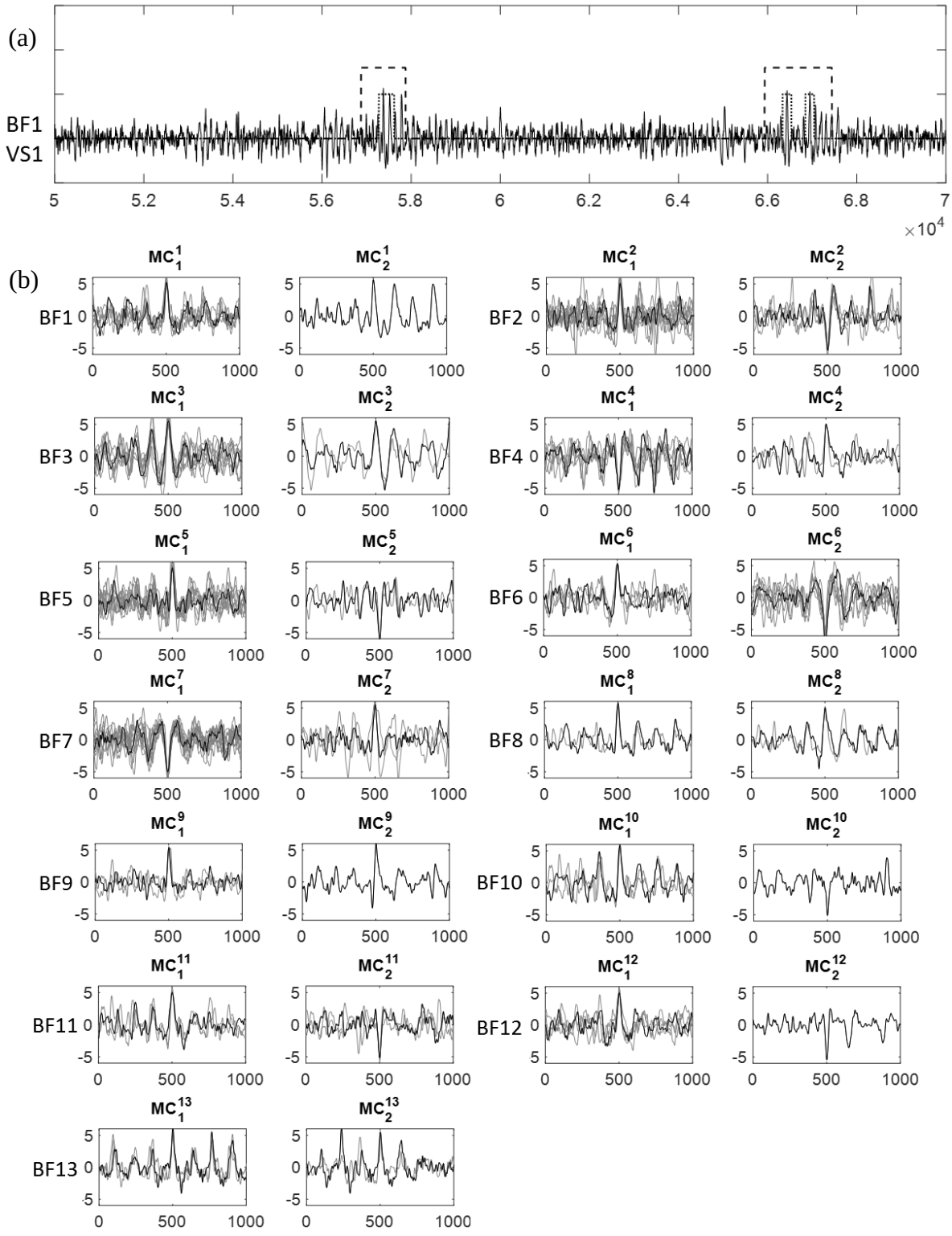

Figure 5-1 Abnormal discharge detection and the morphological clustering . (a) The abnormal discharges were detected on the first VS (VS1) in a beamforming segment BF1. The abnormal discharges detected in this portion are indicated by the dotted line, while the 1 second background data around the detected discharges are highlighted by the dashed line. (b) The morphological clusters on the detected discharges in each beamforming segment of one patient are shown, in which the discharge members of one cluster are shown by the colour grey and their corresponding centroids are shown by the black solid lines. The x-axis in this figure indicates sample numbers.

neurophysiologist (CP), who labelled each centroid as "spike" or "non-spike". The MEG sensor data used was all from the magnetometers.

5.2.3 Interictal spike frequency

We obtained all the morphological clusters across all the segments for one patient. We excluded all the clusters with "non-spike" labels defined by the neurophysiologist. We assume there are M beamforming segments, and in the ith segment we have N_i clusters. Thus, we have

$$\{MC_j^i, i = 1, \cdots, M; j = 1, \cdots, N_i\}. \tag{5.1}$$

The location of $MC_j^i, j = 1, \cdots, N_i$ is the location of VS1 in the ith segment, which is denoted as $\boldsymbol{L}_j^i$. It is worth noting that $\boldsymbol{L}_1^i = \boldsymbol{L}_2^i = \cdots = \boldsymbol{L}_{N_i}^i$. An illustration of spatial distribution of morphological clusters across the brain is shown Figure 5-2(a), in which the big colourful discs represent the VS1 locations across all the beamforming segments and the white dots inside the discs represent various $\boldsymbol{L}_j^i$ in a segment i. The intersecting discs represent that multiple beamforming segment co-localise in the same position with their first VS, such as BF1 and BF2.

We clustered the locations of spike morphological clusters $\boldsymbol{L}_j^i, i = 1, \cdots, M; j = 1, \cdots, N_i$ using the spatial cluster method introduced in Section 4.2.1.2 We cut the hierarchical dendrogram at the height of 1 cm, which indicates that the averaged distances between all pairs of locations in any two clusters was more than 1 cm. We represented the spatial cluster of $\boldsymbol{L}_j^i$ as SC_n, which denotes the nth cluster of this patient, $n = 1, \cdots, n_{sc}$. n_{sc} is number of spatial clusters for a patient. The spatially clustered locations of MC_j^i in Figure 5-2(a) are shown in Figure 5-2(b). Various spatial clusters are represented by different dot colours.

We calculated the interictal spike frequency (ISF_n) in each spatial cluster $SC_n, n = 1, \cdots, n_{sc}$ as

$$ISF_n = \frac{\#spike\ discharges\ in\ SC_n}{\#\ BF\ segments\ in\ SC_n}. \tag{5.2}$$

The numerator of Eq. (5.2) is the number of spike discharges in spatial cluster SC_n, which is the sum of the number of discharges in all the morphological clusters $MC_j^i \in SC_n$. The denominator was used to normalise the spike frequency with the number of beamforming

segments that contributed to the number of spikes in the numerator. For example, the number of segments that contribute to the number of spikes for clusters 1 and 4 in Figure 5-2(b) are 3 and 2, respectively. Based on the parameter ISF_n, $n = 1, \cdots, n_{sc}$, we can obtain the region with the maximal interictal spike frequency (MISF), which is denoted as the MISF region,

$$MISF: \max_{n=n_{MISF}} ISF_n, n = 1, \cdots, n_{sc}. \tag{5.3}$$

For patients with multiple regions with interictal spikes present, we can obtain the region with the MISF, $n = n_{MISF}$. For patients with only one spike localised region $n_{sc} = 1$, the MISF region is this uniquely localised region.

(a)

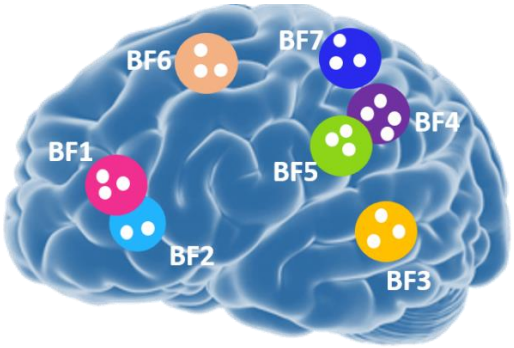

(b)

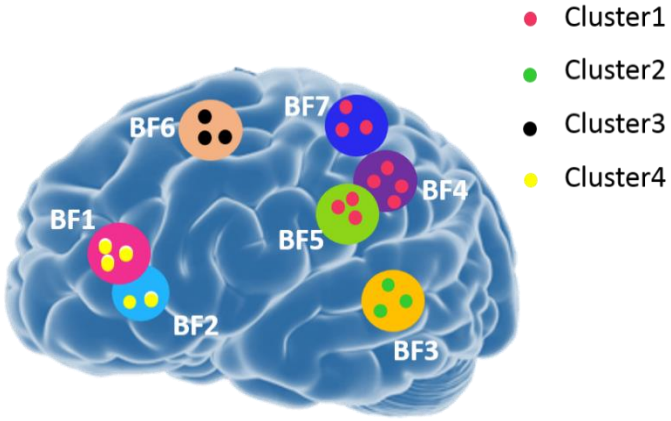

Figure 5-2 Localised morphological clusters in each beamforming segment. (a) (a) The localised first VS in each BF (beamforming) segment is indicated by a big colourful disc, and the corresponding beamforming segment numbers are shown beside the disc. The intersected discs represent VS1 for two segments that were co-localised to the similar positions. The white dots inside the discs demonstrate the discharge clusters in each segment, e.g. there were three morphological clusters obtained from VS1 in segment BF1. (b) The spatially clustered locations of morphological clusters $\boldsymbol{L}_j^i$ are represented by different dot colours. There are four spatial clusters indicated by the magenta, green, black and yellow dots.

5.2.4 Validations

The validations used in this study included the EEG-MEG source localisation performed in clinic, the surgical resections and their surgical outcomes introduced in Section 2.4

The concordance of MISF regions and the clinical solutions were evaluated in terms of overlap, which means the MISF region should be spatially overlapping the clinical solution and should not cover distant or extended regions other than the clinically localised areas. The concordance of MISF regions and the surgical resection was assessed at the overlap scale and at the lobe level. The MISF region was concordant with the surgical resection at the lobe level if they were co-localised to the same lobe. The brain is composed of four lobes: frontal lobe, temporal lobe, parietal lobe and occipital lobe.

Furthermore, we evaluated the prediction of the surgical outcome with the concordance between MISF area and clinical solutions, and the concordance between MISF region and surgical resected areas are the lobe level using sensitivity, specificity, positive predictive value (PPV) and NPF (negative predictive value) calculated from the confusion matrix. The equations of sensitivity, specificity, PPV and NPV can be expressed as

$$\begin{aligned} \text{Sensitivity} &= \frac{\text{TP}}{\text{TP} + \text{FN}} \\ \text{Specificity} &= \frac{\text{TN}}{\text{TN} + \text{FP}} \\ \text{PPV} &= \frac{\text{TP}}{\text{TP} + \text{FP}} \\ \text{NPV} &= \frac{\text{TN}}{\text{TN} + \text{FN}} \end{aligned} \tag{5.4}$$

where TP, FP, TN and FN represent true positive, false positive, true negative and false negative, respectively. The 95% confidence interval for sensitivity and specificity are exact Clopper-Pearson confidence intervals (Clopper & Pearson, 1934). The 95% confidence interval for the PPV and NPV are the standard logit confidence interval (Mercaldo et al., 2007).

The odds ratio (OR) was applied to assess the association of the surgical outcome with the concordance between MISF area and clinical solutions, and the concordance between MISF region and surgical resected areas at the lobe level. The odds ratio quantifies the association between two variables. Two events are independent if and only if OR equals 1; two events are

negatively associated if the OR is less than 1, which means the absence of one event reduces the odds of the other event; two events are positively correlated if the OR is greater than 1, which means the presence of one event increases the odds of the other event.

The distribution of the log odds ratio L is approximately normal with (Morris & Gardner, 1988)

$$L \sim N(log(OR), \sigma^2). \tag{5.5}$$

The standard error of the log odds ratio L is approximately

$$SE[log(OR)] = \sqrt{\frac{1}{a} + \frac{1}{b} + \frac{1}{c} + \frac{1}{d}}, \tag{5.6}$$

where a, b, c and d represent the values of the four elements in the confusion matrix. Because one element of the confusion matrix in our study was zero, for which the odds ratio is not valid, we performed Haldane-Anscombe correction to the confusion matrix by adding 0.5 to each element of the matrix (Lawson, 2004). The 95% confidence interval can be calculated using the logarithm of the OR:

$$CI = exp\{log\ (OR) \pm 1.96 \cdot\ SE[log\ (OR)]\}, \tag{5.7}$$

where $\log(OR)$ is the logarithm of the odds ratio, $\exp\{\cdot\}$ is the natural exponential function, 1.96 is the critical value of the normal distribution with tail area $\alpha = 0.05$. The hypothesis test that the odds ratio equals to 1 can be performed using z-test and the z-statistic is

$$Z = \frac{log\ (OR)}{SE[log(OR)]}. \tag{5.8}$$

If the z-statistic Z is lower 1.96, the hypothesis the odds ratio equals to 1 is valid; Otherwise, the hypothesis is rejected.

5.3 Results

5.3.1 Various regions with interictal spikes present

We clustered the locations with interictal spikes $\boldsymbol{L}_j^i, i = 1, \cdots, M; j = 1, \cdots, N_i$ spatially, and denoted the spatial clusters as $SC_n, n = 1, \cdots, n_{sc}$, where n_{sc} is number of spatial clusters for a patient. The number of spatial clusters with interictal spikes n_{sc} across all the patients in this

study are shown in Table 5-1. The single regions localised by interictal spikes are found in five patients out of the thirteen patients (P007, P035, P040, P042, P072), while eight patients showed multiple regions with interictal spikes (P012, P016, P037, P046, P049, P061, P070). There was one patient without regions revealed by interictal spikes (P074).

5.3.2 Localised regions with various spike frequencies

The four patients with only one spike localised region are shown in Figure 5-3, Figure 5-4, Figure 5-5 and Figure 5-6 for P007, P035, P040 and P042, respectively. In the localisation figures for the four patients, the localised region by the interictal spike is shown in panel (a), in which the colour map registered onto the MRI images is the summed g2 across all the 3 min beamforming segment (see Section 3.7). The validations for each patient are shown in panel (b) including the clinical EEG-MEG source localisation and the surgical resection. In panel (c), the detected discharges in the localised regions are shown, in which all the members of the morphological cluster are shown by the colour grey and the centroid of the cluster is shown by the colour black. In the title of the spike discharge in (c), the beamforming segment with the spikes detected is shown and the number of spikes detected is shown in the brackets.

Table 5-1 Number of spatial spike clusters for all the patients. The first column shows the patient and the second column give the corresponding n_{sc}.

Patient	n_{sc}
P007	1
P012	4
P016	2
P035	1
P037	4
P040	1
P042	1
P046	4
P049	3
P061	2
P070	3
P072	1
P074	None

The spike localised region for P007 shown in Figure 5-3(a) is the right mesial temporal lobe, which was concordant with one side of the clinical localisation. It is worth noting that the spike localised regions are validated against the clinical solutions at the overlapping level. The localised spike region for patient P007 was not concordant with the surgical resection at both overlapping and lobe level. The surgical outcome of this patient was not seizure-free.

The spike localised region for P035 are shown in Figure 5-4(a) is the sylvian fissure, which is concordant with the propagation of the clinical localisation shown in (b) as a pink disc with number 4. The spike localised region was not concordant with the surgical resection in the overlapping level, while it was concordant with the surgical cavity at the lobe level. This patient obtained seizure-free surgical outcome.

For P040, the localised region is the right posterior temporal lobe shown in Figure 5-5(a), which was concordant with the clinical onset illustrated in (b) as the pink disc with number 1. The spike localised region was not concordant with the surgical resection at the overlapping level, but concordant at the lobe level that both located at the temporal lobe. This patient did not achieve seizure-free surgical outcome.

The single localised region with spikes for P042 is the left inferior temporal lobe shown in Figure 5-6(a), which was concordant with the clinical propagation and the surgical resection at both overlap and lobe level. This patient did obtain the seizure freedom after surgery.

For P072, the single spike localised region was right posterior inferior frontal gyrus (Figure 5-7), which was concordant with the clinical onset indicated as the pink disc with number 1 in (b), and it was concordant with the surgical resection in both the overlap and lobe level. This patient obtained post-surgical seizure freedom.

Patient P007

(a)

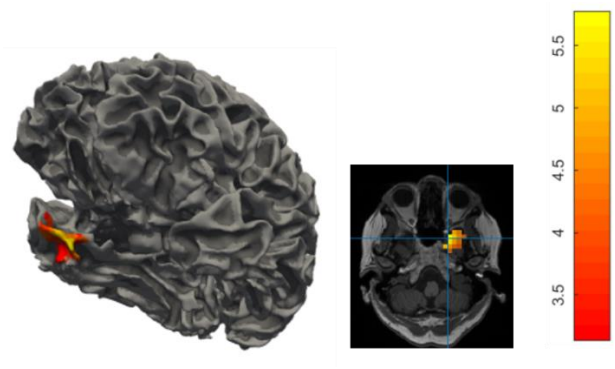

(b)

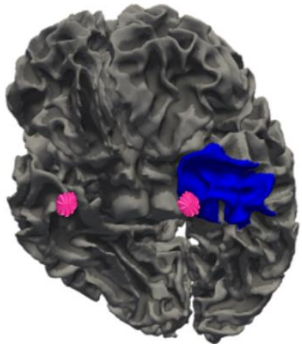

(c)

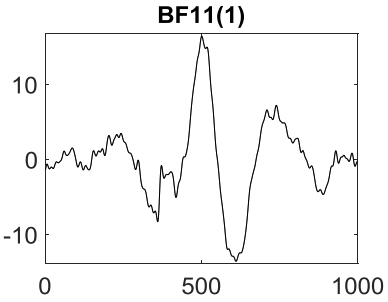

Figure 5-3 The spike localised region for patient P007 . The single spike localised region is the right mesial temporal lobe shown in (a). The validations shown in (b) include surgical resection indicated by the blue mesh and the clinical EEG-MEG source localisation (EMSL) shown by pink discs. The reconstructed interictal spike waveform is shown in (c), which was detected in beamforming segment 11, and the number of detected spikes is shown in the brackets, which was only one. The detected spike waveform shown in (c) is 1 second of data with sampling rate 1000 Hz; the x-axis is sample numbers of the waveform.

Patient P035

(a) (b)

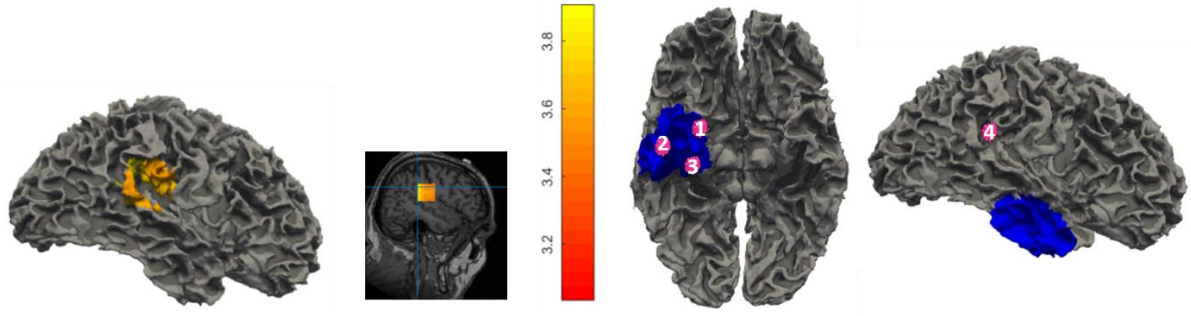

(c)

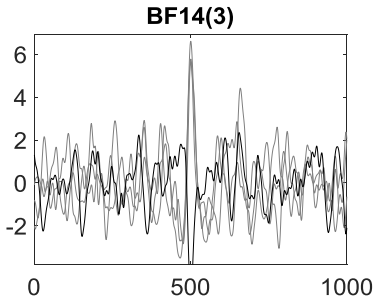

Figure 5-4 The spike localised region for patient P035 . Interictal spikes were detected in only one region shown in (a), which is the sylvian fissure. The validations for this patient are shown in (b), in which the surgical cavity is indicated by the blue mesh and the clinical EMSL results are shown by the pink discs with spike onset and propagations indicated by numbers 1 - 4, indicating the temporal progression. (c) Three spikes detected in the localised region from beamforming segment 14 are shown with 1 second data sampled at 1000Hz.

Patient P040

(a) (b)

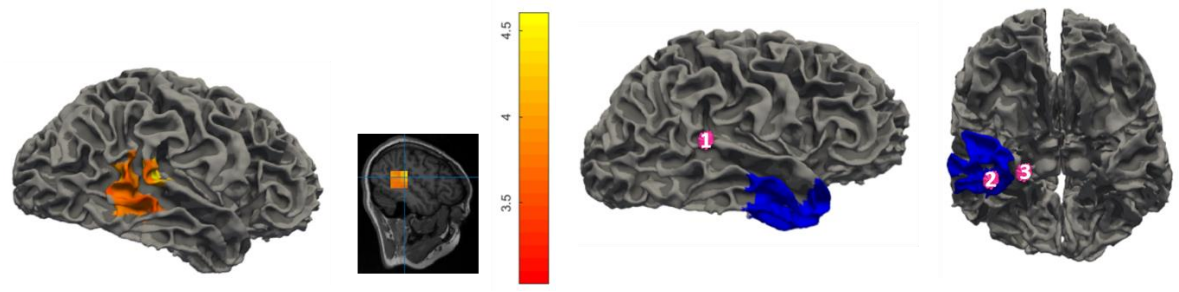

(c)

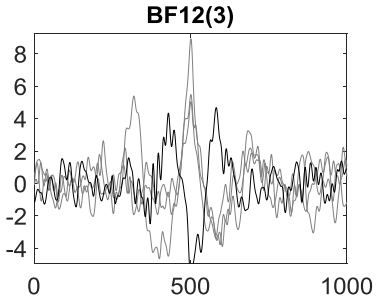

Figure 5-5 The spike localised region for patient P040 . Interictal spikes were detected in only one region shown in (a), which is the right posterior temporal lobe. The validations for this patient are shown in (b), in which the surgical cavity is indicated by the blue mesh and the clinical EMSL results are shown as pink discs with spike onset and propagations indicated by numbers 1 - 3. (c) Three spikes detected in the localised region from beamforming segment 12 are shown with 1 second data sampled at 1000Hz.

Patient P042

(a) (b)

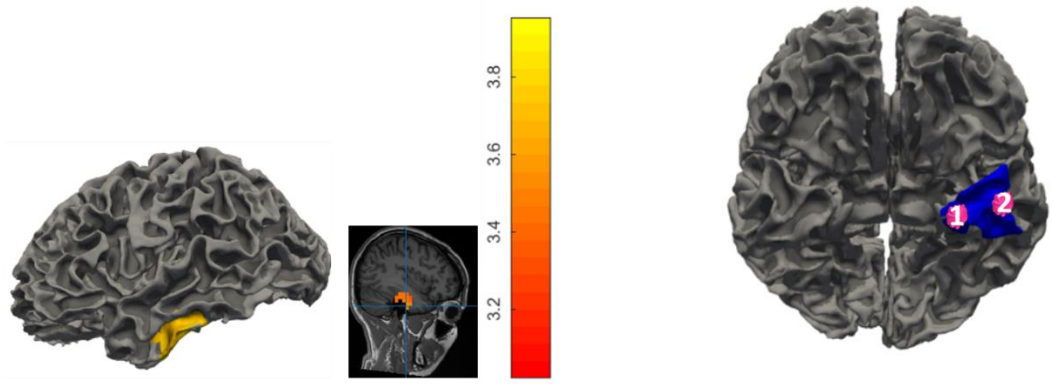

(c)

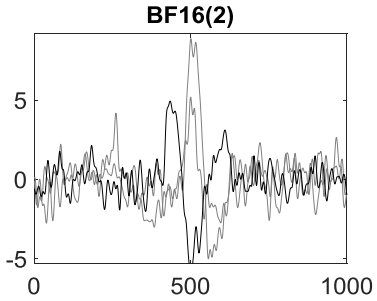

Figure 5-6 The spike localised region for patient P042 . Interictal spikes were detected in only one region shown in (a), which is the left inferior temporal lobe. The validations for this patient are shown in (b), in which the surgical cavity is indicated by the blue mesh and the clinical EMSL results are shown as pink discs with spike onset and propagations indicated by numbers 1 - 2. (c) Two spikes detected in the localised region from beamforming segment 16 are shown with 1 second data sampled at 1000Hz.

Patient P072

(a) (b)

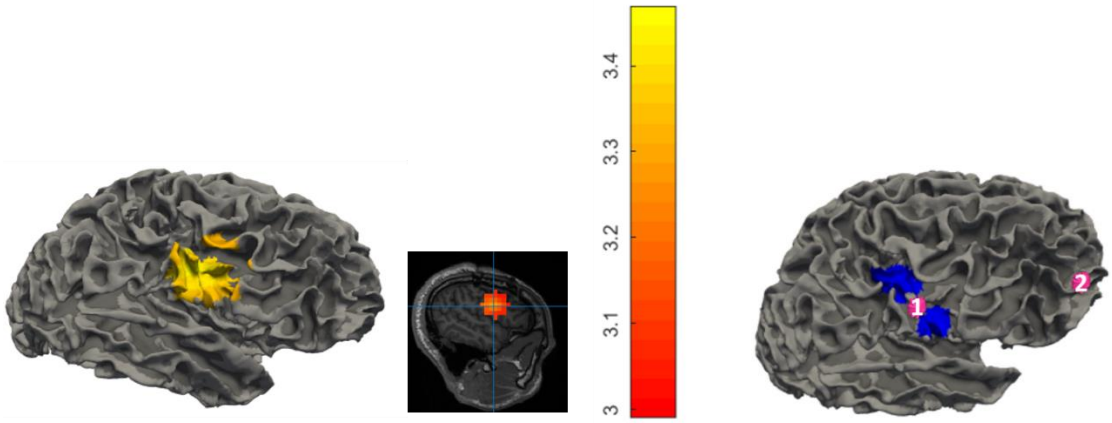

(c)

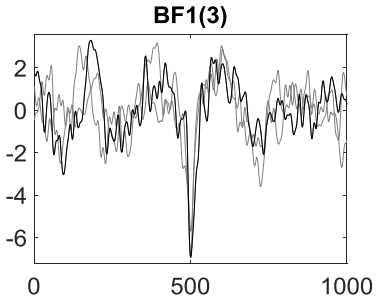

Figure 5-7 The spike localised region for patient P072 . Interictal spikes were detected in only one region shown in (a), which is right posterior inferior frontal gyrus. The validations for this patient are shown in (b), in which the surgical cavity is indicated by the blue mesh and the clinical EMSL results are shown as pink discs with spike onset and propagations indicated by number 1 - 2. (c) Three spikes detected in the MISF region from beamforming segment 1 are shown with 1 second data sampled at 1000Hz.

Multiple localised regions of spikes are shown for eight patients (see Figure 5-8 to Figure 5-14). There are four panels in each figure. In panel (a), the various regions localised by spikes are shown and ranked by the normalised frequencies in the descending order. Each region is indicated by its spike frequency rank, which is a number in a circle. The MISF regions is the region labelled by ①. The colour map registered onto the MRI images in panel (a) is the summed kurtosis across all the MEG beamforming segments and averaged by the number of segments, see Eq. (3.7). The normalised spike frequencies across various regions are shown in panel (b), where the x-axis represents the spike frequency rank of each region and the y-axis is the corresponding spike frequency. In the normalised spike frequency figure, a point with value zero was added to the end of the curve as a reference. The validations including the clinical source localisation and the surgical resections are shown in panel (c) as pink discs and a blue mesh. The morphologically clustered detected spikes in each localised region are shown in panel (d). The spikes in a cluster are depicted as the grey lines and the centroid of each cluster is depicted as a black line.

The spike localised regions for P012 are shown in Figure 5-8(a) with normalised spike frequencies 5.67, 5.33, 3.00 and 2.00, shown in Figure 5-8(b). The morphologically clustered spikes for all four regions are shown in Figure 5-8(d). As can be seen from (d), the numbers of detected interictal spikes across three beamforming segments BF6, BF9 and BF13 were 10, 2 and 5, respectively. Thus, the normalised spike frequency for region 1 was 17/3=5.67. Region 1 with the maximal spike frequency is the MISF region, which was co-localised to clinical propagation as well as the surgical resection in the same lobe. This patient obtained seizure-free surgical outcome. The spike frequency in region 2 was very close to the spike frequency in region 1, and the locations of regions 2 and 1 were very close, but region 2 was anterior to the region 1. The spike frequencies in regions 3 and 4 were considerably less than regions 1 and 2, and the locations of regions 3 and 4 were distant from regions 1 and 2 located at the left occipital lobe and the right post-central gyrus, respectively.

For Patient P016 (see Figure 5-9), region 1 was dominant with spike rate 18, and located in the left posterior inferior frontal gyrus, which was concordant with clinical propagation and the surgical resection with overlapping accuracy shown in (c). This patient achieved seizure freedom after surgery. Another localised region with spike rate 3 was located very close to region 1, but more inferior to region 1.

Four spike localised regions present for patient P037 are shown in Figure 5-10. The MISF region (region 1, located at the base precentral gyrus) had a much higher spike rate than the remaining regions located at the temporal lobe. The MISF region of P037 was concordant with the clinical onset and propagation, and it was overlapping with the surgical resection. This patient obtained post-surgical seizure freedom.

The localised MISF region for P046 (see Figure 5-11) had significantly higher spike rate (15) than the spike rates in the other regions (5, 4, 1), but the MISF region was not concordant with any validations. This patient failed to achieve seizure-free surgical outcome.

For patient P049 (see Figure 5-12), regions 2a and 2b had the same spike frequency (1). The MISF region was localised to the left anterior temporal lobe, but it was not concordant with any validations. This patient did not obtain seizure-free surgical outcome.

There were two regions localised by the interictal spikes for patient P061 (see Figure 5-13) with very similar frequencies 15.71 and 14.00. Also, the localised two regions were located very closely to each other at the right inferior frontal lobe. The MISF region was located at the right inferior frontal gyrus, which was concordant with surgical resection (both overlapping and lobe level) and the onset of clinical solution depicted as the pink disc with the number 1 in Figure 5-13(c). This patient achieved seizure freedom after surgery.

For patient P070 (see Figure 5-14), the MISF region was localised to the left superior temporal lobe with spike rate 5. The MISF region was co-localised with the clinical onset indicated as the pink disc with number 2 shown in (c), and it was co-localised with the surgical resection at the left temporal lobe. The remaining two regions 2a and 2b had the same spike rate 2, which localised to the left posterior inferior temporal lobe and right occipital lobe, respectively.

Patient P012

(a)

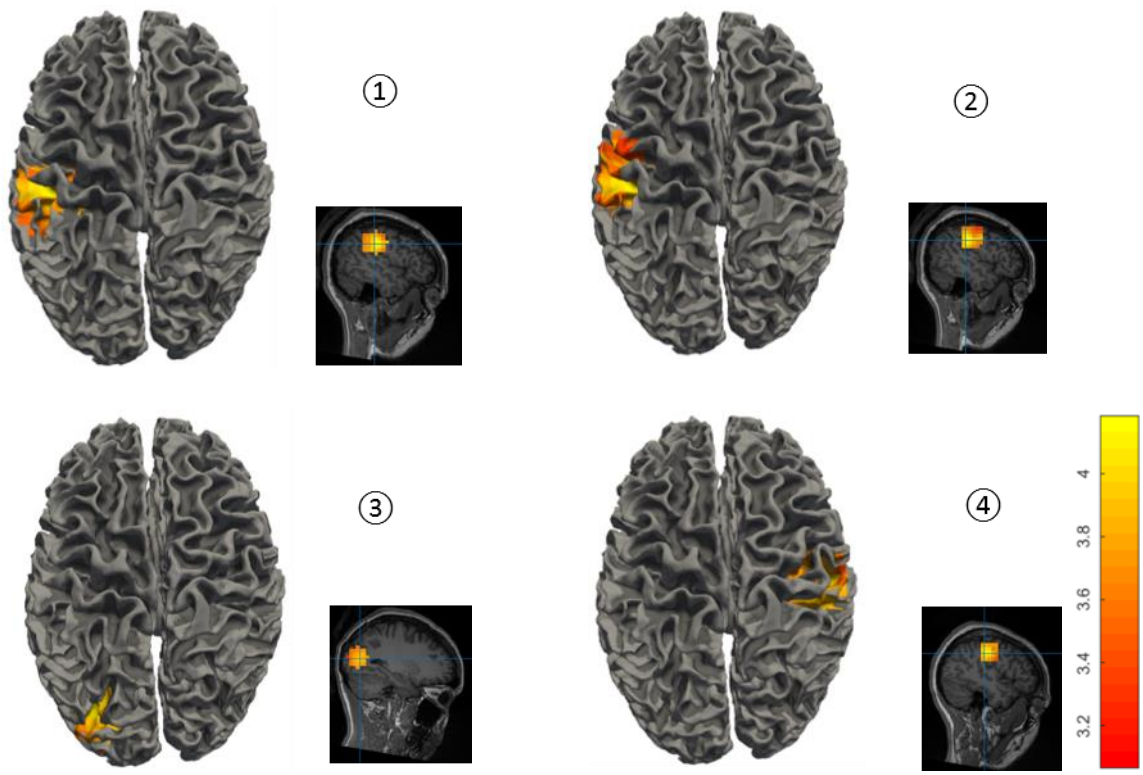

(b)

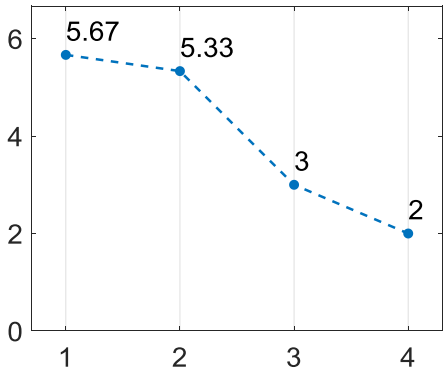

(c)

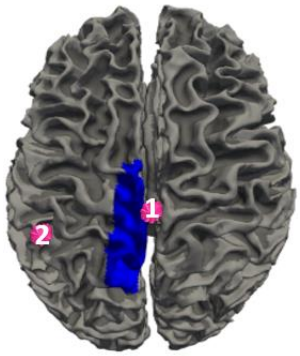

(d)

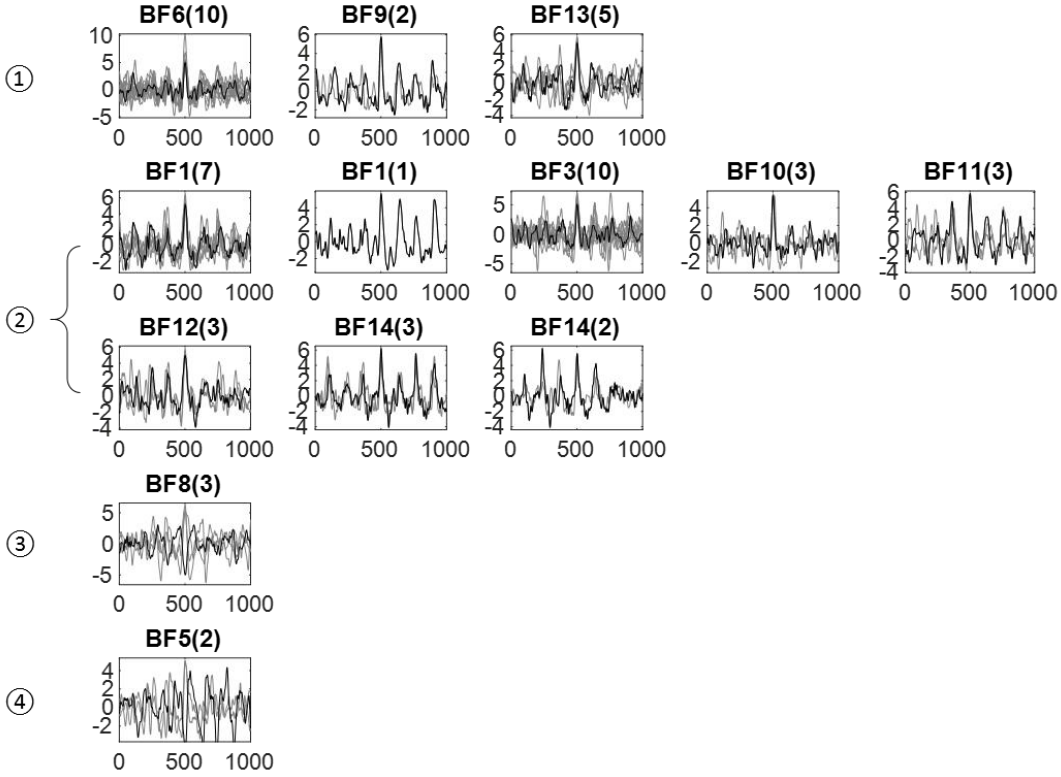

Figure 5-8 The spike localised regions for patient P012. Interictal spikes were detected in four diverse regions shown in (a) and they are arranged in descending order of the spike frequencies shown in (b). The MISF region is shown in (a)①, which is the left parietal convexity. The validations for this patient are shown in (c), in which the surgical cavity is indicated by the blue mesh and the clinical EMSL results are shown as pink discs with spike onset and propagation indicated by numbers 1 - 2, indicating the progression sequence. (d) The reconstructed spikes across four regions are shown; the length of the data shown is 1 second at 1000 Hz sampling rate.

Patient P016

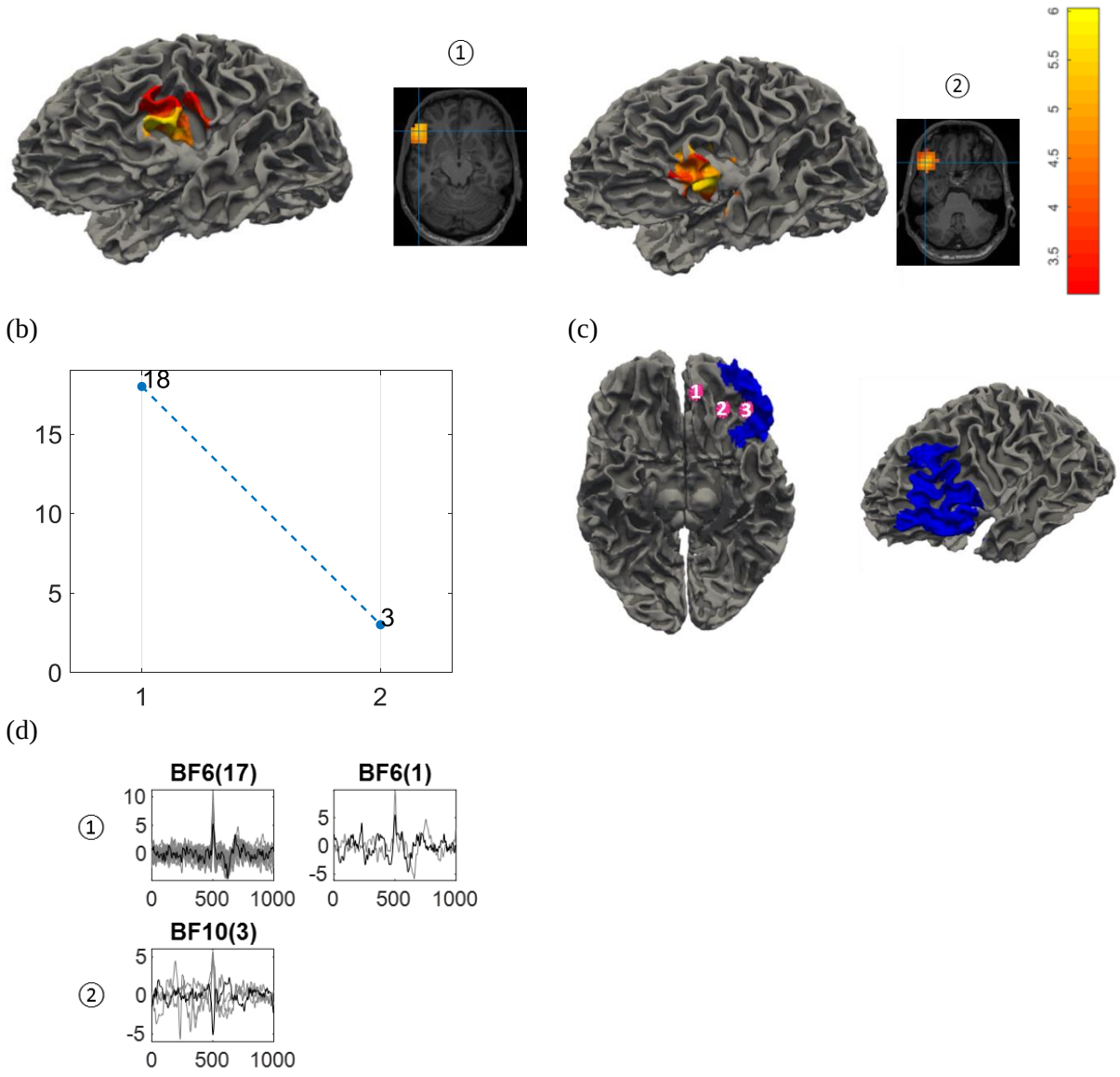

Figure 5-9 The spike localised regions for patient P016. Interictal spikes were detected in two diverse regions shown in (a) and they are arranged in descending order of spike frequencies shown in (b). The MISF region is shown in (a)①, which is the posterior inferior frontal gyrus. The validations for this patient are shown in (c), in which the surgical cavity is indicated by the blue mesh and the clinical EMSL results are shown as pink discs with spike onset and propagations indicated by numbers 1 - 3, indicating the progression sequence. (d) The reconstructed spikes across two regions are shown; the length of the data shown is 1 second at 1000 Hz sampling rate.

Patient P037

(a)

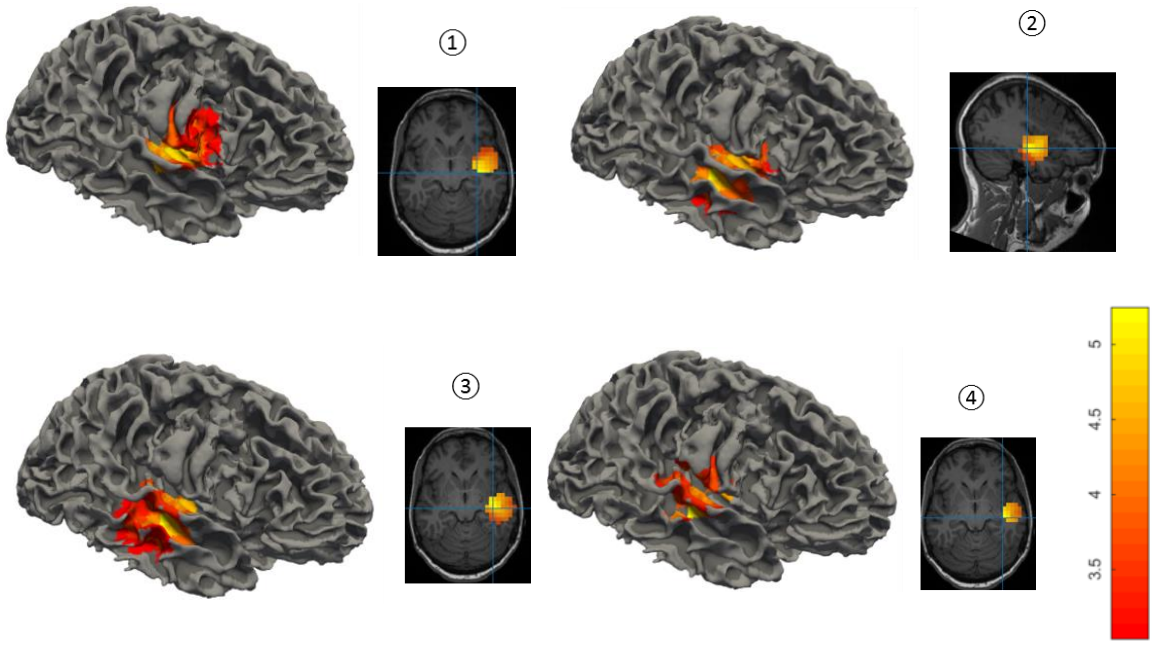

(b)

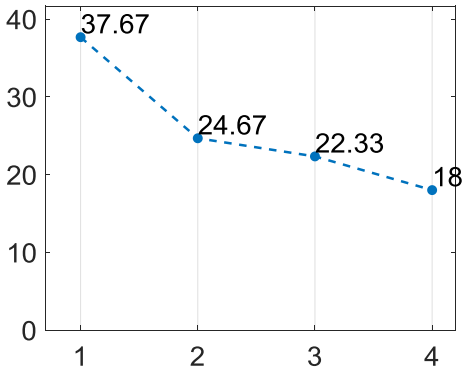

(c)

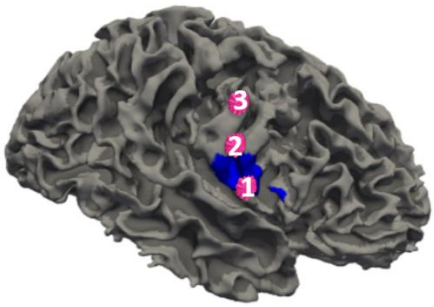

(d)

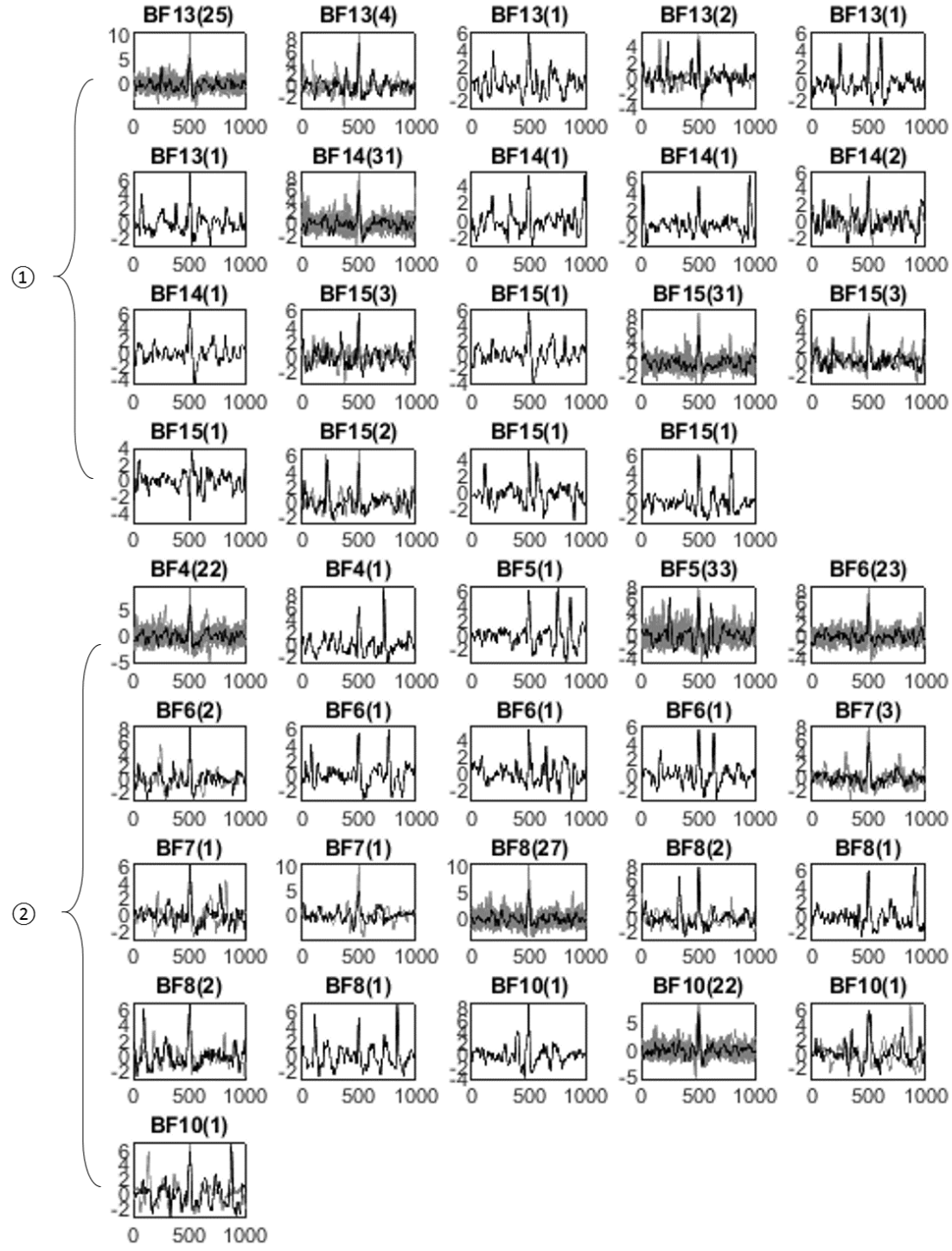
BF13(25)
BF13(4)
BF13(1)
BF13(2)
BF13(1)
BF13(1)
BF14(31)
BF14(1)
BF14(1)
BF14(2)
BF14(1)
BF15(3)
BF15(1)
BF15(31)
BF15(3)
BF15(1)
BF15(2)
BF15(1)
BF15(1)
BF4(22)
BF4(1)
BF5(1)
BF5(33)
BF6(23)
BF6(2)
BF6(1)
BF6(1)
BF6(1)
BF7(3)
BF7(1)
BF7(1)
BF8(27)
BF8(2)
BF8(1)
BF8(2)
BF8(1)
BF10(1)
BF10(22)
BF10(1)
BF10(1)
①
②

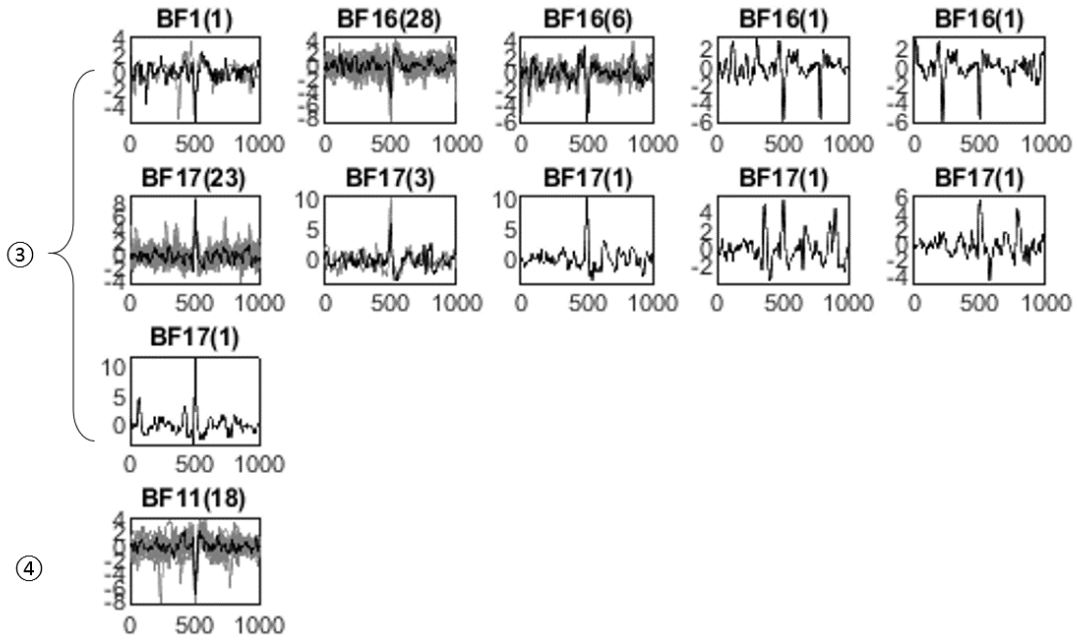

Figure 5-10 The spike localised regions for patient P037. Interictal spikes were detected in four diverse regions shown in (a) and they are arranged in descending order of spike frequencies shown in (b). The MISF region is shown in (a)①, which is the base precentral gyrus. The validations for this patient are shown in (c), in which the surgical cavity is indicated by the blue mesh and the clinical EMSL results are shown as pink discs with spike onset and propagations indicated by numbers 1 - 3, indicating the progression sequence. (d) The reconstructed spikes across four regions are shown; the length of the data shown is 1 second at 1000 Hz sampling rate.

Patient P046

(a)

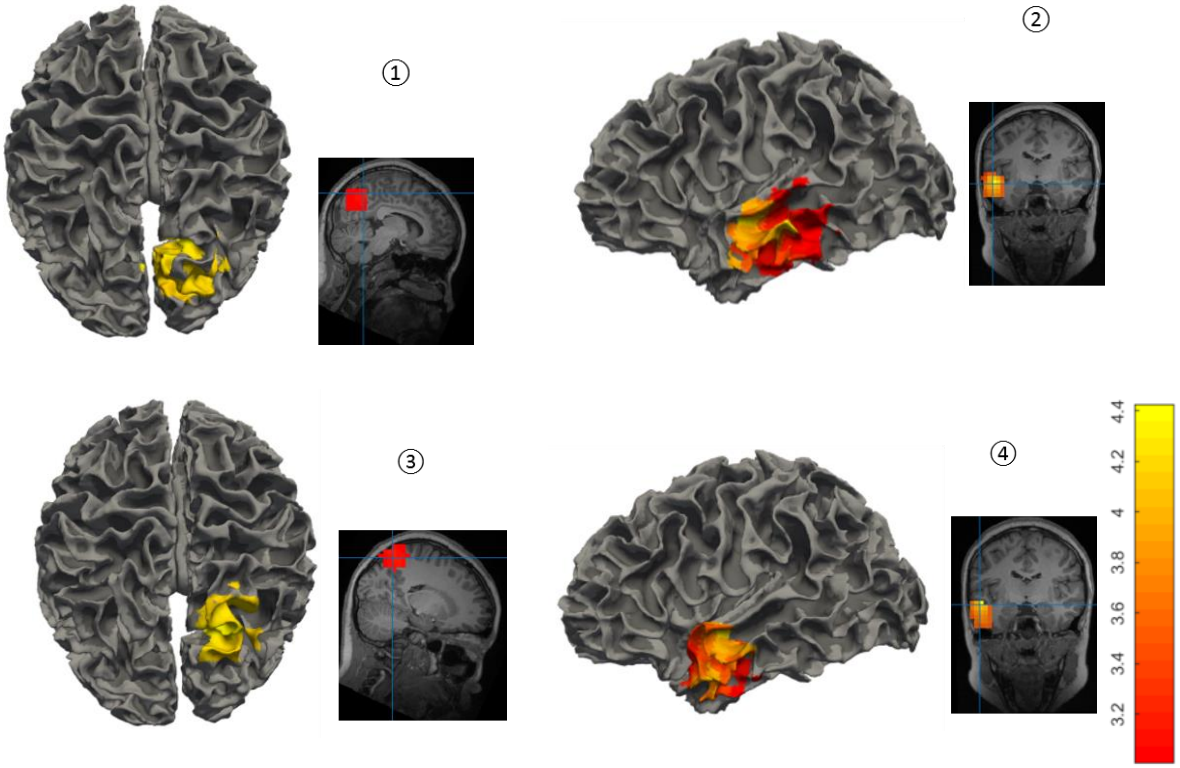

(b)

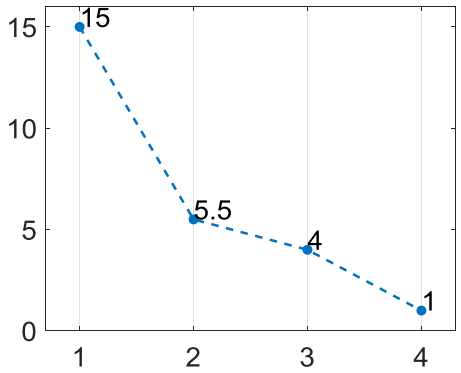

(c)

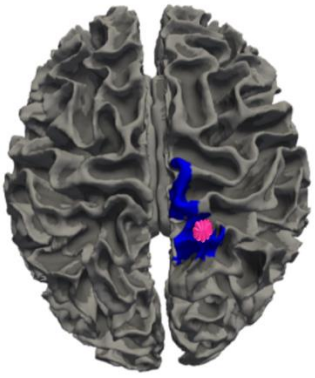

(d)

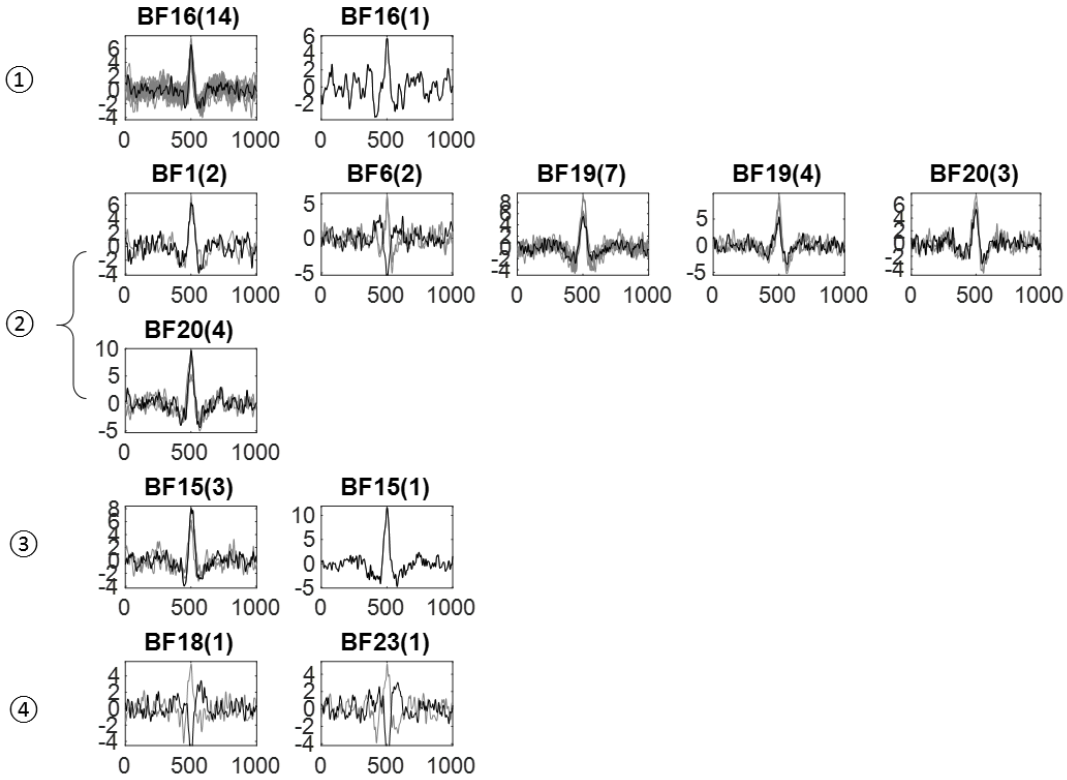

Figure 5-11 The spike localised regions for patient P046. Interictal spikes were detected in four diverse regions shown in (a) and they are arranged in descending order of the spike frequencies shown in (b). The MISF region is shown in (a)①, which is the superior occipital gyrus. The validations for this patient are shown in (c), in which the surgical cavity is indicated by the blue mesh and the clinical EMSL results are shown with pink discs. (d) The reconstructed spikes across four regions are shown; the length of the data shown is 1 second at 1000 Hz sampling rate.

Patient P049

(a)

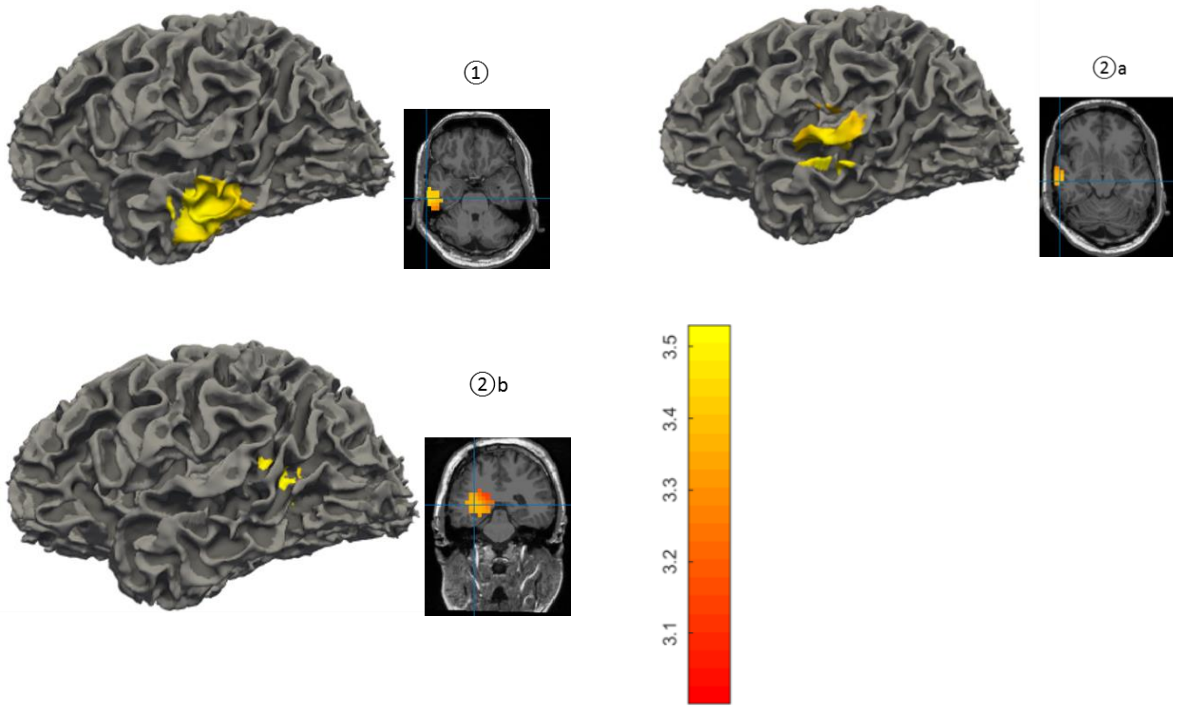

(b)

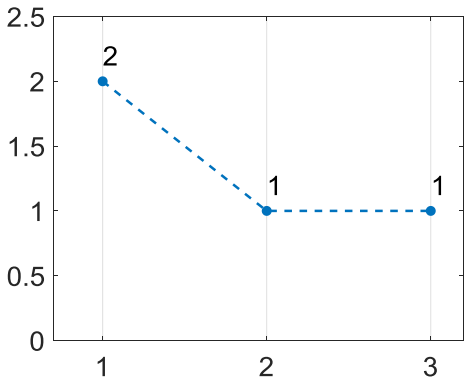

(c)

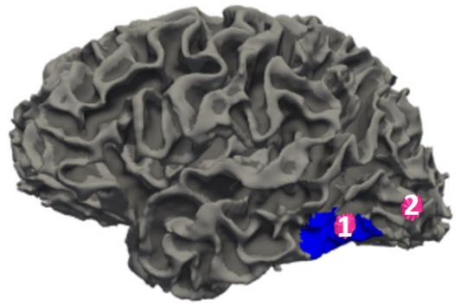

(d)

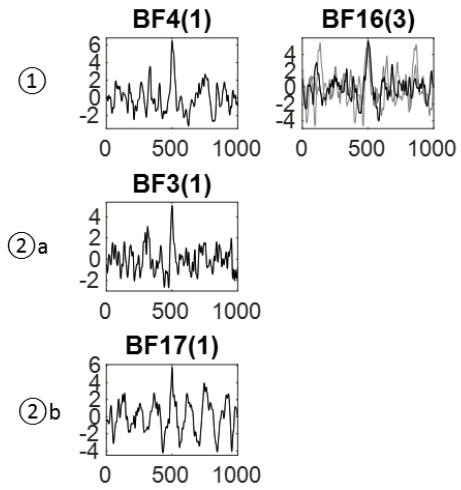

Figure 5-12 The spike localised regions for patient P049.Interictal spikes were detected in three diverse regions shown in (a) and they are arranged in descending order of the spike frequencies shown in (b). The MISF region is shown in (a)①, which is the left anterior temporal lobe. The validations for this patient are shown in (c), in which the surgical cavity is indicated by the blue mesh and the clinical EMSL results are shown with pink discs with spike onset and propagations indicated by number 1 - 2, indicating the progression sequence. (d) The reconstructed spikes across three regions are shown; the length of the data shown is 1 second at 1000 Hz sampling rate.

Patient P061

(a)

1

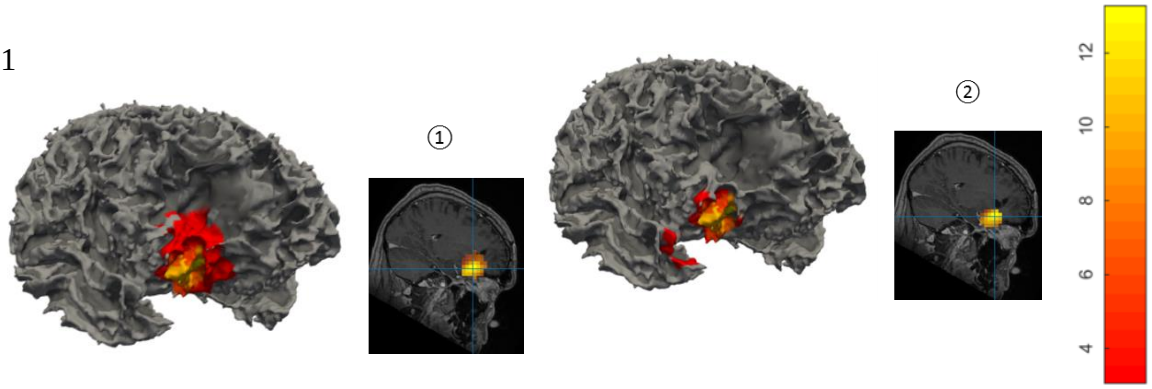

(b)

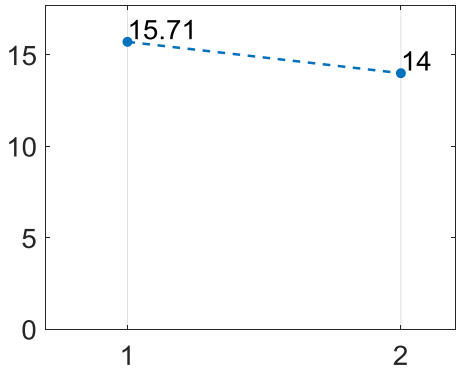

(c)

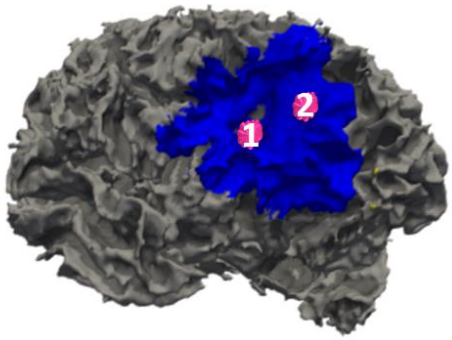

(d)

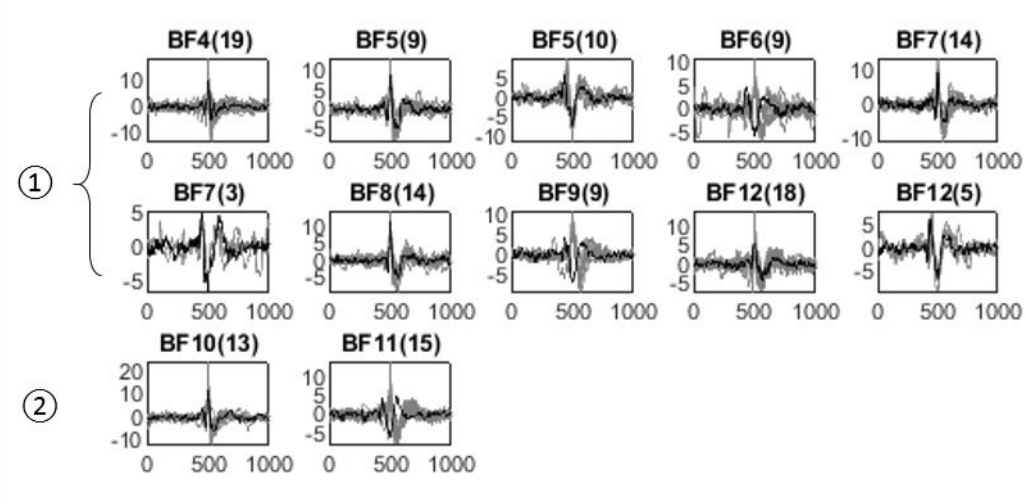

Figure 5-13 The spike localised regions for patient P061. Interictal spikes were detected in three diverse regions shown in (a) and they are arranged in descending order of the spike frequencies shown in (b). The MISF region is shown in (a)①, which is the right inferior frontal gyrus. The validations for this patient are shown in (c), in which the surgical cavity is indicated by the blue mesh and the clinical EMSL results are shown as pink discs with spike onset and propagations indicated by number 1 - 2, indicating the progression sequence. (d) The reconstructed spikes across two regions are shown; the length of the data shown is 1 second at 1000 Hz sampling rate.

Patient P070

(a)

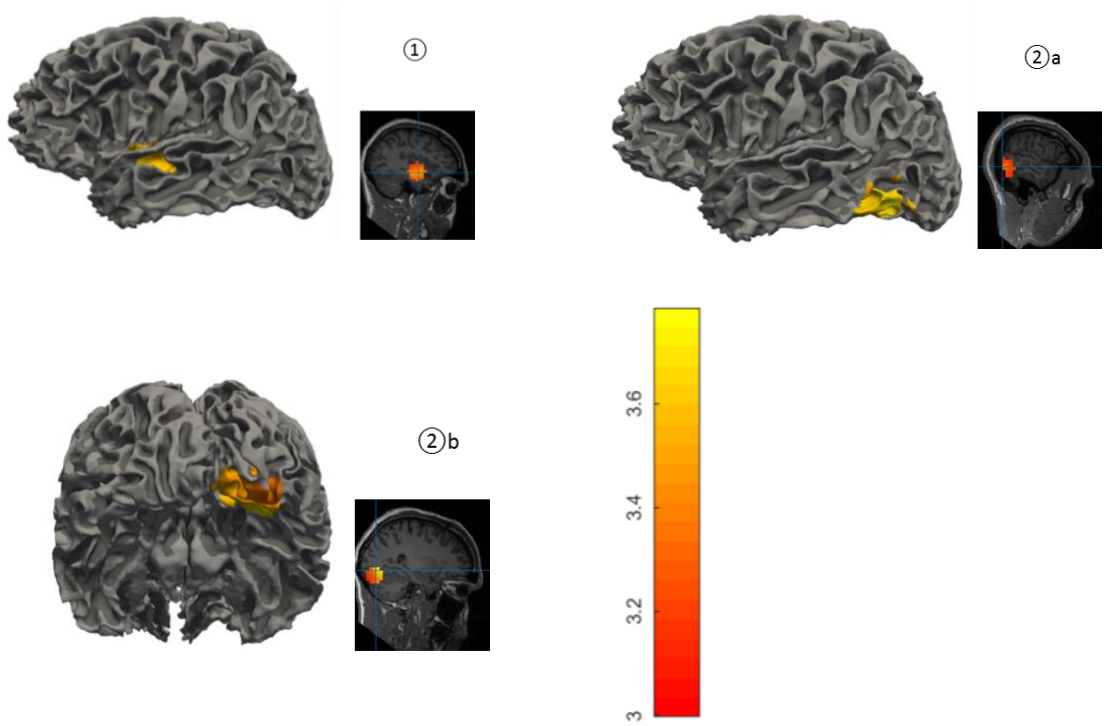

(b)

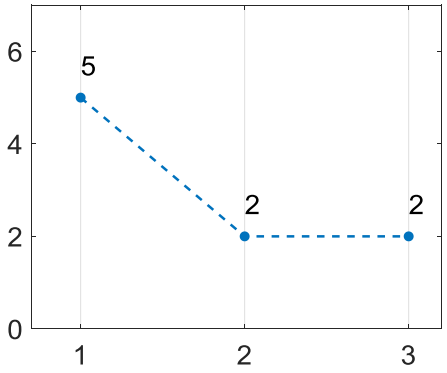

(c)

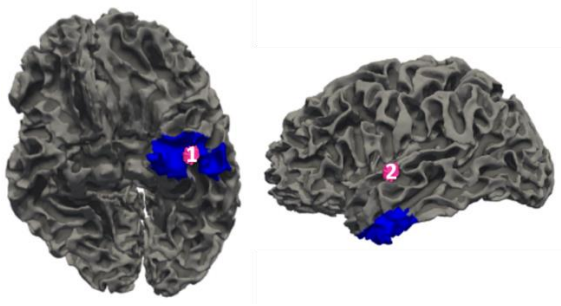

(d)

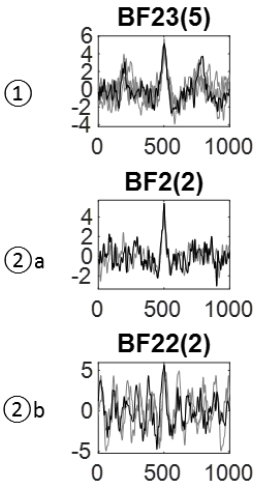

Figure 5-14 The spike localised regions for patient P070. Interictal spikes were detected in three diverse regions shown in (a) and they are arranged in descending order of the spike frequencies shown in (b). The MISF region is shown in (a)①, which is left superior temporal gyrus. The validations for this patient are shown in (c), in which the surgical cavity is indicated by the blue mesh and the clinical EMSL results are shown as pink discs with spike onset and propagation indicated by numbers 1 - 2, indicating the progression sequence. (d) The reconstructed spikes across three regions are shown; the length of the data shown is 1 second at 1000 Hz sampling rate.

5.3.3 Associating the maximal interictal spike frequency (MISF) region with the clinical source localisations and surgical outcome prediction

We validated the MISF region against clinical source localisations. As introduced in section 5.2.4 validations against the clinical solutions were performed on the overlap level. The summarised validations are shown in Table 5-2. We did not reveal any interictal spikes for patient P074. Thus, this patient is not included in the following analysis. For patients with single spike localised regions, we consider these single regions as the MISF regions for the following analysis.

We obtained concordance between MISF and clinical onset in two patients (P037 and P072) and obtained partial concordance in one patient (P007). We observed concordance between the MISF and the clinical solution (including both onset and propagation) in eight out of nine seizure-free patients. We categorise patient P007 as discordant with the clinical solution and obtained non-seizure-free surgical outcome, since the patient had bilateral temporal lobe epilepsy with only the left temporal lobe resected and with the MISF localised on the other side. Thus, we conclude that discordances between the MISF regions and the clinical solutions were obtained in three (P007, P046, P049) out of four non-seizure-free patients.

The confusion matrix of the concordance between MISF and the clinical solutions validated against seizure-free and non-seizure-free patients is shown in Table 5-3. The sensitivity, specificity, positive predictive value and negative predictive value generated from the confusion matrix in Table 5-3 are 100%, 75%, 88.89% and 100%, respectively, shown in Table 5-4. The results indicate that the concordance between MISF and the clinical solutions can predict seizure-free or non-seizure-free surgical outcome.

The odds ratio generated from the confusion matrix in Table 5-3 was 39.67 with 95% confidence interval [1.28, 1229.87], which is much greater than 1 and indicates that the concordances between MISF regions and the clinical solutions were highly associated with seizure-free surgical outcome.

Table 5-2 Validation of MISF region against clinical source localisation and surgical resection. The first column shows the patient included in this study (excluding P074). The following two columns show the concordance between the MISF region with the clinical results with 'Con', 'Dis' and 'Partially-con'. The last column gives the surgical outcomes for all the patient. There was no interictal spikes revealed in P074, thus the concordance for this patient were shown by '-'. The 'Partially-con' and 'Con' validation results are highlighted by the colour blue in the table.

Patients	MISF region		Surgical outcome
	Clinical O	Clinical P	
P007	Partially-con	-	Non-free
P012	Dis	Con	free
P016	Dis	Con	free
P035	Dis	Con	free
P037	Con	Dis	free
P040	Dis	Con	Non-free
P042	Dis	Con	free
P046	Dis	-	Non-free
P049	Dis	Dis	Non-free
P061	Dis	Con	free
P070	Dis	Con	free
P072	Con	Dis	free

'Clinical O': clinical onset;
'Clinical P': clinical propagation;
'SR': surgical resection;
'Con': the concordant validations between MISF regions and clinical onsets or the clinical propagations;
'Dis': the discordant validations between MISF regions and clinical onsets or the clinical propagations;
'Partially-con': the MISF region localised to a part of clinically localised areas. For patient P007, the MISF region localised to the right mesial temporal lobe, while the clinical source localisation showed bilateral temporal lobe. Thus, the "Partially-con" was used for this patient.

Table 5-3 Confusion matrix of concordance between MISF regions and the clinical solutions grouped by the surgical outcomes.

Surgical outcome	Seizure-free	Non-seizure-free
Concordance	8	1
Non-concordance	0	3

Table 5-4 Performance of the concordance of the MISF regions and surgical cavities for the surgical outcome predictions obtained from Table 2. The 95% confidence intervals are shown in the brackets. PPV=positive predictive value; NPV=negative predictive value.

Surgical outcome prediction	
Sensitivity	100% (63.06% to 100.00%)
Specificity	75% (19.41% to 99.37%)
PPV	88.89% (59.44% to 97.76%)
NPV	100%
Odd ratio	39.67(1.28 to 1229.87)

5.3.4 Associating the maximal interictal spike frequency (MISF) region with the surgical resection and its surgical outcome prediction

In this section, we validated the MISF region against the surgical resections. As introduced in section 5.2.4 the validation performed against the surgical resection was performed at both the overlap level and the lobe level. The summarised validations are shown in Table 5-5. The MISF regions were co-localised with surgical resection in terms of overlap in five patients (P016, P037, P042, P061, P072) and all five patients obtained seizure-free surgical outcome. The concordant validations between the MISF regions and the surgical resections in the brain lobe level were present in nine out of twelve patients.

We categorised patients that obtained lobe level co-localisation between the MISF regions and the surgical resection into seizure-free and non-seizure-free groups and generated the confusion matrix in Table 5-6. The confusion matrix is the same as the confusion matrix generated from

the concordance between the MISF region and the clinical solutions given in Table 5-3. Thus, the prediction and association of surgical outcome using the concordance of the MISF region and the surgical resection in the lobe scale are the same as the sensitivity, specificity, PPV, NPV and odds ratio given by the Table 5-4. The sensitivity and specificity are 100% and 75%, and the odds ratio is 39.67, which is much greater than 1. Therefore, we can conclude that the MISF can localise to the epileptogenic zone at the lobe level, which can lead to seizure freedom.

Table 5-5 Concordance between the MISF regions and surgically resected areas. The table lists the concordance in terms of "overlap" and "lobe" levels in the second column. The surgical outcomes are listed in the third column. "N" indicates that the MISF area and the surgical cavity were not concordant; "Y" indicates they were consistent. "Free" indicates the patient obtained Engel I surgical outcome; "Not free" indicates the surgical outcome was categorised as Engel II - IV.

Patients	Surgical resection (overlap/lobe)	Surgery outcome
P007	N / N	Not free
P012	N / Y	Free
P016	Y / Y	Free
P035	N / Y	Free
P037	Y / Y	Free
P040	N / Y	Not free
P042	Y / Y	Free
P046	N / N	Not free
P049	N / N	Not free
P061	Y / Y	Free
P070	N / Y	Free
P072	Y / Y	Free

Table 5-6 Confusion matrix of concordances between MISF regions and surgical cavities classified by surgical outcomes.

Surgical outcome	Free	Not free
Concordance	8	1
Non-concordance	0	3

5.3.5 Comparison between localised MISF regions and clinically localised onset regions

We compared the localisation performance of MISF regions and clinically localised onset regions (Plummer et al., 2019) validated against surgical resections at the overlap level. Because the MISF region only revealed interictal spikes in 12 out of 13 patients, the comparison was performed in the 12 patients with localised spikes. The comparisons of performance are shown in Table 5-7. The performance scores were obtained using the following rules:

Score = 1: if the patient had seizure-free surgical outcome, the method localised to the surgical cavity, or if the patient had non-seizure-free surgical outcome, the method localised to a location other than the surgical resection.

Score = 0: if the patient had seizure-free surgical outcome, the method localised to locations other than the surgical resection, or if the patient had non-seizure-free surgical outcome, the method localised to the surgical cavity.

Score = 0.5: this score was given to the MISF region of patient P007, because the MISF localised to one side of the bilateral temporal lobe epilepsy.

For five of the 12 patients, both the MISF method and the clinical onset method scored 1. For the other seven patients, either the MISF method or the clinical onset method scored 1 but not both.

We can see from the last row of Table 5-7 that the total calculated score for the MISF method was 8.5, while the score for the clinical onset was 9. We can conclude that the localisation performances of the MISF method and the clinical onset method were comparable.

Table 5-7 Comparison of localisation performance between MISF regions and onset regions clinically validated against surgical resections. The first column gives the patient number for 12 patients. The following two columns show the performance scores for the two localisation methods: localised MISF region and clinical onset region. The last column gives the surgical outcome of each patient. The last row shows the total score across 12 patients.

Patients	MISF	Clinical onset	Surgery outcome
P007	0.5	1	Not free
P012	0	1	Free
P016	1	0	Free
P035	0	1	Free
P037	1	1	Free
P040	1	1	Not free
P042	1	1	Free
P046	1	0	Not free
P049	1	0	Not free
P061	1	1	Free
P070	0	1	Free
P072	1	1	Free
Total	**8.5**	**9**	-

5.4 Discussion

This study proposed a method to reduce the visual inspection required for post-processing procedures of kurtosis beamforming. Continuous virtual sensor data require visual inspection to guarantee the presence of authentic interictal spikes rather than artefacts (Agirre-Arrizubieta et al., 2014; de Gooijer-van de Groep et al., 2013; Hall et al., 2018; Kirsch et al., 2006; Oishi et al., 2006; Rose et al., 2013; Tenney et al., 2014). In this work, visual inspection was only required for the representative discharges extracted from the virtual sensor with the maximum

kurtosis in each beamforming segment. This method can reveal interictal spikes effectively, with spikes localised in 12 out of the 13 patients studied.

This study explored spike frequencies on the VSs reconstructed using beamforming from MEG data to assess localisation performance of the maximal interictal spike frequency (MISF). The MISF was able to localise to the epileptogenic zone at the lobe level correctly, even though the patients included in this study were complex and challenging cases as their brain images, including MRI, VEM, PET and SPECT, did not provide consistent localisations (see Table 2-1). This result indicates that the MISF method may be used to constrain surgical resection to a certain brain lobe and can guide the implantation of intracranial EEG for presurgical evaluation.

Effective localisation using quantified interictal spikes on VSs reconstructed using beamforming has also been shown in another study that showed regions with the maximum percentage of spikes/sharp waves on VSs were co-localised to the seizure onset zone defined by subdural EEG in 7 out of 9 patients (Oishi et al., 2006). However, that study did not validate the localised maximum percentage of abnormal discharges against surgical resections. Another study validated the localised VSs with maximal kurtosis against the surgical resections, which were concordant with surgical cavities in 9 out of 13 seizure-free patients at the lobe level (Hall et al., 2018). Our work indicates that spike frequency may be a better biomarker than kurtosis for EZ localisation.

The concordance of MISF regions with clinical solutions can predict surgical outcomes. Therefore, this approach may help indicate clinical localisation that may contribute to seizure-free surgical outcome at the non-invasive evaluation stage. In the study of Hall et al. (2018), the concordance of localised VS with maximal kurtosis with surgical resection at the lobe level was 9 out of 13 seizure-free patients and 3 out of 5 non-seizure-free patients. However, the MISF was co-localised with surgical cavities at the same lobe in all 8 out of 8 seizure-free patients and in 1 out of 3 non-seizure-free patients. This also indicates that spike frequency may predict surgical outcome better than kurtosis.

We also compared localisation performance of MISF regions with clinical onset regions. Their performances were comparable, with clinical onset outperforming MISF marginally. It is worth noting that the clinical onset was localised using sLORETA from averaged interictal spikes, which required a neurophysiologist to annotate the interictal spikes from the continuous MEG sensor data, while the MISF method required much fewer visual inspections to identify spikes.

Englot et al. (2015) reported localisation performance validated against surgical resection of another commonly used localisation method: dipole fitting. For 71 seizure-free patients, the dipole fitting co-localised to the surgical resection at the same lobe in 82% of patients. In our work, the percentage of lobar co-localisation of MISF with surgical cavities was 100%. However, comparison is problematic because of the considerable difference between numbers of patients in the two cohorts. In addition, the patients considered in our work were those for whom EZs were considered difficult to localise.

The method proposed in this study has limitations. The method failed to detect interictal spikes on VSs in one patient (P074). The probable reason, which is a limitation of this study, is that we only included one VS with the maximal kurtosis in each beamforming segment in the subsequent analysis. The limited inclusion of VSs may contribute to failing to detect interictal spikes, and it may only reveal incomplete spatial distributions of spike frequencies. In future work, it will be important to include more VSs rather than only the first VS to uncover spikes suppressed by noise or other physiological signals. The inclusion of more VSs may not only enable the consideration of spikes with low SNR, but also enable the comprehensive analysis of the spatial distributions of interictal spikes.

Another limitation of this method is that the MISF method can only localise a single area with maximal spike frequency. Thus, it is unable to localise to multiple locations for patients with multiple independent epileptic sources, such as patient P007. One possible solution is to consider regions with spike frequencies significantly higher than others rather than only the maximal one as the localisation solution. This may help source localisation for patients with multiple foci. Therefore, inclusion of more VSs and decreasing the threshold for spike frequency may help us to understand the spatial distribution of epileptic interictal spikes and their relationship to surgical resections and outcomes for drug refractory patients with a single focus or multiple foci.

5.5 Conclusion

The proposed method in this study can simplify the visual inspection of virtual sensors after kurtosis beamforming. The maximal interictal spike frequency (MISF) on the virtual sensors reconstructed by beamforming from MEG data can localise to the epileptogenic zone at the lobar level accurately. In presurgical evaluation, considering both the MISF region and the clinical solution can predict seizure-free surgical outcome.

Chapter 6 Conclusion

Epilepsy is a neurological disorder that causes the brain to have recurrent seizures. 1% of population across the world are affected by epilepsy. Seizures in one third of patients cannot be controlled by medication adequately meaning that twenty million people are drug refractory. Effectiveness of treatments for refractory epilepsy patients are still limited. Epileptic source localisation can improve therapeutic effects for responsive neural stimulation and epilepsy surgery. In particular, epilepsy surgery is the only way currently to cure epilepsy and the surgical outcome is determined by the accuracy of source localisation in presurgical evaluation.

MEG is a non-invasive functional brain imaging technique that has superb temporal resolution. It has been shown that it can provide additional information for surgical plans (Agirre-Arrizubieta et al., 2009), while the validations of MEG source localisation against surgical resection and outcome are limited. Englot et al. (2015) and Plummer et al. (2019) performed dipole fitting and sLORETA on averaged interictal spike and validated localised areas against surgical resections. In the study of Englot et al. (2015), the dipole fitting method localised to surgically resected brain lobes in 82% of 71 seizure-free patients with spikes modelled. The limited patient cohort was included in the study of Plummer et al. (2019) that the onset of spikes was localised to the surgical resection in terms of overlapping in 8 out of 9 seizure-free patients. The annotations of spikes along MEG recordings were involved in both studies, which can be time consuming and limit the application of in epileptic source localisation.

Kurtosis beamforming can be applied to continuous MEG data without requiring neurophysiologists to annotate spikes. The validation of kurtosis beamforming against surgical resections are also limited. Only one work has assessed localisation performance of kurtosis beamforming against surgical resections and outcomes in a limited size of patient cohort with 22 refractory epilepsy patients (Hall et al., 2018). In addition, two major issues exist in detecting interictal spikes on VSs using kurtosis:

1. Kurtosis is biased to infrequent interictal spikes and
2. Kurtosis not only detects interictal spikes, but also detects artefacts and other brain activities that stand out from background.

Because of limited application and evaluation of MEG in presurgical source localisation, we covered the following three objectives in this thesis by retrospectively studying MEG recordings of 13 focal epilepsy patients:

1. Localise epileptogenic zones using kurtosis beamforming and explore the performance with different sliding windows;
2. Develop an automatic interictal spike detection method on VSs and validate its performance against labels from human experts.
3. Investigate the spatial distributions of interictal spikes on virtual sensors (VSs) and associate spike frequency with the epileptogenic zones;

The major conclusions we achieved from three the studies of this thesis were:

- The performance of kurtosis beamforming can be improved by using a sliding window.
- The maximal interictal spike frequency on virtual sources reconstructed using beamforming from MEG data can localise to the epileptogenic zone accurately at the lobar level.
- The performance of the automatic detection method developed in this project is comparable to labelling by human experts.

In the study of the first objective (Chapter 3), we applied kurtosis beamforming and performed source localisation using four approaches. Two approaches were implemented using 3 min and 1 s sliding windows, while the other two approaches were the VS with maximal kurtosis (used by Hall et al., 2018) and regions with persistent interictal spikes. In our patient cohort, the best method was the 1 s sliding window, while 3 min sliding window and regions with persist interictal spikes had similar performance validated against surgical resections. In the following work, it is worth exploring optimal and patient-specific sliding windows to further improve the localisation performance of kurtosis beamforming.

The second study of this thesis (Chapter 4) was an automatic spike detection method on VSs, which showed comparable performance with human experts. The automatic spike detection method on VSs enables research on quantification of interictal spikes using the non-invasive modality, MEG. Future studies should investigate detection of spikes on MEG VSs and their spatiotemporal dynamics, which has shown associations with epileptic source localisation in intracranial EEG studies (Conrad et al., 2019; Tomlinson et al., 2019b).

In the third study (Chapter 5), we detected interictal spikes on VSs directly instead of using kurtosis, which detects all the outliers in time series. The maximal interictal spike frequency can localise to surgically resected lobe in all eight seizure-free patients with spikes localised. Additionally, it localised outside of the resected lobe in three out of four seizure-persistent

patients. This indicates the maximal interictal spike frequency can localise to EZ with good sensitivity as well as specificity. This is one of the major contributions of this thesis, in which the association between spike frequencies and epileptic source localisation have been investigated in intracranial EEG studies, but where there is still debate about their performance and stability (Bartolomei et al., 2016; Conrad et al., 2019; Goncharova et al., 2009; Hufnagel et al., 2000; Libenson et al., 2014). Our study demonstrates that spike rate recorded by MEG is correlated with EZ localisation. It is worth noting that patients included in this study were difficult cases, since the patient selection criteria included non-lesion or complex lesion MRI and inconsistent localised results using other non-invasive modalities.

Two validations – surgical resections and the clinical source localisation using sLORETA – were used in this study as references for epileptogenic zone (EZ) source localisation results. EZ is defined as the minimum amount of cortex that has to be resected to achieve seizure freedom; however, this is just a theoretical concept. The resected area of epilepsy surgery with seizure-free outcome is the best proximal region of the EZ. Nonetheless, they are not equivalent because seizure-free surgical outcome only indicates that the EZ has been included in the resected area (Rosenow & Lüders, 2001). Another validation used was clinical source localisation of MEG interictal spikes using sLORETA, which has been performed by experienced experts with thorough and skilled procedures. However, it reveals the irritative zone that generates interictal spikes, which has been reported can be more extensive than the EZ (Bartolomei et al., 2016; Lüders et al., 2006; Plummer et al., 2019; Rosenow & Lüders, 2001).

One approach to alleviate the limitations of validating using surgical resections and clinical source localisation would be to use a phantom brain in future studies from which we can allocate brain sources and validate source localisation methods with the ground truth (Lau et al., 2014). Additionally, it is worth applying methods developed in the thesis in an extended patient cohort and repeated MEG data recordings from multiple sessions to verify their practical value and the reproducibility for the following clinical application.

The increasing interest in research that interprets epilepsy activities as network interactions sheds light on source localisation in pre-surgical evaluations with a set of novel tools including methods from graph theory and virtual resection of nodes in a network built from ictal data or from data-driven models (Goodfellow et al., 2016; Kini et al., 2019; Nissen et al., 2017).

Dynamic connectivity networks may also be very useful tools for localisation of fast evolving electrical discharges of the brain.

Bibliography

Adams, R., & Bischof, L. (1994). Seeded region growing. *IEEE Transactions on pattern analysis machine intelligence, 16*(6), 641-647.

Adjouadi, M., Cabrerizo, M., Ayala, M., Sanchez, D., Yaylali, I., Jayakar, P., & Barreto, A. (2004). A new mathematical approach based on orthogonal operators for the detection of interictal spikes in epileptogenic data. *Biomedical sciences instrumentation, 40*, 175-180.

Adjouadi, M., Sanchez, D., Cabrerizo, M., Ayala, M., Jayakar, P., Yaylali, I., & Barreto, A. (2004). Interictal spike detection using the Walsh transform. *J IEEE Transactions on Biomedical Engineering, 51*(5), 868-872.

Agirre-Arrizubieta, Z., Huiskamp, G., Ferrier, C., Van Huffelen, A., & Leijten, F. (2009). Interictal magnetoencephalography and the irritative zone in the electrocorticogram. *Brain, 132*(11), 3060-3071.

Agirre-Arrizubieta, Z., Thai, N. J., Valentín, A., Furlong, P. L., Seri, S., Selway, R. P., Elwes, R. D., & Alarcón, G. (2014). The value of Magnetoencephalography to guide electrode implantation in epilepsy. *Brain topography, 27*(1), 197-207.

Babb, T. L., Wilson, C. L., & Isokawa-Akesson, M. (1987). Firing patterns of human limbic neurons during stereoencephalography (SEEG) and clinical temporal lobe seizures. *Electroencephalography clinical neurophysiology, 66*(6), 467-482.

Baillet, S., Mosher, J. C., & Leahy, R. M. (2001). Electromagnetic brain mapping. *IEEE Signal processing magazine, 18*(6), 14-30.

Barth, D. S., Sutherling, W., Broffman, J., & Beatty, J. (1986). Magnetic localization of a dipolar current source implanted in a sphere and a human cranium. *Electroencephalography clinical neurophysiology, 63*(3), 260-273.

Bartolomei, F., Trébuchon, A., Bonini, F., Lambert, I., Gavaret, M., Woodman, M., Giusiano, B., Wendling, F., & Bénar, C. (2016). What is the concordance between the seizure onset zone and the irritative zone? A SEEG quantified study. *Clinical Neurophysiology, 127*(2), 1157-1162.

Baumgartner, C., Alexopoulos, N., Taylor, S., Rogers, R. L. J. E., & neurophysiology, c. (1995). MEG and ECoG localization accuracy test. *94*, 109-114.

Bazhenov, M., Lonjers, P., Skorheim, S., Bedard, C., Destexhe, A. J. P. T. o. t. R. S. A. M., Physical, & Sciences, E. (2011). Non-homogeneous extracellular resistivity affects the current-source density profiles of up–down state oscillations. *369*(1952), 3802-3819.

Bell, A. J., & Sejnowski, T. J. (1995). An information-maximization approach to blind separation and blind deconvolution. *Neural computation, 7*(6), 1129-1159.

Bergey, G. K., Morrell, M. J., Mizrahi, E. M., Goldman, A., King-Stephens, D., Nair, D., Srinivasan, S., Jobst, B., Gross, R. E., & Shields, D. C. (2015). Long-term treatment with responsive brain stimulation in adults with refractory partial seizures. *Neurology, 84*(8), 810-817.

Birot, G., Spinelli, L., Vulliémoz, S., Mégevand, P., Brunet, D., Seeck, M., & Michel, C. M. (2014). Head model and electrical source imaging: a study of 38 epileptic patients. *NeuroImage: Clinical, 5*, 77-83.

Black, M. A., Jones, R. D., Carroll, G. J., Dingle, A. A., Donaldson, I. M., & Parkin, P. J. (2000). Real-time detection of epileptiform activity in the EEG: a blinded clinical trial. *Clinical Electroencephalography, 31*(3), 122-130.

Bonilha, L., Nesland, T., Martz, G. U., Joseph, J. E., Spampinato, M. V., Edwards, J. C., & Tabesh, A. (2012). Medial temporal lobe epilepsy is associated with neuronal fibre loss and paradoxical increase in structural connectivity of limbic structures. *J Neurol Neurosurg Psychiatry, 83*(9), 903-909.

Bradley, A. P. (1997). The use of the area under the ROC curve in the evaluation of machine learning algorithms. *Pattern recognition, 30*(7), 1145-1159.

Breiman, L. (1996). Bagging predictors. *Machine learning, 24*(2), 123-140.

Breiman, L. (2001). Random forests. *Machine learning, 45*(1), 5-32.

Brookes, M. J., Vrba, J., Robinson, S. E., Stevenson, C. M., Peters, A. M., Barnes, G. R., Hillebrand, A., & Morris, P. G. (2008). Optimising experimental design for MEG beamformer imaging. *Neuroimage, 39*(4), 1788-1802.

Caliński, T., & Harabasz, J. (1974). A dendrite method for cluster analysis. *Communications in Statistics-theory Methods, 3*(1), 1-27.

Cendes, F., Theodore, W. H., Brinkmann, B. H., Sulc, V., & Cascino, G. D. (2016). Neuroimaging of epilepsy. In *Handbook of clinical neurology* (Vol. 136, pp. 985-1014): Elsevier.

Chawla, N. V., Bowyer, K. W., Hall, L. O., & Kegelmeyer, W. P. (2002). SMOTE: synthetic minority over-sampling technique. *Journal of artificial intelligence research, 16*, 321-357.

Clopper, C. J., & Pearson, E. S. (1934). The use of confidence or fiducial limits illustrated in the case of the binomial. *Biometrika, 26*(4), 404-413.

Cohen, D., Cuffin, B. N., Yunokuchi, K., Maniewski, R., Purcell, C., Cosgrove, G. R., Ives, J., Kennedy, J. G., & Schomer, D. L. (1990). MEG versus EEG localization test using implanted sources in the human brain. *Annals of Neurology: Official Journal of the American Neurological Association the Child Neurology Society, 28*(6), 811-817.

Conrad, E. C., Tomlinson, S. B., Wong, J. N., Oechsel, K. F., Shinohara, R. T., Litt, B., Davis, K. A., & Marsh, E. D. (2019). Spatial distribution of interictal spikes fluctuates over time and localizes seizure onset. *Brain*.

de Gooijer-van de Groep, K. L., Leijten, F. S., Ferrier, C. H., & Huiskamp, G. J. (2013). Inverse modeling in magnetic source imaging: comparison of MUSIC, SAM (g2), and sLORETA to interictal intracranial EEG. *Human brain mapping, 34*(9), 2032-2044.

Delorme, A., & Makeig, S. (2004). EEGLAB: an open source toolbox for analysis of single-trial EEG dynamics including independent component analysis. *Journal of Neuroscience Methods, 134*(1), 9-21.

Dingle, A. A., Jones, R. D., Carroll, G. J., & Fright, W. R. (1993). A multistage system to detect epileptiform activity in the EEG. *IEEE Transactions on Biomedical Engineering, 40*(12), 1260-1268.

Duncan, J. S. (1997). Imaging and epilepsy. *Brain: a journal of neurology, 120*(2), 339-377.

Ebersole, J. S., & Ebersole, S. M. (2010). Combining MEG and EEG source modeling in epilepsy evaluations. *Journal of Clinical Neurophysiology, 27*(6), 360-371.

Engel, J. J. (2000). Overview of functional neuroimaging in epilepsy. *Advances in neurology, 83*, 1-9.

Engel Jr, J. (1992). Update on surgical treatment of the epilepsies. *Clinical experimental neurology, 29*, 32.

Engel Jr, J. (1993). *Outcome with respect to epileptic seizures*.

Englot, D. J., Chang, E. F., & Auguste, K. I. (2011). Vagus nerve stimulation for epilepsy: a meta-analysis of efficacy and predictors of response: a review. *Journal of neurosurgery, 115*(6), 1248-1255.

Englot, D. J., Nagarajan, S. S., Imber, B. S., Raygor, K. P., Honma, S. M., Mizuiri, D., Mantle, M., Knowlton, R. C., Kirsch, H. E., & Chang, E. F. (2015). Epileptogenic zone localization using magnetoencephalography predicts seizure freedom in epilepsy surgery. *Epilepsia, 56*(6), 949-958.

Exarchos, T. P., Tzallas, A. T., Fotiadis, D. I., Konitsiotis, S., & Giannopoulos, S. (2006). EEG transient event detection and classification using association rules. *IEEE Transactions on Information Technology in Biomedicine, 10*(3), 451-457.

Fernandes, J. M., da Silva, A. M., Huiskamp, G., Velis, D. N., Manshanden, I., de Munck, J. C., da Silva, F. L., & Cunha, J. P. S. (2005). What does an epileptiform spike look like in MEG? Comparison between coincident EEG and MEG spikes. *Journal of Clinical Neurophysiology, 22*(1), 68-73.

Feucht, M., Hoffmann, K., Steinberger, K., Witte, H., Benninger, F., Arnold, M., & Doering, A. (1997). Simultaneous spike detection and topographic classification in pediatric surface EEGs. *NeuroReport, 8*(9), 2193-2197.

Fisher, R. S., Boas, W. V. E., Blume, W., Elger, C., Genton, P., Lee, P., & Engel Jr, J. (2005). Epileptic seizures and epilepsy: definitions proposed by the International League Against Epilepsy (ILAE) and the International Bureau for Epilepsy (IBE). *Epilepsia, 46*(4), 470-472.

Goncharova, I. I., Zaveri, H. P., Duckrow, R. B., Novotny, E. J., & Spencer, S. S. (2009). Spatial distribution of intracranially recorded spikes in medial and lateral temporal epilepsies. *Epilepsia, 50*(12), 2575-2585.

Goodfellow, M., Rummel, C., Abela, E., Richardson, M., Schindler, K., & Terry, J. (2016). Estimation of brain network ictogenicity predicts outcome from epilepsy surgery. *Scientific reports, 6*, 29215.

Gotman, J., & Gloor, P. (1976). Automatic recognition and quantification of interictal epileptic activity in the human scalp EEG. *Electroencephalography clinical neurophysiology, 41*(5), 513-529.

Gotman, J., Ives, J., & Gloor, P. (1979). Automatic recognition of inter-ictal epileptic activity in prolonged EEG recordings. *Electroencephalography clinical neurophysiology, 46*(5), 510-520.

Gray, H., & Lewis, W. (1918). Anatomy of the Human Body. Lea & Febiger, Philadelphia.

Halford, J. J. (2009). Computerized epileptiform transient detection in the scalp electroencephalogram: Obstacles to progress and the example of computerized ECG interpretation. *Clinical Neurophysiology, 120*(11), 1909-1915.

Hall, J. E. (2015). *Guyton & Hall Physiology Review E-Book*: Elsevier Health Sciences.

Hall, M. B., Nissen, I. A., Van Straaten, E. C., Furlong, P. L., Witton, C., Foley, E., Seri, S., & Hillebrand, A. (2018). An evaluation of kurtosis beamforming in magnetoencephalography to localize the epileptogenic zone in drug resistant epilepsy patients. *Clinical Neurophysiology, 129*(6), 1221-1229.

Hanley, J. A., & McNeil, B. J. (1982). The meaning and use of the area under a receiver operating characteristic (ROC) curve. *Radiology, 143*(1), 29-36.

Harpaz, Y., Robinson, S. E., Medvedovsky, M., & Goldstein, A. (2015). Improving the excess kurtosis (g2) method for localizing epileptic sources in magnetoencephalographic recordings. *Clinical Neurophysiology, 126*(5), 889-897.

Haueisen, J., & Knösche, T. R. (2019). Forward modeling and tissue conductivities. *Magnetoencephalography: From signals to dynamic cortical networks*, 145-165.

Heeger, P. D. Poisson model of spike generation.

Heller, L., & Volegov, P. (2014). Electric and magnetic fields of the brain. In *Magnetoencephalography* (pp. 73-105): Springer.

Hillebrand, A., & Barnes, G. R. (2005). Beamformer analysis of MEG data. *International review of neurobiology, 68*, 149-171.

Hillebrand, A., Nissen, I. A., Ris-Hilgersom, I., Sijsma, N., Ronner, H., Van Dijk, B., & Stam, C. (2016). Detecting epileptiform activity from deeper brain regions in spatially filtered MEG data. *Clin. Neurophysiol, 127*(8), 2766-2769.

Huang, M. X., Shih, J., Lee, R., Harrington, D., Thoma, R., Weisend, M., Hanlon, F., Paulson, K., Li, T., & Martin, K. (2004). Commonalities and differences among vectorized beamformers in electromagnetic source imaging. *Brain topography, 16*(3), 139-158.

Huettel, S. A., Song, A. W., & McCarthy, G. (2004). *Functional magnetic resonance imaging* (Vol. 1): Sinauer Associates Sunderland, MA.

Hufnagel, A., Dümpelmann, M., Zentner, J., Schijns, O., & Elger, C. (2000). Clinical relevance of quantified intracranial interictal spike activity in presurgical evaluation of epilepsy. *Epilepsia, 41*(4), 467-478.

Idrees, F., Rajarajan, M., Conti, M., Chen, T. M., & Rahulamathavan, Y. (2017). PIndroid: A novel Android malware detection system using ensemble learning methods. *Computers Security, 68*, 36-46.

İnan, Z. H., & Kuntalp, M. (2007a). A study on fuzzy C-means clustering-based systems in automatic spike detection. *%J Computers in biology medicine, 37*(8), 1160-1166.

İnan, Z. H., & Kuntalp, M. (2007b). A study on fuzzy C-means clustering-based systems in automatic spike detection. *Computers in biology medicine, 37*(8), 1160-1166.

Ishii, R., Canuet, L., Ochi, A., Xiang, J., Imai, K., Chan, D., Iwase, M., Takeda, M., Snead III, O. C., & Otsubo, H. (2008). Spatially filtered magnetoencephalography compared with electrocorticography to identify intrinsically epileptogenic focal cortical dysplasia. *Epilepsy research, 81*(2-3), 228-232.

Isokawa-Akesson, M., Wilson, C. L., & Babb, T. L. (1989). Inhibition in synchronously firing human hippocampal neurons. *Epilepsy research, 3*(3), 236-247.

Iwasaki, M., Pestana, E., Burgess, R. C., Lüders, H. O., Shamoto, H., & Nakasato, N. (2005). Detection of epileptiform activity by human interpreters: blinded comparison between electroencephalography and magnetoencephalography. *Epilepsia, 46*(1), 59-68.

Ketchen, D. J., & Shook, C. L. (1996). The application of cluster analysis in strategic management research: an analysis and critique. *Strategic management journal, 17*(6), 441-458.

Khalid, M. I., Alotaiby, T., Aldosari, S. A., Alshebeili, S. A., Al-Hameed, M. H., Almohammed, F. S. Y., & Alotaibi, T. S. (2016). Epileptic MEG spikes detection using common spatial patterns and linear discriminant analysis. *IEEE Access, 4*, 4629-4634.

Khalid, M. I., Alotaiby, T. N., Aldosari, S. A., Alshebeili, S. A., Alhameed, M. H., & Poghosyan, V. (2017). Epileptic MEG spikes detection using amplitude thresholding and dynamic time warping. *IEEE Access, 5*, 11658-11667.

Kini, L. G., Bernabei, J. M., Mikhail, F., Hadar, P., Shah, P., Khambhati, A. N., Oechsel, K., Archer, R., Boccanfuso, J., & Conrad, E. (2019). Virtual resection predicts surgical outcome for drug-resistant epilepsy. *Brain, 142*(12), 3892-3905.

Kirsch, H., Robinson, S., Mantle, M., & Nagarajan, S. (2006). Automated localization of magnetoencephalographic interictal spikes by adaptive spatial filtering. *Clinical Neurophysiology, 117*(10), 2264-2271.

Kooi, K. A. (1966). Voltage-time characteristics of spikes and other rapid electroencephalographic transients: semantic and morphological considerations. *Neurology, 16*(1), 59-59.

Lau, S., Flemming, L., & Haueisen, J. (2014). Magnetoencephalography signals are influenced by skull defects. *Clinical Neurophysiology, 125*(8), 1653-1662.

Lawson, R. (2004). Small sample confidence intervals for the odds ratio. *Communications in Statistics-Simulation Computation, 33*(4), 1095-1113.

Leahy, R., Mosher, J., Spencer, M., Huang, M., & Lewine, J. (1998). A study of dipole localization accuracy for MEG and EEG using a human skull phantom. *Electroencephalography clinical neurophysiology, 107*(2), 159-173.

Lee, Y.-H., & Kim, K. (2019). Instrumentation for Measuring MEG Signals. *Magnetoencephalography: From signals to dynamic cortical networks*, 41-71.

Libenson, M. H., Haldar, A., & Pinto, A. L. (2014). The stability of spike counts in children with interictal epileptiform activity. *Seizure, 23*(6), 454-456.

Liu, H. S., Zhang, T., & Yang, F. S. (2002). A multistage, multimethod approach for automatic detection and classification of epileptiform EEG. *IEEE Transactions on biomedical engineering, 49*(12), 1557-1566.

Lüders, H. O., Najm, I., Nair, D., Widdess-Walsh, P., & Bingman, W. (2006). The epileptogenic zone: general principles. *Epileptic disorders, 8*(2), 1-9.

Maharaj, E. A. (2000). Cluster of Time Series. *Journal of Classification, 17*(2).

Mandrekar, J. N. (2010). Receiver operating characteristic curve in diagnostic test assessment. *Journal of Thoracic Oncology, 5*(9), 1315-1316.

Mégevand, P., & Seeck, M. (2018). Electroencephalography, magnetoencephalography and source localization: their value in epilepsy. *Current opinion in neurology, 31*(2), 176-183.

Mercaldo, N. D., Lau, K. F., & Zhou, X. H. (2007). Confidence intervals for predictive values with an emphasis to case–control studies. *Statistics in medicine, 26*(10), 2170-2183.

Meyer-Lindenberg, A. (2010). From maps to mechanisms through neuroimaging of schizophrenia. *Nature, 468*(7321), 194-202.

Mikuni, N., Nagamine, T., Ikeda, A., Terada, K., Taki, W., Kimura, J., Kikuchi, H., & Shibasaki, H. J. N. (1997). Simultaneous recording of epileptiform discharges by MEG and subdural electrodes in temporal lobe epilepsy. *5*(4), 298-306.

Morris, J. A., & Gardner, M. J. (1988). Calculating confidence intervals for relative risks (odds ratios) and standardised ratios and rates. *British Medical Journal, 296*(6632), 1313-1316.

Nguyen, D. K., Mbacfou, M. T., Nguyen, D. B., & Lassonde, M. (2013). Prevalence of nonlesional focal epilepsy in an adult epilepsy clinic. *Canadian journal of neurological sciences, 40*(2), 198-202.

Nissen, I. A., Stam, C. J., Reijneveld, J. C., van Straaten, I. E., Hendriks, E. J., Baayen, J. C., De Witt Hamer, P. C., Idema, S., & Hillebrand, A. (2017). Identifying the epileptogenic zone in interictal resting-state MEG source-space networks. *Epilepsia, 58*(1), 137-148.

Nolte, G. (2003). The magnetic lead field theorem in the quasi-static approximation and its use for magnetoencephalography forward calculation in realistic volume conductors. *Physics in Medicine Biology, 48*(22), 3637.

Nowak, R., Santiuste, M., & Russi, A. (2009). Toward a definition of MEG spike: parametric description of spikes recorded simultaneously by MEG and depth electrodes. *Seizure, 18*(9), 652-655.

Nunez, P. L., & Srinivasan, R. (2006). *Electric fields of the brain: the neurophysics of EEG*: Oxford University Press, USA.

Oishi, M., Otsubo, H., Iida, K., Suyama, Y., Ochi, A., Weiss, S. K., Xiang, J., Gaetz, W., Cheyne, D., & Chuang, S. H. (2006). Preoperative simulation of intracerebral epileptiform discharges: synthetic aperture magnetometry virtual sensor analysis of interictal magnetoencephalography data. *Journal of Neurosurgery: Pediatrics, 105*(1), 41-49.

Oishi, M., Otsubo, H., Kameyama, S., Morota, N., Masuda, H., Kitayama, M., & Tanaka, R. (2002). Epileptic spikes: magnetoencephalography versus simultaneous electrocorticography. *Epilepsia, 43*(11), 1390-1395.

Oostenveld, R., Fries, P., Maris, E., & Schoffelen, J.-M. (2011). FieldTrip: open source software for advanced analysis of MEG, EEG, and invasive electrophysiological data. *Computational intelligence and neuroscience, 2011*, 1.

Pascual-Marqui, & Domingo, R. (1999). Review of methods for solving the EEG inverse problem. *International journal of bioelectromagnetism, 1*(1), 75-86.

Pascual-Marqui, R. D., Michel, C. M., & Lehmann, D. (1994). Low resolution electromagnetic tomography: a new method for localizing electrical activity in the brain. *International Journal of psychophysiology, 18*(1), 49-65.

Phelps, M. E., Hoffman, E. J., Mullani, N. A., & Ter-Pogossian, M. M. (1975). Application of annihilation coincidence detection to transaxial reconstruction tomography. *Journal of Nuclear Medicine, 16*(3), 210-224.

Pizzella, V., & Romani, G. (1990). Principles of magnetoencephalography. *Advances in neurology, 54*, 1-9.

Plummer, C., Vogrin, S. J., Woods, W. P., Murphy, M. A., Cook, M. J., & Liley, D. T. (2019). Interictal and ictal source localization for epilepsy surgery using high-density EEG with MEG: a prospective long-term study. *Brain, 142*(4), 932-951.

Ramanujam, B., Bharti, K., Viswanathan, V., Garg, A., Tripathi, M., Bal, C., Chandra, P. S., & Tripathi, M. (2017). Can ictal-MEG obviate the need for phase II monitoring in people with drug-refractory epilepsy? A prospective observational study. *Seizure, 45*, 17-23.

Ramírez, R. R. (2008). Source localization. *Scholarpedia, 3*(11), 1733.

Richard, C., Tanenbaum, A., Audit, B., Arneodo, A., Khalil, A., & Frankel, W. N. (2015). Swdreader: a wavelet-based algorithm using spectral phase to characterize spike-wave morphological variation in genetic models of absence epilepsy. *Journal of Neuroscience Methods, 242*, 127-140.

Robinson, S., Nagarajan, S., Mantle, M., Gibbons, V., & Kirsch, H. (2004). Localization of interictal spikes using SAM (g2) and dipole fit. *Neurology & clinical neurophysiology: NCN, 2004*, 74.

Rose, D., Fujiwara, H., Holland-Bouley, K., Greiner, H., Arthur, T., & Mangano, F. T. (2013). Focal peak activities in spread of interictal-ictal discharges in epilepsy with beamformer MEG: evidence for an epileptic network? *Frontiers in neurology, 4*, 56.

Rosenow, F., & Lüders, H. (2001). Presurgical evaluation of epilepsy. *Brain, 124*(9), 1683-1700.

Sander, J., & Shorvon. (1996). Epidemiology of the epilepsies. *Journal of neurology, neurosurgery, and psychiatry, 61*(5), 433.

Sankar, R., & Natour, J. (1992). Automatic computer analysis of transients in EEG. *Computers in biology medicine, 22*(6), 407-422.

Sarvas, J. (1987). Basic mathematical and electromagnetic concepts of the biomagnetic inverse problem. *Physics in Medicine Biology, 32*(1), 11.

Schachter, S. C., & Saper, C. B. (1998). Vagus nerve stimulation. *Epilepsia, 39*(7), 677-686.

Scheuer, M. L., Bagic, A., & Wilson, S. B. (2017). Spike detection: Inter-reader agreement and a statistical Turing test on a large data set. *Clinical Neurophysiology, 128*(1), 243-250.

Schuele, S. U., & Lüders, H. O. (2008). Intractable epilepsy: management and therapeutic alternatives. *The Lancet Neurology, 7*(6), 514-524.

Scott, J. M., Robinson, S. E., Holroyd, T., Coppola, R., Sato, S., & Inati, S. K. (2016). Localization of interictal epileptic spikes with MEG: optimization of an automated beamformer screening method (SAMepi) in a diverse epilepsy population. *Journal of clinical neurophysiology: official publication of the American Electroencephalographic Society, 33*(5), 414.

Sekihara, K., & Nagarajan, S. S. (2008). *Adaptive spatial filters for electromagnetic brain imaging*: Springer Science & Business Media.

Sekihara, K., Nagarajan, S. S., Poeppel, D., Marantz, A., & Miyashita, Y. (2001). Reconstructing spatio-temporal activities of neural sources using an MEG vector beamformer technique. *IEEE Transactions on Biomedical Engineering, 48*(7), 760-771.

Sekihara, K., Nagarajan, S. S., Poeppel, D., Marantz, A., & Miyashita, Y. (2002). Application of an MEG eigenspace beamformer to reconstructing spatio-temporal activities of neural sources. *Human brain mapping, 15*(4), 199-215.

Senhadji, L., Dillenseger, J.-L., Wendling, F., Rocha, C., & Kinie, A. (1995). Wavelet analysis of EEG for three-dimensional mapping of epileptic events. *Annals of biomedical engineering, 23*(5), 543-552.

Spencer, S., & Huh, L. (2008). Outcomes of epilepsy surgery in adults and children. *The Lancet Neurology, 7*(6), 525-537.

Stafstrom, C. E., & Carmant, L. (2015). Seizures and epilepsy: an overview for neuroscientists. *Cold Spring Harbor perspectives in medicine, 5*(6), a022426.

Stapleton-Kotloski, J. R., Kotloski, R. J., Boggs, J. A., Popli, G., O'Donovan, C. A., Couture, D. E., Cornell, C., & Godwin, D. W. (2014). Localization of interictal epileptiform activity using magnetoencephalography with synthetic aperture magnetometry in patients with a vagus nerve stimulator. *Frontiers in neurology, 5*, 244.

Stevens, J. R., Lonsbury, B. L., & Goel, S. L. (1972). Seizure occurrence and interspike interval: telemetered electroencephalogram studies. *Archives of neurology, 26*(5), 409-419.

Sugiyama, I., Imai, K., Yamaguchi, Y., Ochi, A., Akizuki, Y., Go, C., Akiyama, T., Snead, O. C., Rutka, J. T., & Drake, J. M. (2009). Localization of epileptic foci in children with intractable epilepsy secondary to multiple cortical tubers by using synthetic aperture magnetometry kurtosis. *Journal of Neurosurgery: Pediatrics, 4*(6), 515-522.

Sun, F. T., Morrell, M. J., & Wharen, R. E. (2008). Responsive cortical stimulation for the treatment of epilepsy. *Neurotherapeutics, 5*(1), 68-74.

Tao, J. X., Ray, A., Hawes-Ebersole, S., & Ebersole, J. S. (2005). Intracranial EEG substrates of scalp EEG interictal spikes. *Epilepsia, 46*(5), 669-676.

Taulu, S., Simola, J., Nenonen, J., & Parkkonen, L. (2019). Novel noise reduction methods. *Magnetoencephalography: From signals to dynamic cortical networks*, 73-109.

Tenney, J. R., Fujiwara, H., Horn, P. S., & Rose, D. F. (2014). Comparison of magnetic source estimation to intracranial EEG, resection area, and seizure outcome. *Epilepsia, 55*(11), 1854-1863.

Tomlinson, S. B., Bermudez, C., Conley, C., Brown, M. W., Porter, B. E., & Marsh, E. D. (2016). Spatiotemporal mapping of interictal spike propagation: a novel methodology applied to pediatric intracranial EEG recordings. *Frontiers in neurology, 7*, 229.

Tomlinson, S. B., Porter, B. E., & Marsh, E. D. (2017). Interictal network synchrony and local heterogeneity predict epilepsy surgery outcome among pediatric patients. *Epilepsia, 58*(3), 402-411.

Tomlinson, S. B., Wong, J. N., Conrad, E. C., Kennedy, B. C., & Marsh, E. D. (2019a). Reproducibility of interictal spike propagation in children with refractory epilepsy. *Epilepsia*, *60*(5), 898-910.

Tomlinson, S. B., Wong, J. N., Conrad, E. C., Kennedy, B. C., & Marsh, E. D. J. E. (2019b). Reproducibility of interictal spike propagation in children with refractory epilepsy. *60*(5), 898-910.

Tzallas, A., Karvelis, P., Katsis, C., Fotiadis, D., Giannopoulos, S., & Konitsiotis, S. (2006). A method for classification of transient events in EEG recordings: application to epilepsy diagnosis. *Methods of Information in Medicine, 45*(06), 610-621.

Urrestarazu, E., Jirsch, J. D., LeVan, P., & Hall, J. (2006). High-frequency intracerebral EEG activity (100–500 Hz) following interictal spikes. *Epilepsia, 47*(9), 1465-1476.

Van Veen, B. D., Van Drongelen, W., Yuchtman, M., & Suzuki, A. (1997). Localization of brain electrical activity via linearly constrained minimum variance spatial filtering. *IEEE Transactions on Biomedical Engineering, 44*(9), 867-880.

Vrba, J., & Robinson, S. E. (2001). Signal processing in magnetoencephalography. *Methods, 25*(2), 249-271.

Webber, W., Litt, B., Wilson, K., & Lesser, R. P. (1994). Practical detection of epileptiform discharges (EDs) in the EEG using an artificial neural network: a comparison of raw and parameterized EEG data. *%J Electroencephalography clinical Neurophysiology, 91*(3), 194-204.

Webber, W. R. S., Litt, B., Lesser, R. P., Fisher, R., & Bankman, I. (1993). Automatic EEG spike detection: what should the computer imitate? *Electroencephalography clinical neurophysiology, 87*(6), 364-373.

Wei, T., Simko, V., Levy, M., Xie, Y., Jin, Y., & Zemla, J. (2017). Package 'corrplot'. *Statistician, 56*, 316-324.

Wennberg, R., Valiante, T., & Cheyne, D. (2011). EEG and MEG in mesial temporal lobe epilepsy: where do the spikes really come from? *Clinical Neurophysiology, 122*(7), 1295-1313.

Westfall, P. H. (2014). Kurtosis as peakedness, 1905–2014. RIP. *The American Statistician, 68*(3), 191-195.

Wilson, S., Harner, R., Duffy, F., Tharp, B., Nuwer, M., & Sperling, M. (1996). Spike detection. I. Correlation and reliability of human experts. *Electroencephalography clinical neurophysiology, 98*(3), 186-198.

Wilson, S. B., & Emerson, R. (2002). Spike detection: a review and comparison of algorithms. *Clinical Neurophysiology, 113*(12), 1873-1881.

Wolters, C. H. (2003). *Influence of tissue conductivity inhomogeneity and anisotropy on EEG/MEG based source localization in the human brain.* Max Planck Institute of Cognitive Neuroscience Leipzig,

Wyler, A. R., Ojemann, G. A., & Ward Jr, A. A. (1982). Neurons in human epileptic cortex: correlation between unit and EEG activity. *Annals of Neurology: Official Journal of the American Neurological Association the Child Neurology Society, 11*(3), 301-308.

Youngerman, B. E., Khan, F. A., & McKhann, G. M. (2019). Stereoelectroencephalography in epilepsy, cognitive neurophysiology, and psychiatric disease: safety, efficacy, and place in therapy. *Neuropsychiatric disease treatment, 15*, 1701.

Yuan, Y., Yang, C., & Si, J. (2012). The M-Sorter: an automatic and robust spike detection and classification system. *Journal of Neuroscience Methods, 210*(2), 281-290.

Zaitoun, N. M., & Aqel, M. J. (2015). Survey on image segmentation techniques. *Procedia Computer Science, 65*, 797-806.

Zijlmans, M., Huiskamp, G. M., Leijten, F. S., van der Meij, W. M., Wieneke, G., & van Huffelen, A. C. (2002). Modality-specific spike identification in simultaneous magnetoencephalography/electroencephalography: a methodological approach. *Journal of Clinical Neurophysiology, 19*(3), 183-191.